ABSTRACT

KEPHART, JEREMY D. Method of Evaluating the effect of HPGe Design on the Sensitivity of Physics Experiments. (Under the direction of Dr. Albert Young).

Motivated by planned double beta decay experiments in ^{76}Ge I describe a computational model for the electric fields of solid state diode detectors and the subsequent charge transport. Aspects of detector performance determined by the impurity charge concentration are explored in a series of measurements of comparable "point contact" p-type germanium detectors and compared to our computational model.

In particular, we measure the capacitance of the germanium detector as a function of the bias voltage to determine the free parameters in a three parameter model of the impurity charge density, effectively mapping out the density at all points within the detector volume. We then use our impurity charge density map to refine the sensitivity of pulse shape analysis applied to various classes of physics events detected in the crystal. When possible, the impact of our refinements on a figure-of-merit for double-beta decay experiments is described.

Method of Evaluating the effect of HPGe Design on the Sensitivity of Physics Experiments

by
Jeremy Dale Kephart

A dissertation submitted to the Graduate Faculty of
North Carolina State University
in partial fullfillment of the
requirements for the Degree of
Doctor of Philosophy

Physics

Raleigh, North Carolina

2009

APPROVED BY:

Dr. Paul Huffman	Dr. Robert White
Dr. Albert Young Chair of Advisory Committee	Dr. Christopher Gould

TABLE OF CONTENTS

LIST OF TABLES viii

LIST OF FIGURES ix

1 Motivation 1
- 1.1 Overview 1
- 1.2 Introduction 3
  - 1.2.1 Neutrinos 3
- 1.3 Motivation 4
  - 1.3.1 IGEX 4
  - 1.3.2 Heidelberg-Moscow 5
  - 1.3.3 GERDA 5
  - 1.3.4 Majorana 6
  - 1.3.5 Necessary advances addressed by this work 6
  - 1.3.6 Wrapping it all up 9
- 1.4 Scope of this work 9

2 Fundamentals of radiation interaction with high purity germanium detectors 11
- 2.1 Introduction 11
- 2.2 The Detection Process 12
- 2.3 Photon Interactions with Matter 12
  - 2.3.1 Compton Scattering 13
  - 2.3.2 Photoelectric Absorption 14
  - 2.3.3 Pair Production 14
  - 2.3.4 Other forms of interactions 15
- 2.4 HPGe as a radiation detector 15
  - 2.4.1 Charge Carrier Mobility 18
  - 2.4.2 Statistics of charge collection 20
  - 2.4.3 Charge Impurity 22
- 2.5 Electronics 25

3 Charge Transport Simulation 28
- 3.1 Introduction 28
- 3.2 Charge Transport Code 28
  - 3.2.1 Field Solutions 29
  - 3.2.2 Charge Transport Dynamics 33
  - 3.2.3 Pulse Processing 34
  - 3.2.4 Verification and Validation 35

3.3 Charge Impurity Profile 36

4 Single from Multiple Site Rejection 40
4.1 Why we need it 40
4.2 Statistical Moments 44
4.2.1 Statistical Moments properties 44
4.3 Pulse Shape Discrimination 48
4.3.1 Introduction 48
4.3.2 Aalseth PSD Method 48
4.3.3 Analytical Model for PSD 53
4.3.4 Velocity and the PSD parameter space 54
4.3.5 Notes on PSD 56
4.4 Figure of Merit 58

5 A P-type Modified Electrode Detector: Overview of Detector Properties 60
5.1 Introduction 60
5.2 Motivation for the P-type Detector Geometry 61
5.3 Method 65
5.4 Results 69
5.5 Conclusion 73

6 Determination of the Impurity Profile for a PPC Detector 75
6.1 Introduction 75
6.2 Physics of HPGe Detector Capacitance 77
6.2.1 Electronic noise and capacitance 80
6.3 Capacitance Measurement 81
6.4 Impurity profile from Capacitance 83
6.5 Efficiency Method for Impurity Profile 85
6.6 Four point Resistance Measurement 87
6.7 Pulse Shape Library from a Scan 89
6.8 Conclusion 90

7 Position Resolution 91
7.1 Overview 91
7.2 Factors affecting position resolution 91
7.2.1 Intrinsic Factors 91
7.2.2 Technical Factors 93
7.2.3 Consequences 95
7.3 Effect of Anisotropic Drift Velocity 96
7.4 Effect of Finite Carrier Lifetimes 102
7.5 Optimizing a Geometry 106

8 Conclusion 112

8.1 Overview 112

8.2 Extension of this work to future $0\nu\beta\beta$ decay experiments 114

Bibliography 118

Appendices 130

Appendix A. Shockely Ramo theorem for calculation 131

LIST OF TABLES

Table 1.1 Characterization of the 5 enriched Heidelberg-Moscow HPGe detectors [1]... 5

Table 2.1 Common shallow donors and acceptors that can be used in high purity germanium semiconductors [2]. ... 23

Table 2.2 Segregation coefficients for elements in germanium as reported by Trumbore [3].The elements U,Th and K are not known but of particular interest as sources of background in HPGe detectors. ... 25

Table 3.1 Coefficients for the velocity equation Eq. 3.1 from [4]. ... 34

Table 7.1 Mass attenuation Coefficients, density, and thicknesses for the materials used in the measurement [5]. Dead layer thicknesses are typically "several hundered micrometers"[6]. ... 99

LIST OF FIGURES

Figure 2.1 Representation of the diamond lattice structure of high purity germanium. 16

Figure 2.2 The band structure of Germanium. Used with permission [2]. 16

Figure 2.3 The range of an electron of given energy in high purity germanium. 17

Figure 2.4 Comparison of the magnitude of the electric field for a coaxial HPGe detector with and without a charged impurities. The radius goes from an inner radius of 1.5 mm to an outer radius of 14 mm. The impurity density was given as constant at 0.0003 C/m^3. The black line illustrate the electric field at depletion at 100 Volts up to 150 Volts applied to the contact. The red line shows the electric field without charged impurities at 150 volts. 24

Figure 2.5 Impurity profile of a germanium ingot [7]. The crystal growth seed is located at the 0 % end of the crystal. 26

Figure 3.1 A simple HPGe detector showing cylindrical, spherical and conic shaped regions. 30

Figure 3.2 Illustration of how congruent solid geometry descriptions can represent complex geometries. Starting with a simple cylinder on the right, we can apply a subtraction of another smaller cylinder to produce a coaxial cylinder. We can then use a union to join another cylinder to the top to generate a semi coaxial detector shape. 31

Figure 3.3 Illustration of how a cylinder super-imposed on a Cartesian grid. In red are the grid points of a regular Cartesian grid. With the cylinder superimposed the blue shows the volume of our effective solution. 32

Figure 3.4 This figure demonstrates the relationship between each grid point and the super-imposed surface grid point. The Blue connections are pointers from each grid point to its neighbor. The Red connections are pointers to the surface grid point potential. These links have the correct distance to the correct nearest neighbor. These surface elements can be understood as the superposition of two different grid systems. These two grids allow us the ease of a regular Cartesian grid while using the surface grid to correctly enforce boundary conditions. The ability to build the surface grid in any non-uniform way allows for the construction of complex geometries. 33

Figure 3.5 The potential of a true cylindrical coaxial HPGe from simulation compared to the analytical solution [6]. 37

Figure 3.6 Comparison between simulated energy depositions uniformly distributed through an HPGe detector and the energy given after charge transport simulation. This type of systematic test shows that the energy is preserved across the crystal volume. This type of test also shows that charge is conserved as well. 38

Figure 4.1 The electron range in HPGe versus initial energy. The solid horizontal line shows the 1 mm electron path length close to 0.9 MeV. 43

Figure 4.2 Theoretical PSD parameter space with color indicating the distance between multiple interactions. 49

Figure 4.3 A current pulse with the 10% to 10% of the maximum enclosed in a box. The timming points needed are the start time, the end time and the time directly in the middle of these two, called the mid time. 50

Figure 4.4 The front back area and the half back area as measured from a current pulse. 51

Figure 4.5 The PSD line for single site events as the interaction point moves along the radius. The different lines indicate the effect of different combinations of drift velocities for electrons and hole respectively. 55

Figure 5.1 This notional diagram shows the comparison of an ordinary p-type detector (left) and a p-type point contact detector (right) showing a dead layer (dark), bulk p-type material (light), and an implanted contact on the central hole (thinned). . . 62

Figure 5.2 Impurity profile of a germanium ingot [7]. The crystal growth seed is located at the 0 percent end of the crystal. 64

Figure 5.3 Simplified schematic of a typical HPGe preamplifier circuit focusing on the contributions to the front end capacitance. The PPC preamp may or may not have a Feedback loop in the circuit. 67

Figure 5.4 Calculated depletion voltage for given values of minimum charge impurity and charge impurity profile. Dark to light shading represents low to high depletion voltage respectively. The computation was cutoff at 5000 V. The darkest shading represents 0 V. Imposing a lower bound of 1000 V would only remove a small region very close to the origin. 70

Figure 5.5 Calculated charge collection time surface parameterized by A and B. The prototype PPC showed a charge collection of up to 700 ns. 72

Figure 5.6 Capacitance versus bias voltage for the prototype PPC [8] compared with simulation. 73

Figure 6.1 Effects of a reverse bias on a p-n junction. As the voltage increases, the amount of the charge in both the acceptor and donor regions increase by the regions increasing in volume. 79

Figure 6.2 Capacitance measurement of a HPGe detector using injected voltage pulse, compared to ^{60}Co 1332 keV peak. 83

Figure 6.3 Iterating over a parameter space of the charge impurity profile, a fit to the capacitance was found. 85

Figure 6.4 The Number of counts for a collimated ^{60}Co source placed at four different heights versus the applied bias voltage of the University of Chicago PPC detector. As the applied voltage increases, the active volume increases thus the number of counts should increase proportionately. 87

Figure 7.1 Spectra for a 120% HPGe detector for a colimated ^{57}Co source at different angles to the front of the detector. 98

Figure 7.2 The relative dead layer thickness as parsed from the low energy efficiency. . 98

Figure 7.3 Rise time data extracted from the 122 keV peak of the ^{57}Co spectra. 99

Figure 7.4 A fit to the rise time extracted from the 122 keV peak of the ^{57}Co spectra at 25°. 100

Figure 7.5 The timing for full charge collection of electrons in a p-type HPGe versus angle. The error bars indicate the FWHM of the peak. 100

Figure 7.6 The velocity of holes in a p-type HPGe versus angle. Including corrections for dead layer thickness. 101

Figure 7.7 A plot of the charge carrier lifetime limit in high purity germanium at 77 k versus path length and electric field strength. This is for holes and is the loss of energy given a 1 MeV energy deposition with $\tau < 1E-4$ seconds [6]. 104

Figure 7.8 A plot of the total charge carrier drift time in the UC PPC versus the 10-90% rise time of the integrated current pulse. For the 1332.5 keV gamma of a ^{60}Co source tagged with a NaI detector. Data courtesy of Phil Barbeau and Juan Collar at the University of Chicago. 106

Figure 7.9 A plot of the Energy versus the duration for the UC PPC. 107

Figure 7.10 Representation of the geometric parameter space. We can see the change in diameter and height for the parameter space in question. 108

Figure 7.11 A ^{232}Th spectrum illustrating the PSD method used to remove most of the multiple site events while retaining most of the single site events. Using these peaks from this type of spectrum follows the method outlined in [9]. 110

Figure 7.12 The resulting figure of merit interpolated for the geometric parameter space shown in Fig. 7.10 of different radii and heights for a simple Point Contact Detector design. 111

Figure 8.1 Parameterized model for for simulation of the detector response. 115

Figure 8.2 Total parameterized model for general consideration of physics experiments. 117

Chapter 1

Motivation

1.1 Overview

Modern nuclear and particle physics experiments analyze individual pulse shapes from many different detector geometries to help characterize the interaction giving rise to a particular detected event. A complete model of the detector's response, for each physical region and each type of detected event can be helpful in the analysis of experimental data and may also be key in optimizing the detector design and configuration before the experiment begins. For instance, the utility of certain detector schemes depends critically on the pulse-by-pulse analysis of events to categorize them as single or multiple site. The response of the detector (or the segment of the detector) to these two classes of events is critical in determining if a design is worth the additional cost, schedule delay, or difficulty in handling. Modelling the response to individual energy depositions can help differentiate among different detector configurations and guide the optimization of detector material, size, electrode configurations and even relative placement.

Many backgrounds anticipated in next-generation neutrinoless double-beta decay searches involve multiple photon interactions. In contrast, neutrinoless double-beta decay events deposit all of their energy at a single interaction location. Thus, event multiplicity is a desirable way of discriminating signal from backgrounds. Event multiplicity discrimination is done by decomposing detector signals using a basis, or library of pulse shapes corresponding to interactions at each position in a detector. The single from multiple site resolution of pulse-shape analysis depends on the accuracy of this library. A library is built in two ways; a long and difficult experimental campaign, or using a highly-accurate, verified model of the pulse formation process.

This first chapter outlines the physics needs which motivate our work, namely the need of better detectors and detection methods to farther our limited knowledge of the nature of neutrinos. To this end, a brief overview of neutrinos is given. In particular, neutrino mass provides the motivation for several current and historic physics experiments each of which may benefit from an increased pulse shape discrimination ability. These experiments rely on the solid state technology of high purity germanium detectors. Several needs are discussed about a single experiment, yet applicable to an entire series of experiments: the ability to do pulse-by-pulse analysis, the need for extremely low background and the need for detector material on the ton scale.

Double beta-decay is an extremely rare process in which the charge of the nucleus changes by two owing to a second order charged current weak interaction [10, 11, 12]. Neutrinoless double beta decay is a double beta decay in which the neutrino acts as its own antiparticle, and no neutrinos are actually emitted. This process has never been observed, but it can only occur if the neutrino is a Majorana particle and is therefore its own antiparticle. The decay rate is also proportional to the mass of the neutrino squared. The unique information these measurements provide, place them as one of the highest priorities of the nuclear physics communities [13, 14, 15].

1.2 Introduction

1.2.1 Neutrinos

Neutrinos are a particle originally proposed by Enrico Fermi to retain the principle of conservation of energy in beta decay. Neutrinos are spin 1/2 particles with no charge, and known to have mass[16]. There are many unique and wonderful properties of neutrinos which include but are not limited to its oscillating between three distinct states, each of which with a unique mass matrix. As a result propagating neutrinos do not have a unique mass, but are a superposition of mass states.

The fact that neutrinos have masses and oscillate between mass eigenstates represents the first real extension of the standard model of particle physics since it was formulated [17] and has generated tremendous interest in the physics community. These experiments have grown steadily larger and more complex[18]. A key remaining question is whether a neutrino has a Majorana mass term [19].

Double beta decay is an extremely rare process in which the charge of the nucleus changes by two due to the second order charged-current weak interaction. Neutrino-less double beta decay is a double beta decay in which the neutrino acts as its own antiparticle, and no neutrinos are actually emitted [20]. This process has never been observed, but it can only occur if the neutrino is a Majorana particle and is therefore its own antiparticle. The decay rate is also proportional to the mass of the neutrino squared. Because of the unique information these measurements provide, they have become one of the highest priorities of the nuclear and particle physics communities.

1.3 Motivation

The basic operating premise for HPGe neutrinoless double beta decay experiments is to use the ”target” mass is also the active detector[20]. This strategy utilizes the ^{76}Ge isotope as a semiconductor detector. This strategy has, to date, placed the most stringent limits on neutrinoless double beta decay rates [21, 1]. Many new experiments intend to extend this limit [14], this work focuses on two such experiments, the GERDA [22] and Majorana [23] experiments.

1.3.1 IGEX

The International Germanium Experiment (IGEX) was a search for neutrinoless double beta decay using approximately 6.5 kilograms of isotropically enriched to 86% in ^{76}Ge. Three p-type detectors of $\sim$ 2kg each and three detectors of $\sim$ 1 kg each collected data in three laboratories: Homestake gold mine(4000 meters water equivalent(mwe)), Canfranc Tunnel (2450 mwe) and Baskan Neutrino Observatory (660 mwe). The detectors had a detection efficiency of almost 100% relative to a 7.62 cm ×7.62 cm cylindrical NaI(Tl) detector for a 1332 keV gamma peak. The total energy resolution of the summed data was interpolated to be $\sim$ 4 keV at 2038 keV. IGEX used unique cryostat technology, ultra-low background materials, ancient lead shielding, and pulse shape analysis to maximize the signal to noise ratio.

1.3.2 Heidelberg-Moscow

The HEIDELBERG-MOSCOW experiment used 10.96 kg active mass of 86% enriched ^{76}Ge into five p-type HPGe detectors. The experiment ran August 1990 to May 2003 in the Gran-Sasso underground laboratory(3500 mwe). Four of these detectors were placed in a common shield. In the construction of the cryostat, mainly made of electrolytic Cu, only selected and cleaned low-level materials were used. Materials were stored underground to minimize the activation due to cosmic rays [24].

All detectors except detector No. 4 were operated in a common Pb shielding of 30 cm of Pb, the 10 cm closest to the detectors were radio-pure LC2-grade Pb. The entire cryostat is placed in an air-tight steel box pressurized with radio-pure nitrogen in order to suppress the ^{222}Rn contamination of the air [1].

Table 1.1: Characterization of the 5 enriched Heidelberg-Moscow HPGe detectors [1].

Technical parameters of the five enriched detectors				
Detector	Total mass [kg]	Active mass [kg]	Enrichment in ^{76}Ge [%]	FWHM at 1332 keV [keV]
No. 1	0.980	0.920	85.96±1.3	2.226±0.02
No. 2	2.906	2.758	86.66±2.5	2.436±0.03
No. 3	2.446	2.324	88.36±2.6	2.716±0.03
No. 4	2.400	2.295	86.36±1.3	2.146±0.04
No. 5	2.781	2.666	85.66±1.3	2.556±0.05

1.3.3 GERDA

GERmanium Detector Array (GERDA) experiment is an array of 86% isotopically enriched ^{76}Ge detectors, submerged in liquid argon for both shielding and cooling [25, 26]. The argon is very radon pure and will be surrounded by water as a low-Z shield. The liquid argon will act as an active shield as well as a bulk shield to the HPGe detectors inside. This experiment has three phases. The first phase will combine the five detectors from the Heidelberg-Moscow experiment with the three ∼ 2 kg detectors from the IGEX experiment. GERDA will reduce the background lower then both Hiedelberg-Moscow and IGEX by using ultra-clean materials, pulse shape analysis, segmentation, and novel shielding with liquid argon.

1.3.4 Majorana

The Majorana collaboration proposes to operate 500 kg of 86% enriched Ge detectors seperated into 60 kg modules. The cryostat's will be constructed using electro-formed copper[27], to avoid the production of radioactive impurities by cosmic ray activation the copper will be electroformed underground. Presently, electrode configurations for Ge detectors are under study to check the impact of parameters such as segmentation and granularity on signal and background. The research and development phase will begin with a demonstrator module with 30-60 kg of enriched and unenriched HPGe detectors. The goal is to reach a background of less than 1 counts/ton/keV/y in the energy region of interest around 2038 keV through the use of ultrapure materials, improved pulse shape discrimination, and detector granularity to reject multiple site events corresponding to background events [11, 23].

1.3.5 Necessary advances addressed by this work

All of these experiments have used, or have proposed using high purity germanium as both the source and the detector of the neutrino less double beta decay signal. Results are recorded as lower limits and the reader is referred to the Particle Data Group publication for their comparison [28]. In order to place stringent limits on the neutrino signal, many sources of background must be suppressed as much as possible.

Pulse Shape Analysis

The availability of digital electronics capable of recording and analyzing pulses from an HPGe detector system has enabled the continued advancement of detector technology and experimental sensitivity. Previous experiments would typically use sophisticated analog electronics to reduce backgrounds by triggering on the pulses of interest, defined by some criteria, and extract information such as the energy and timing of the event. By digitizing the analog signals on the nanosecond time scale, we can easily record the pulse for off-line analysis. This Pulse Shape Analysis **(PSA)** for HPGe detector systems allows for the extraction of information about the event that was difficult if not impossible in previous systems [29].

With the ability to record and analyze each pulse a new door has opened. In addition to the energy of the incident interaction, geometrical localization of the event can be extracted [30]. Multiple site events can be separated from single site events. Even gamma ray tracking can be done to locate the source position relative to the detector [31].

The electronic noise is a fundamental limitation of any PSA method. Charge carrier production in an ionizing event has fluctuations described by the Fano factor. There is thermal noise in the solid state detector and there is noise in the electronics. Where possible, all of these sources must be minimized to extract the maximum amount of information from the signal.

Low Background

The half life of neutrinoless double beta decay in ^{76}Ge is greater than 1.2×10^{25} years [14, 32]. With such a small decay rate, true decay events will be very few and far between. In order to tell the signal of interest from the background radiation, all backgrounds must be minimized. Existing experiments have gone to great lengths to minimize backgrounds, however future experiments must go further. Experiments must be located deep underground with both passive and active shielding to reduce high energy cosmic backgrounds. Ultrapure materials must surround the detectors to reduce local radiological backgrounds. In short, every means within the resources available to the experimenters must be utilized to drive backgrounds low enough to see such rare events.

One source of background is the detector itself [33]. Even though these detectors are made of a high purity germanium, the highest purity material known to man [6], there still exists a radioactive contamination in the detector. Two of the most troublesome contaminants are U, Th and K. Also, when exposed to cosmic radiation, as is present on the earths' surface, detector material can be transformed into radioactive isotopes such as ^{57}Co, ^{60}Co,^{68}Ge.

1 Ton

As mentioned earlier, the decay rate of the signal of interest is exceedingly small. One way to increase the likelihood of seeing a signal, assuming that the background is low enough, is simply to increase the amount of mass. Current calculations indicate that at least 1 ton of material is needed to achieve a statistically significant result within 10 years for a Majorana neutrino mass of ≈ 50 eV. A common HPGe detector is between 1/2 and

1 kg, with up to 2 kg detectors possible. There are, however, limits to the size of a crystal that can be made and this means that arrays of detectors must be used to establish 1 ton of active mass.

1.3.6 Wrapping it all up

There are many more factors to consider. The ones listed above are the ones directly affected by this work. In order to maximize our ability to do pulse shape analysis, an electronic model of each detector must be made. The better the model, the better our ability to discriminated between signals of interest and noise. The number of detectors necessary, combined with the very urgent need to minimize the time spent above ground dictates that any characterizations needed above ground must be done quickly. The number of detectors limits the amount of characterization time that can be spent on each detector. Optimizing the performance of an array of HPGe detectors involves a delicate trade off between ease of characterization, background reduction capability, and intrinsic background introduced by the instrumentation required for signal readout. As the parameters of this problem have clarified, so has the opportunity for new detector geometries and analysis methods to make an impact.

1.4 Scope of this work

This work includes investigation of a new method to quickly characterize high purity germanium detectors. The new method is a simple two hour test that can be preformed with no more than a working detector, suitable electronics and a pulser. Our method is compared and contrasted with other methods to obtain the same information. Each alternative is found inadequate or too time consuming to be viable. A second key method is introduced for optimization of the design parameters using simulations of HPGe response and the actual analysis software to maximize the signal to noise ratio in the region of interest. An example of this method optimizes a novel detector design and optimizes the height and diameter of the detector to maximize a specific analysis method. As such, this work provides current experiments a method to quickly optimize the efficacy of pulse shape analysis methods while minimizing ingrown backgrounds and remaining tractable for performing in an experiment with a large number of detectors.

Chapter 2

Fundamentals of radiation interaction with high purity germanium detectors

2.1 Introduction

The interaction of a photon with the detector material results in all or part of the photon's energy being transferred to one or more charged particles. These charges are transported through the detector and collected, producing an electrical signal which can be recorded and analyzed to extract information such as the energy and location of the interaction.

Pulse shape analysis of photon interactions with high purity germanium semiconductor detectors requires an understanding of the physical processes associated with the interaction of electromagnetic radiation with matter, the basic properties of germanium semiconductor as related to its use as a semiconductor detector, and the factors involved in the electronic signal formation within the detector material. Each aspect contributes to the ability to accurately model and analyze pulse shapes formed by photon interactions.

2.2 The Detection Process

A detector will produce an electrical signal that contains information from the photon interaction. In addition to the energy it has deposited in the detector, other information is available as well. The detection of photons is an indirect process, involving an interaction between the photon and the detector material that results in all or part of the energy being transferred to one or more charge carrying particles. From one keV to tens of an MeV the interaction mechanisms that a photon can undergo in a solid state detector are restricted to photoelectric absorption, Compton scattering and electron-positron pair production. The relevance of each interaction mechanism as a function of energy will be investigated in subsequent sections.

An HPGe detector with an appropriate contact forms a p-n junction [6]. This junction is reverse biased by applying the appropriate voltage to the appropriate detector contact, creating an electric field across an empty conduction band. A photon moving through the region can interact through processes of photoelectric absorption, Compton scattering or electron-positron pair production. Photon interactions result in all or part of the energy being transferred to the charge carrying particles, traversing the forbidden band gap of the crystal lattice to the conduction band which are then swept away to the contacts by the electric field. The signal formed by the movement of this charge contains the information of the interaction.

2.3 Photon Interactions with Matter

As mentioned previously, there are three main photon interactions considered in this thesis. In the most general form, we have the statistics formula for the photon interaction probability.

$$I = I_0 e^{-\mu x} \tag{2.1}$$

where x is the distance traveled in the the material and μ is the probability per unit length of removal of that photon called the linear attenuation coefficient [34]. The linear attenuation coefficient μ has three contributions:

$$\mu = P_{PA} + P_{CS} + P_{PP} \tag{2.2}$$

The P_{PA} is the probability per unit length of photo absorption. The P_{CS} is the probability per unit length of Compton scattering. The P_{PP} is the probability per unit length of pair production. Each probability can be expressed as a cross section as $P_i = \sigma_i NZ$

Note that this formula applies to a specific material and photons at a specific energy. It cannot account for altering of the energy or production of new photons of any other methods. This is a limited methodology.

2.3.1 Compton Scattering

For the probability of Compton scattering above the probability is given by $P(\sigma) = \sigma_c NZ$ where N is the number of atoms and Z is the atomic number. The the differential cross section per electron, σ_c, is given by the Klein-Nishina formula:

$$\frac{d\sigma}{d\Omega} = r_0^2 \left(\frac{1}{1+\alpha(1-cos\theta)}\right)^2 \left(\frac{1+cos^2\theta}{2}\right) \left(1 + \frac{\alpha^2(1-cos\theta)^2}{(1+cos^2\theta)[1+\alpha(1-cos\theta)]}\right) \tag{2.3}$$

where α is the photon energy in units of the electron rest energy $\alpha = E_\gamma/mc^2$. The r_0 is a parameter given by $r_0 = e^2/4\pi\epsilon_0 mc^2 = 2.818$ [34].

2.3.2 Photoelectric Absorption

The photoelectric effect is the main interaction mechanism for photons at low energies (up to about 200 keV for Ge). The photon interacts with an atom in such a way that the entire photon energy is transferred to a bound electron which leaves the atom. The energy of the resulting free electron is given by the difference between the energy of the photon $h\nu$ and the binding energy of the electron E_b

$$E = h\nu - E_b \tag{2.4}$$

The nucleus will recoil due to conservation of the impulse. Photons undergoing photoelectric absorption are predominantly absorbed by the K shell electrons. Part of the binding energy E_b will be transferred to X-rays emitted from the atom when the vacancy left by a photoelectron is filled by a less bound electron. The X-rays are in turn absorbed by the other atoms producing further photoelectrons.

The probability of photoelectric absorption is given as the cross-section:

$$\sigma_{pe} = k_{pe} \cdot \frac{Z^{4.5}}{E_\gamma^3}, \tag{2.5}$$

where k_{pe} is a proportionality constant, Z is the atomic number of the material, and E_γ is the energy of the incident photon [35]. For compounds, the different atomic numbers (Z) are averaged according to their weight fractions. The probability of interaction occurring at constant atomic densities is proportional to the path length of photon through the detector.

2.3.3 Pair Production

Pair production is the production of electron-positron pairs in the presence of an electromagnetic field due to the presence of a near by massive atom. The conservation of energy gives the equation:

$$E_\gamma = T_+ + T_- + 2mc^2 \tag{2.6}$$

Thus no pair production happens below 1.022 MeV.

No simple expression exists for the probability of pair production per nucleus, however an empirical formula exists for the cross section for high energies. For photon energies $E >> 20$ MeV the cross section has roughly a Z^2 dependence. It can be written

$$\sigma_{PP} = 4\alpha r_0^2 Z^2 \left(\frac{7}{9} ln \left(\frac{183}{Z^{1/3}} \right) - \frac{1}{54} \right) \tag{2.7}$$

where α represent the fine structure constant [36].

The electron and positron produced then can further interact with the detector material through several means. The charges can produce additional photons by annihilation or Bremsstrahlung in strong electric fields.

2.3.4 Other forms of interactions

In addition, photons can undergo Rayleigh scattering, Thompson scattering and muon-antimuon pair production. These processes are typically not important in double beta decay experiments, and so we do not consider them further, for a more extensive review see [36, 35, 33].

2.4 HPGe as a radiation detector

Germanium and silicon are semiconducting material which can be made to exceedingly high purity standards [7]. They can also be made into very large crystals. A crystal of germanium is made from germanium atoms arranged in a diamond lattice, as in Fig. 2.4.

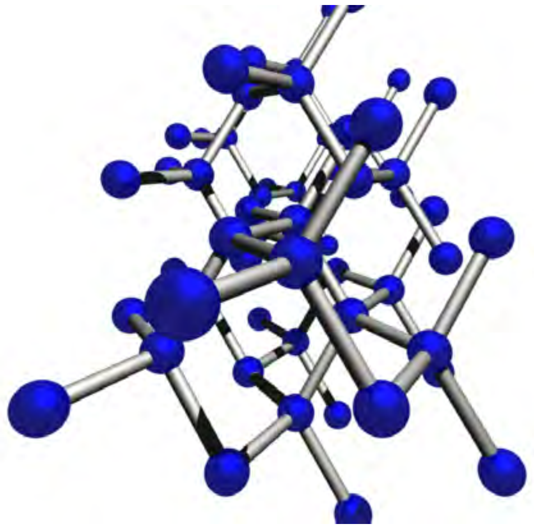

Figure 2.1: Representation of the diamond lattice structure of high purity germanium.

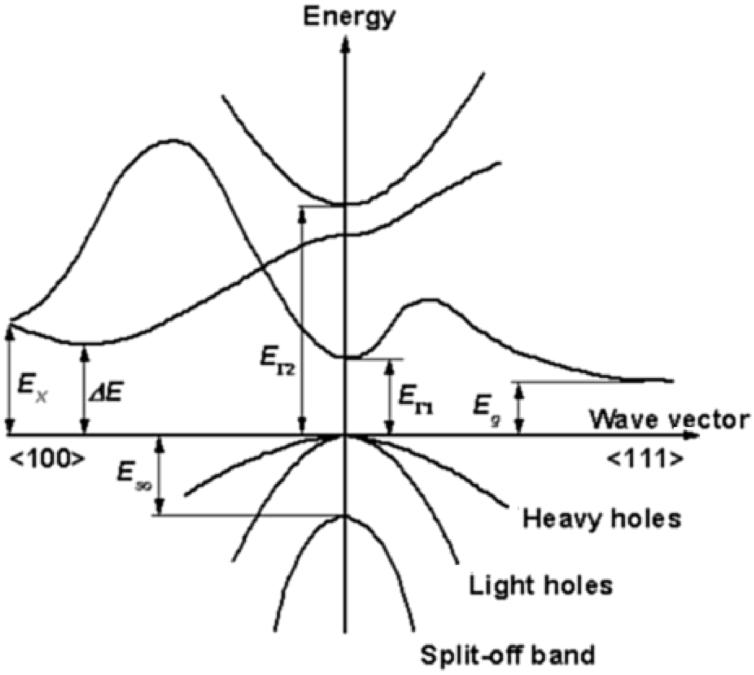

Figure 2.2: The band structure of Germanium. Used with permission [2].

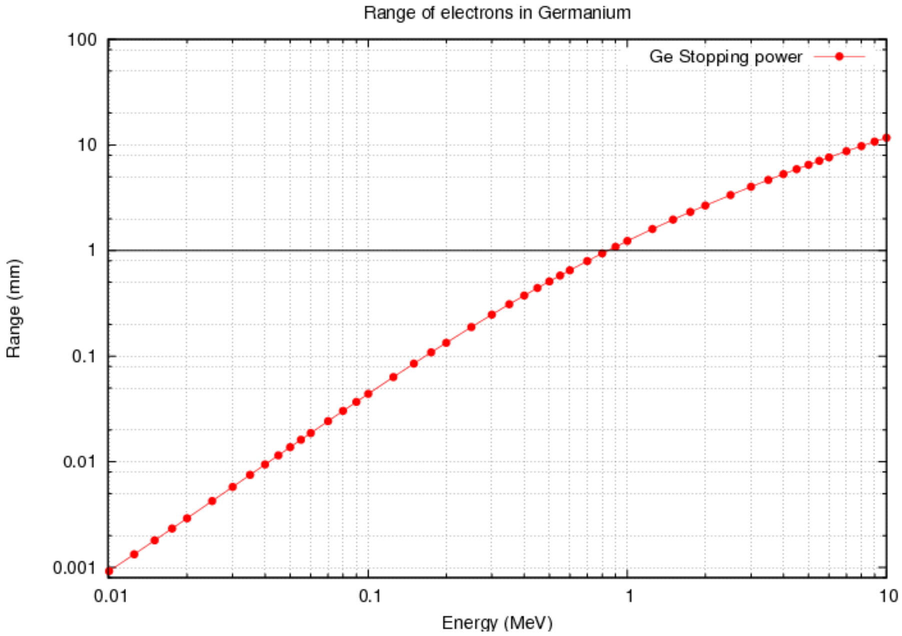

Figure 2.3: The range of an electron of given energy in high purity germanium.

Germanium atoms arranged in a diamond lattice are close enough that their orbital electron shells of overlap. Given the Pauli exclusion principle and multiple atoms, the electrons form bands in the allowed energies they can take. As more atoms are brought into the diamond lattice, more electrons fill the allowed energy band. For semiconductors, there exist both allowed and forbidden energy bands.

The outer most electrons are only loosely bond to the atom. When the atoms come together to form a semi-conductor crystal lattice these outer electrons form an energy band called the valence band. Above this is the forbidden band which no electron can occupy. Above this is called the conduction band. In the conduction band electrons are free to move around the crystal.

Electrons in the conduction band are not geometrically free to zip through the crystal. From Newtons laws we know that a mass will move in a straight line until acted on by a force, its momentum is constant unless changed by a force. This is true of electrons traveling in the conduction band of a crystal. The changes in the charge carriers momentum as they scatter through the crystal lattice gives rise to the concept of resistance in a conducting material. The motion of electrons in a crystal lattice is only approximately a classical process, described by quantum mechanics through a Bloch wave-function. This wave-function describes an electron traveling through a crystal lattice and can be used to accurately calculate the band structures of a semiconductor in a self consistent manner.

2.4.1 Charge Carrier Mobility

The model of charge carriers in a semiconductor used by many radiation textbooks [6, 36] is derived from the Drude model. The model of conduction would be simple if it were not for [37]:

1. Scattering which depends on $\mathbf{k}$ and $\mathbf{q}$
2. Statistical effects of electron propagation of multiple electrons
3. Band structure effects

Using the Drude model of conduction we can easily bypass these processes with averaging. We begin with Newton's second law:

$$m\dot{\mathbf{v}} = \mathbf{F_0} \tag{2.8}$$

To include effects of the band structure we would replace the mass (m) with the effective mass (m^*) [38]. In order to avoid we an ever increasing velocity we add a frictional force:

$$m^*\dot{\mathbf{v}} = \mathbf{F_0} - m^*\frac{\mathbf{v}}{\tau} \tag{2.9}$$

Letting $\mathbf{F_0}$ go to 0 we have a solution for the velocity $\mathbf{v} \propto e^{-\frac{t}{\tau}}$ with τ as the decay time constant. In the presence of an electric field the force is $\mathbf{F} = q\mathbf{E}$ giving:

$$m^*\dot{\mathbf{v}} = -e\mathbf{E} - m^*\frac{\mathbf{v}}{\tau} \tag{2.10}$$

combining this equation with the assumption of steady state we have:

$$m^*\dot{\mathbf{v}} = 0 = -e\mathbf{E} - m^*\frac{\mathbf{v}}{\tau} \tag{2.11}$$

Solving for the velocity we have:

$$m^*\mathbf{v} = e\mathbf{E}\tau \tag{2.12}$$

We know from Ohm's law that the current density is defined as $\mathbf{j} = \sigma\mathbf{E}$. From electrodynamics [39] we have the current density is given by $\mathbf{j} = en\mathbf{v}$. Plugging in v from above we have:

$$\mathbf{j} = en\mathbf{v} = \frac{e^2\tau n}{m^*}\mathbf{E} = \sigma\mathbf{E} \tag{2.13}$$

where σ is the conductivity, $\sigma = \frac{e^2\tau n}{m^*} = en\mu$, and μ is the mobility. This model is good for low field, low frequency conduction where the velocity is on average isotropic in the semiconductor, such as exist in HPGe detectors.

The source of the frictional force is scattering through the crystal lattice. By far the most important scattering process for low energy electrons affecting conductivity is lattice vibrations (phonons) [37]. Phonons take energy away from the electrons and keep them energetically close to the conduction band edge. There are other scattering mechanisms, which are elastic but still influence the conduction substantially. Among these are scattering by charge impurities, neutral impurities, and surfaces. Phonons traverse the crystal lattice as well and scatter by impurities in the crystal lattice as well as different isotopes of which the crystal is composed

In this model we have the velocity as a function of the electric field strength $v = \mu|E|$ where the coefficient is given by $\mu = e\tau/m^*$. The electrons scattering through the crystal lattice gives rise to an effective mass of the charge carriers. This lattice dependence also introduces a directionality to the effective mass, thus an effective mass is a tensor relative to the crystal lattice. This directionality, coupled with the electric field results in a directional dependence of the velocity in the crystal lattice as well. This directionality in the charge carrier velocity is called the anisotropic drift velocity.

2.4.2 Statistics of charge collection

To understand the statistics of electron-hole pair production, let us assume that the energy deposited by the incident radiation goes into causing lattice excitations and ionization. If ϵ_i and ϵ_x represent the average energies needed to produce ionization and excitation respectively, then the total deposited energy can be written as

$$E_{dep} = \epsilon_i n_i + \epsilon_x n_x \tag{2.14}$$

where n_i and n_x represent the total number of ionization and excitations produced by the radiation. If we now assume that these processes follow Poisson statistics, it would mean that the variance in the number of ionization and excitations can be written as

$$\sigma_i = \sqrt{n_i} \tag{2.15}$$

$$\sigma_x = \sqrt{n_x} \tag{2.16}$$

These two variances are normally not equal because of differences in the thresholds for excitation and ionization processes. However if we weight them with their corresponding thresholds, they should be equal for a large number of collisions, i.e.,

$$\epsilon_i \sigma_i = \epsilon_x \sigma_x \tag{2.17}$$

$$\epsilon_i \sqrt{n_i} = \epsilon_x \sqrt{n_x} \tag{2.18}$$

Combining this with equation 2.14 gives

$$\sigma_i = \frac{\epsilon_x}{\epsilon_i} \left[\frac{E_{dep}}{\epsilon_x} - \frac{\epsilon_i}{\epsilon_x} n_i \right]^{1/2} \tag{2.19}$$

Let us now denote the average energy needed to create an electron-hole pair by w_i. Note that this energy includes the contribution from all other non-ionizing processes as well. This means that it can be obtained simply by dividing the total deposited energy by the number of electron-hole pairs detected n_s. Hence we can write

$$w_i = \frac{E_{dep}}{n_s} \tag{2.20}$$

or

$$n_s = \frac{E_{dep}}{w_i} \tag{2.21}$$

If we have a perfect detection system that is able to count all the charge pairs generated, then we can safely substitute n_s for n_i. In this case the above expression for σ_i, yields

$$\sigma_i = \left[\frac{\epsilon_x}{\epsilon_i} \left(\frac{w_i}{\epsilon_i} - 1 \right) \frac{E_{dep}}{w_i} \right]^{1/2} \tag{2.22}$$

Using $E_{dep}/w_i = n_s$, this can be written as

$$\sigma_i = \sqrt{F n_s} \tag{2.23}$$

where

$$F = \frac{\epsilon_x}{\epsilon_i} \left(\frac{w_i}{\epsilon_i} - 1 \right) \tag{2.24}$$

is called the Fano factor. It is interesting to note here that even though we assumed that the individual processes of ionization and excitations were Poisson in nature, but the spread in the output signal can be described by the Poisson process only if we multiply it by another factor. The reason, of course, is that these processes are not uncorrelated as required by a strictly Gaussian process. The Fano factor was first introduced to explain the anomaly between the observed and expected variance in the signal [40]. The simple calculations we performed above do not produce very accurate results and they were only meant to motivate the Fano factor. For detailed calculations see van Roosbroeck, W and Alkhazov.

2.4.3 Charge Impurity

The impurities found in a HPGe crystal play a crucial role in the operation of the crystal as a radiation detector. Impurities have many classifications depending on their effect. Uncharged impurities are elements in the crystal lattice with strongly bound electrons such that they contribute minimally to the electrical properties of the crystal. These impurities can however decay producing an internal source of background to signals of interest. For many $0\nu\beta\beta$ decay experiments using HPGe detectors, impurities that can contribute background to the region of interest are U,Th,K [41, 42, 43, 44, 24]. Impurities are removed through the method of zone refining [7, 45]. The model for how impurities move during zone refining is given as:

$$N = N_0 k (1 - L)^{k-1} \tag{2.25}$$

where N_0 is the concentration of the impurity in the starting melted germanium, L is the fraction of the original melt has solidified, k is the segregation coefficient of the impurity. Known segregation coefficients are listed in Table: 2.2.

Charged impurities are those elements which contribute significantly to the electrical properties of an HPGe crystal. Of these type of impurities are donors and acceptors. Donors have a loosely bound electron which it shares with the germanium crystal lattice. Acceptors are the opposite of donors in that they want to loosely accept an electron from the crystal lattice. Charged impurities play a crucial role in HPGe detectors. At the purity levels germanium crystal are grown, manufactures must add charged impurities to make a functional HPGe detector, these are referred to as dopant's. The need for dopant's is illustrated in Fig. 2.4. The electric field without the dopant's is very high at the inner contact and very low at the outer contact, resulting in very poor charge collection. The application of large voltages cannot compensate. By doping the high purity material with the appropriate donors or acceptors, the initially neutral material must remove the donor or acceptor charge leaving behind a net charge which extends the electric field through the entire volume. Dopant's enable high purity germanium detectors. Many common dopant's are used in HPGe detectors, many common in the semi-conductor industry are listed in Table: 2.1. All High purity material

Table 2.1: Common shallow donors and acceptors that can be used in high purity germanium semiconductors [2].

Common dopant's for use in Germanium					
Shallow Donors	As	**P**	Sb	Bi	Li
Shallow Acceptors	**Al**	B	Ga	In	Tl

After the material is zone refined and the proper dopant's added, it is fabricated into a large single crystal by the Czochralski method [45]. This method involves growing a single crystal from melted material in a quartz crucible. The system is heated by a radio frequency induction coil wrapped around the crucible in a process called RF heating. A

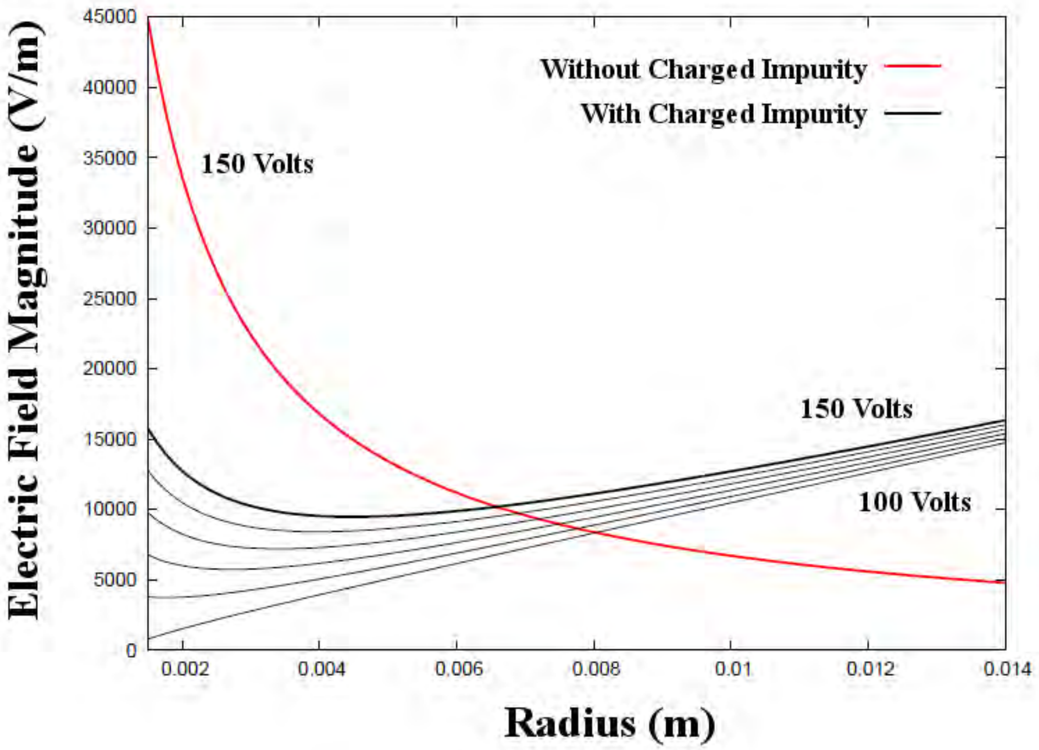

Figure 2.4: Comparison of the magnitude of the electric field for a coaxial HPGe detector with and without a charged impurities. The radius goes from an inner radius of 1.5 mm to an outer radius of 14 mm. The impurity density was given as constant at 0.0003 C/m^3. The black line illustrate the electric field at depletion at 100 Volts up to 150 Volts applied to the contact. The red line shows the electric field without charged impurities at 150 volts.

Table 2.2: Segregation coefficients for elements in germanium as reported by Trumbore [3].The elements U,Th and K are not known but of particular interest as sources of background in HPGe detectors.

Elemental Segregation Coefficients in Germanium			
Element	Coefficient	Element	Coefficient
Co	1.00E-06	Sb	3.00E-03
Zn	4.00E-04	Li	0.002
Mn	1.00E-06	As	2.00E-02
Fe	3.00E-05	P	8.00E-02
Tl	4.00E-05	B	17
Bi	4.50E-05	U	-
P	8.00E-02	Th	-
Pt	5.00E-06	K	-
Cd	$>$ 1E-05	Ag	4.00E-07
V	$<$ 3E-07	In	0.001
Au	1.30E-05	Si	5.5
Cu	1.50E-05	Pb	1.70E-04
Al	7.30E-02	Bi	4.50E-05
Ga	8.70E-02	Te	1.00E-06
Sn	2.00E-02	Ni	3.00E-06

small dislocation free seed crystal is slowly pulled out of the melt as the material solidifies into a single crystal. The seed is rotated as it is pulled to obtain a cylindrical ingot. To prevent absorption of impurities the process takes places under argon gas [7].

2.5 Electronics

One of the key components in modern detector systems is the electronics readout system. Many experiments and detector systems use many different electronics technologies, however the all share the same basic principles for the electronic readout and optimization of signal to noise ratio. Ultimately, the purpose of these pulse processing systems is to:

1. Acquire electrical signal from the detector.

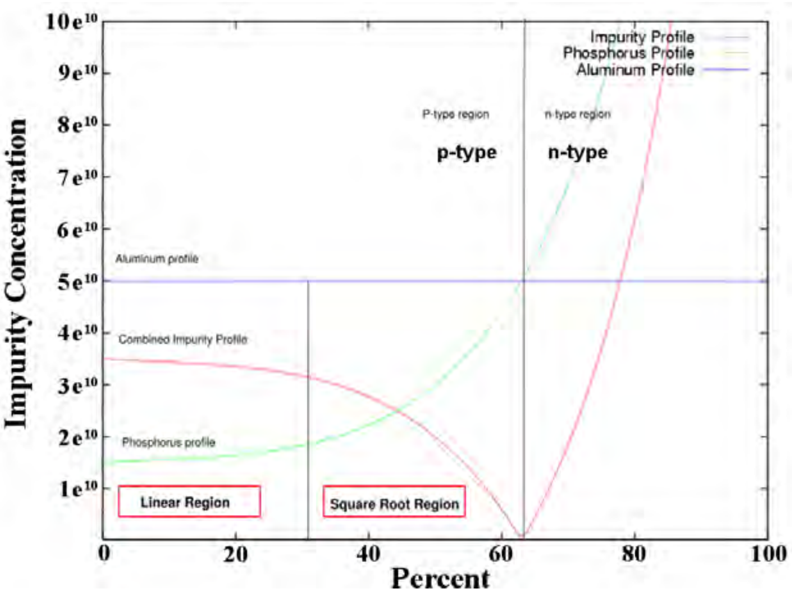

Figure 2.5: Impurity profile of a germanium ingot [7]. The crystal growth seed is located at the 0 % end of the crystal.

2. Optimize the response of the system to:
    - the minimum detectable signal
    - energy measurement
    - event rate
    - timing
    - insensitivity to variations in the pulse shape due to detector characteristics
3. Digitize and store the signal for subsequent analysis

Generally, these properties cannot be optimized simultaneously, so compromises are necessary. In addition to these primary properties of the electronics readout system, other considerations can be equally important like: resistance to radiation damage, low power, portable, temperature, etc.... Many modern and accessible texts exists so the topic of electronics will not be discussed any further here except when necessary.

Chapter 3

Charge Transport Simulation

3.1 Introduction

The Shockely-Ramo theorem is the basis for charge transport simulation in High Purity Germanium (HPGe) detectors [46, 47, 48]. In this chapter we review this method and present a computer code (CRT) to perform charge transport simulations in HPGe detector. We discuss the most significant input parameters such as the geometry and impurity profile.

3.2 Charge Transport Code

Our charge transport code developed solves for the potential of a complex geometrical germanium detector in three dimensions. The code was developed from scratch for many reasons, including the high cost of commercial software to the scientific community in general, and the lack of free software capable of solving for complex three dimensional geometries in particular. Instead of patching several programs and data formats together a complete solution provides seamless compatibility, as well as high level transparency. Finally, being general in the scope of the geometry but specific in the ultimate form of the solution provides for efficient development, computational efficiency and design stability.

An accurate, verified model of the pulse shape formation process is needed. Such an accurate simulation model has been developed **(CRT)**, with experimental validation. The model covers aspects necessary to completely describe the pulse formation process:

(1) Modeling of the electric fields, with and without space charge effects.

(2) Transport of the deposited charge, including second-order effects such as drift velocity anisotropy from lattice orientation effects.

(3) Calculation of induced charge signals, using the weighting field formalism.

(4) Convolving with the electronic response of the analog readout system, e.g. a charge-integrating preamplifier.

3.2.1 Field Solutions

CRT can solve for the fields given the applied voltages, the geometry and the charged impurity profile. Solving for the electric field in a given region is most easily done by first solving for the potential. Given boundary conditions, the relaxation method [39] is a simple yet powerful method of solving the potential in the bounded region. However, it proves difficult to solve the boundary conditions do not match up with the grid coordinate system being used. HPGe detectors are often of very complex shapes and most often include cylindrical and spherical regions.

Figure 3.1: A simple HPGe detector showing cylindrical, spherical and conic shaped regions.

Geometry

The geometry is described with Congruent Solid Geometry, where simple shapes are operated on by a subtraction, intersection, or a union of one of more shapes to another. A simple implementation of this method allows for the combination of simple shapes to accurately represent a complex volume. The shapes are combined with the relevant material properties. With the description of the geometry a Cartesian grid is built and superimposed with a surface grid. The surface grid imposes the proper boundary conditions of the geometry on the fields. Given a charge density profile, the code can then solve for the necessary electric and weighting fields.

CRT constructs geometries using derived classes for each simple shape. Adding a derived object that performs a Union, Intersection, or Subtraction function on two objects we can make complex volumes from simple ones. We pass the constructed object to a logical class providing material information about the object, like its permittivity or density.

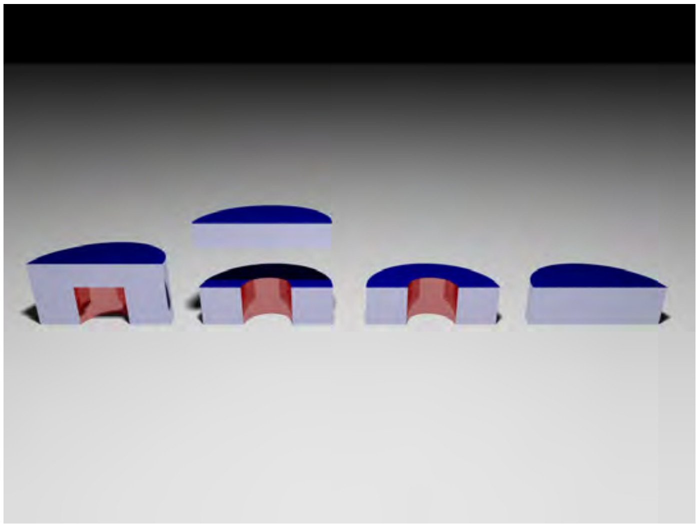

Figure 3.2: Illustration of how congruent solid geometry descriptions can represent complex geometries. Starting with a simple cylinder on the right, we can apply a subtraction of another smaller cylinder to produce a coaxial cylinder. We can then use a union to join another cylinder to the top to generate a semi coaxial detector shape.

Finally we pass the logical object to a physical volume class handling the actual placement of the volume. The physical volume represents the object in question, defining its boundaries, its position and any material properties. Any information needed, is passed through the physical volume, and given the correct offsets to be passed to each constituent simple solid.

Grid

A graphic of a cylinder represented on a course Cartesian grid is shown in Fig. 3.3. We can see the short comings inherent to this method. Even with very small grid spacing, there will be significant error near the surface which can collectively increase the error of the integral cells and final solution. Besides the inability to account for the volume and total charge, the greatest error comes from not being able to correctly enforce the boundary conditions of the electric field at the surface.

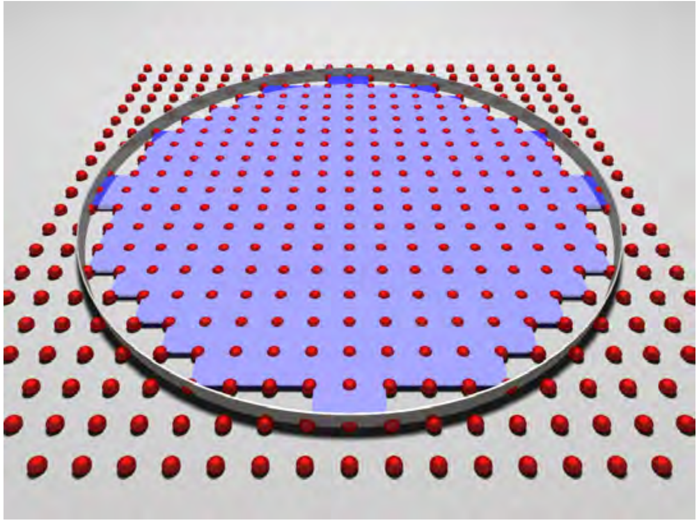

Figure 3.3: Illustration of how a cylinder super-imposed on a Cartesian grid. In red are the grid points of a regular Cartesian grid. With the cylinder superimposed the blue shows the volume of our effective solution.

CRT superimposes several grids. The basis is a Cartesian grid used to represent the potential at any point in the volume. A second non-regular grid represents the surface at any intersection of the surface with the Cartesian grid. This method faithfully reproduces the correct boundary conditions at the surface, most notably that the electric field is normal to the metallic surface [39].

CRT is written in the C++ language [49] making use of many of the key concepts. Defining base classes, inheritance, along with the extensive use of pointers. Each regular grid point contains the potential and charge at that point, as well as pointers to each of the six nearest neighbors and the distance to each. The CRT code uses relaxation to solve for the potential [39] and using pointers to get the nearest neighbor information relieves the code of costly overhead with the use of a little extra memory. The consequent speedup makes this simple relaxation implementation more than sufficient for calculating electric

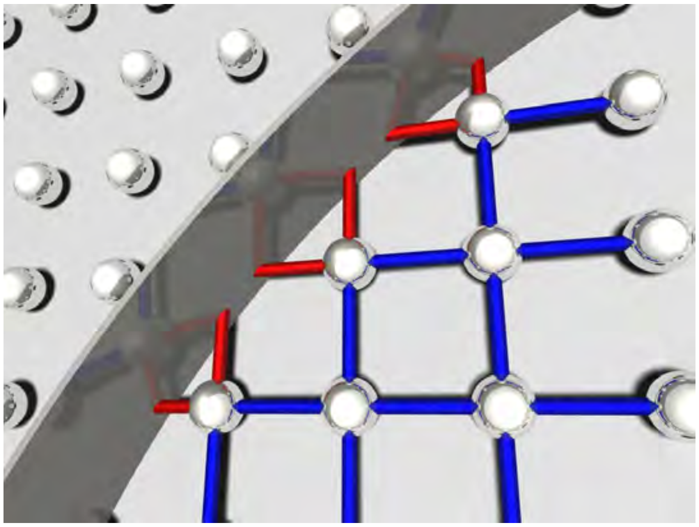

Figure 3.4: This figure demonstrates the relationship between each grid point and the superimposed surface grid point. The Blue connections are pointers from each grid point to its neighbor. The Red connections are pointers to the surface grid point potential. These links have the correct distance to the correct nearest neighbor. These surface elements can be understood as the superposition of two different grid systems. These two grids allow us the ease of a regular Cartesian grid while using the surface grid to correctly enforce boundary conditions. The ability to build the surface grid in any non-uniform way allows for the construction of complex geometries.

fields within the scope of this problem. These nearest neighbor pointers of the regular grid point to the necessary value at the surface for unambiguous calculation.

3.2.2 Charge Transport Dynamics

CRT can build directly or read from a file the weight potentials for each contact as well as the electrical potential given a charge impurity profile and applied voltage. From this CRT builds the electric field. For charge transport dynamics, a third order, 3D polynomial interpolation of the potential is built and stored for each grid point. This allows for a second order electric field such that the electric field and derivatives are smooth at any cell boundary. For dynamics,the interaction locations and deposition energies are read in from a file. The energies are mapped to charge in Germanium [6, 50] producing electron hole pairs.

This charge is propagated via a fourth-order Runga-Kutta **(RK4)**integration [51] of the charges from their initial positions to the boundaries. The velocity at each point is a function of the electric field and crystal lattice orientation given by [52, 4]:

$$v = \frac{\mu_0 E}{(1 + (\frac{E}{E_0})^{1/\beta})^{\beta}} - \mu_n E \tag{3.1}$$

Where the parameters come from the sign of the charge carrier and the crystal orientation relative to charge propagation.

Table 3.1: Coefficients for the velocity equation Eq. 3.1 from [4].

Velocity coefficients				
Orientation	μ_0	β	E_0 $[V/cm]$	μ_n
$< 100 >_e$	40180	0.72	493	589
$< 111 >_e$	42426	0.87	251	62
$< 100 >_h$	66333	0.7444	181	-
$< 111 >_h$	107270	0.580	100	-

The weighting potentials permit the calculation of all proper current and charge signals for even highly segmented detectors with complex geometry. CRT handles multiple depositions in a single event to produce a total signal. A record file is then produced of the current and charge signals. [50, 46, 53, 51, 54, 4, 48, 55, 52]

3.2.3 Pulse Processing

A separate code reads in the resulting current signal and convolves it with the transfer function of the readout electronics to produce the observed voltage signal. The voltage signal is stored in a binary file of the format used by the DGF4C digitizer from

X-ray Instrumentation Associates. This allows us to run the same analysis code on both the simulated and experimental signals for consistent comparison.

The transfer function captures the effect of a charge integrating preamplifier. The functional form of the response can be read in from a file that has been produced from a measurement or from a SPICE model [56]. The default behavior is to use a two parameter analytical model to approximate the electronics response. This analytical model works very well in general cases. Reading a response function in from a file allows one to fine tune the simulation to an electronics design or existing electronics package [57]. The analytical model is given as [58]:

$$R(t) = \frac{A}{T_d - T_r \frac{\sqrt{\pi}}{2\sqrt{1.3}}} \left(exp(-\frac{t}{T_d}) - exp(-\frac{1.3t^2}{T_r^2}) \right) \tag{3.2}$$

3.2.4 Verification and Validation

Validation of the electric field solution has been relatively straight forward. A comparison for geometries with analytical solutions has been performed 3.5. The electric fields are normal to the metallic surface in all cases tested. Explicit enforcement of this rule is not necessary with the super-position of the surface grid.

The energy histogram in Fig. 3.6 sums up the three main systematic tests necessary for this code. An input file was generated where an energy distribution was spread out along a constant radius but varying angle. The model has crystal lattice anisotropic drift velocity capabilities, however these results used an isotropic model where all charges moved at the same speed given the magnitude of the electric field. This tested the ability of the code to interpolate the electric field in 3D coordinates. The sensitivity of the current on the weighting field made this very difficult. Thus the systematic tests we felt were most significant for this code were:

- Charge conservation, charge is lost as a particle steps out of the volume, with such high fields the velocities must have good integration method. We use RK4 integration, charge is conserved in this model.
- Sufficiently smooth interpolation methods, the current is very sensitive to the weighting field, so we must have a good interpolation method, otherwise the results are both non-conservation of charge and inaccurate signals.
- Correctly account for non-Cartesian system in Cartesian coordinates. Interpolating along an axis on a grid is fairly easy, interpolating in a 3D grid, is straight forward as long as the point is sufficiently contained by Cartesian grid point. If we are near a surface, most interpolation schemes introduce errors. Correct geometric accounting ensures that every path gives the correct pulse for the same energy for the same radius.

3.3 Charge Impurity Profile

The signal is a function of the velocity. The velocity and path depend on the electric field in the detector. The electric field is a direct result of the boundary conditions combined with the charged density of the charged impurities, both acceptors N_A and donors N_D. The total charge density is the difference in these two impurities per unit volume.

The charge density is one of the most critical parameters in the computational model. Ironically, the charge density, from the dopant's, is the most difficult parameter to measure and insufficiently understood. The underlying processes are understood, the

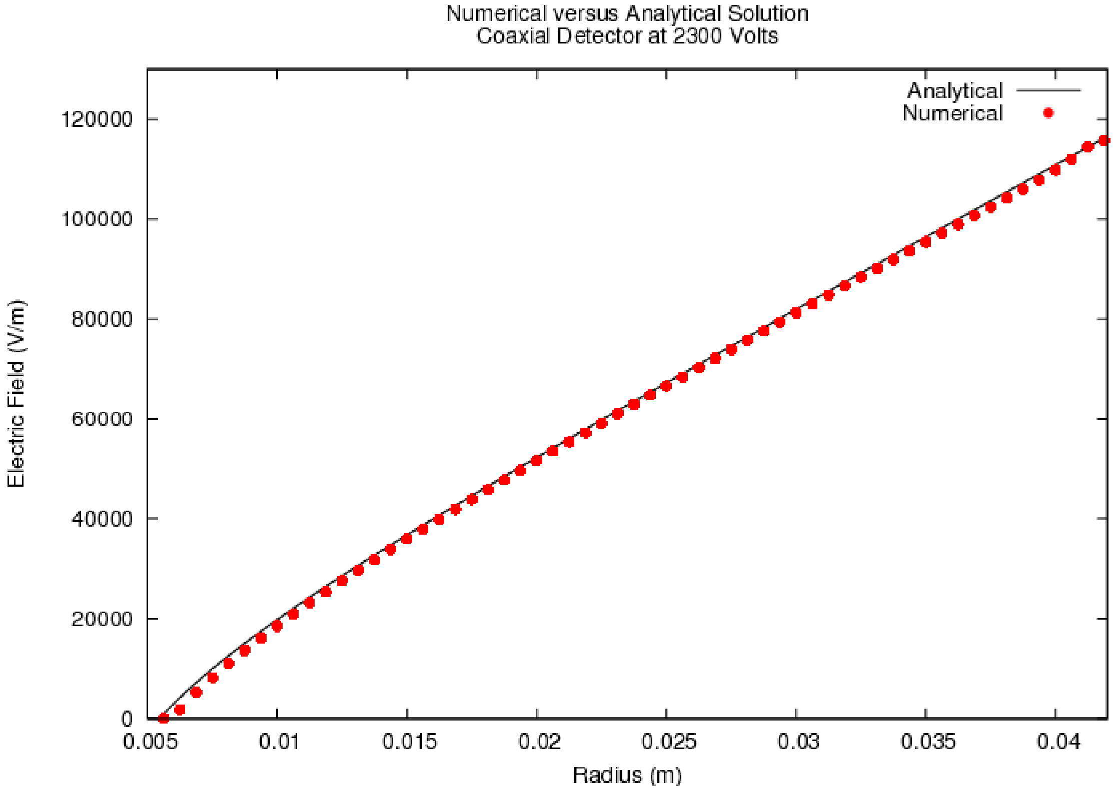

Figure 3.5: The potential of a true cylindrical coaxial HPGe from simulation compared to the analytical solution [6].

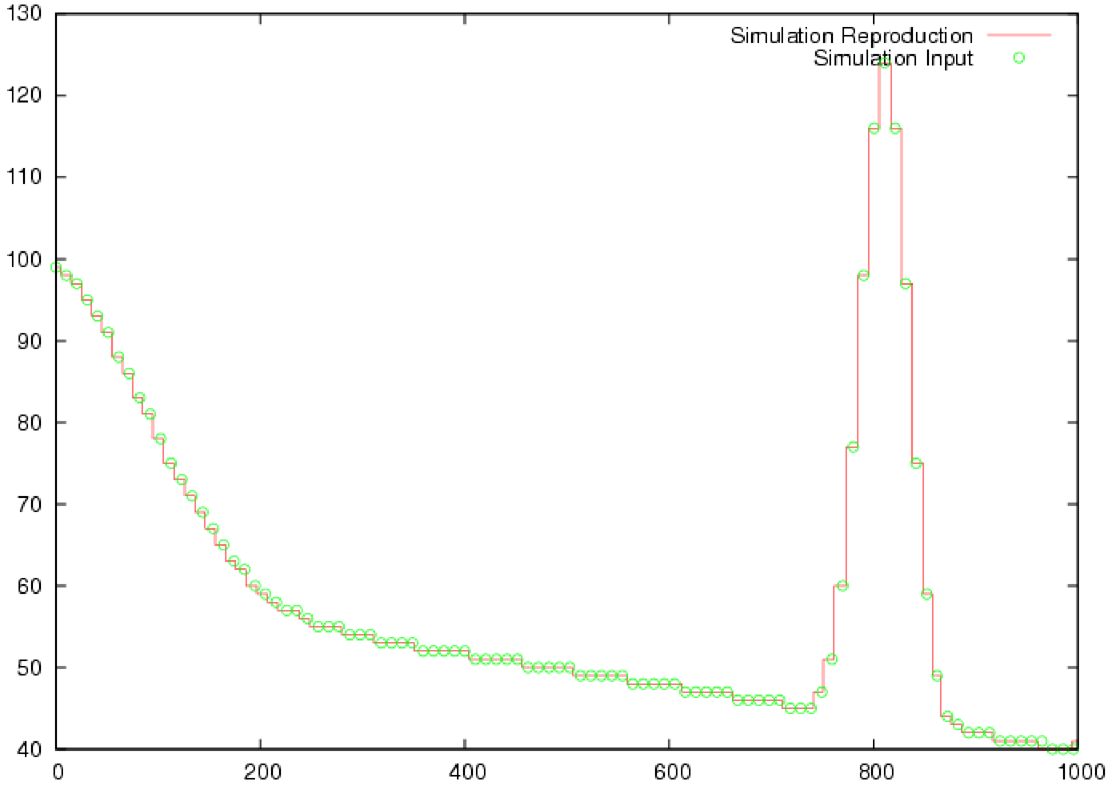

Figure 3.6: Comparison between simulated energy depositions uniformly distributed through an HPGe detector and the energy given after charge transport simulation. This type of systematic test shows that the energy is preserved across the crystal volume. This type of test also shows that charge is conserved as well.

models exist, but few studies have been preformed to examine the nature of charge density profiles in working high purity germanium detectors. A method to quickly obtain a charge density profile is given in chapter 6.

The lack of these studies is a critical shortcoming in the current status of detector characterization methods. A proper handle on the charged impurity profile is necessary for any functional model of the detector response [7]. The impurity profile determines many physical aspects of an HPGe detector performance, including the depletion voltage, the capacitance, and the pulse shape characteristics directly. How to find the charged impurity profile is given in chapter 6, along with a comparison to other methods.

Chapter 4

Single from Multiple Site Rejection

The signatures of events encountered in double beta decay experiments can be classified according to the the spatial distribution of ionization in the semiconducting detector. A detailed classification for these events is given in addition to the importance of multiple site rejection and single site acceptance. A simple analytical model of the pulse shape discrimination is presented as well.

4.1 Why we need it

The $0\nu bb$-decay process has, in addition to the daughter nuclei, two electrons and no neutrinos in the final state. The sum of the kinetic energies of the electrons is therefore approximately equal to the Q-value for the decay. For the germanium isotope ^{76}Ge this energy release is $Q_{\beta\beta} = 2039$ keV [59]. Electrons in the relevant energy range predominantly deposit their energy in germanium via ionization. The range of the electrons is of the order of millimeters [60]. Since the germanium detectors under consideration has a volume of the order of $400cm^3$, the energy of the electrons will be fully contained within a small volume of the crystal, if no hard bremsstrahlung is present. The signature of $0\nu bb$-decay events is thus a peak at the energy of 2039 keV.

Background events are produced from a wide variety of physical processes with alpha's, beta's, gamma's, pion's, muon's, neutrons, etc..., in this work we concentrate on the dominant background contributions in underground low background germanium experiments resulting from gamma radiation. Background rocesses not treated here are considered more fully elsewhere [61] as is the overall neutron flux from radioactive elements in the surrounding bed-rock.

All radioactive materials with Q-values larger than $Q_{\beta\beta}$ are potential background sources for the $0\nu\beta\beta$-decay process. A fraction of the released energy can be deposited inside a detector, such that the measured energy is in the region of interest **(ROI)** the $Q_{\beta\beta}$-value. Photons in the MeV range predominantly deposit their energy via Compton scattering. Their absorption length is of the order of centimeters. Considering the size of the germanium crystals under study, process with photons in the final state are likely to deposit only a fraction of the total energy inside one detector. The signature of the $0\nu\beta\beta$ decay signal and the main background signatures are classified according to the particles in the final state[1].

- *Single Site*:
  - *Two electrons*: This class encompasses the neutrino-less and neutrino accompanied double beta decay processes. If the energy resolution is better than 10keV, the two modes of double beta decay can be separated, since the energy region around the $Q_{\beta\beta}$-value is not populated by $2\nu\beta\beta$-decay process. The two electrons deposit their energy locally, i.e. on a millimeter scale, see Fig.4.1.

---

[1] The Single Site versus Multiple Site categorization was adapted from Abt[62], indicating wether energy deposition occurs entirely within a single detector region or if energy deposition is divided amoung several detector regions.

- *Multiple Site*:
  - *Photon(s) and electron*: This class contains all β^- decay processes accompanied by the emission of one of more photons which occur inside the detector or close to its surface. The energy of the electron is deposited locally, whereas the photon scatter and not all of its energy is necessarily deposited inside the detector. An example for this class is the decay of ^{60}Co inside the germanium.
  - *Photon(s) and positron*: Similar to above, this class contains all β^+-decay processes accompanied by the emission of one or more photons inside the detector. The positron deposits most of its energy locally and annihilates. The photons (the two 511 keV gammas plus any additional photons) scatter and mostly do not deposit all of their energy inside one detector. The most prominent example for this class is the decay of ^{68}Ge inside the germanium.
  - *Photon(s) only*: If the decay occurs outside the germanium detectors, α-particles of electrons can be stopped before they reach the crystals. Most prominent examples are the decays of ^{208}Tl and ^{214}Bi which come from radio-impurities in the detector surrounding.
  - *α-particles*: Surface contaminations with ^{210}Pb or other isotopes which decay via α-emission can contribute to the background. α-particles in the 2-10 MeV range deposit their energy on a 2-50 μm scale. α-particles emitted at the surface therefore potentially deposit only a fraction of their initial energy inside the active volume of the crystal.

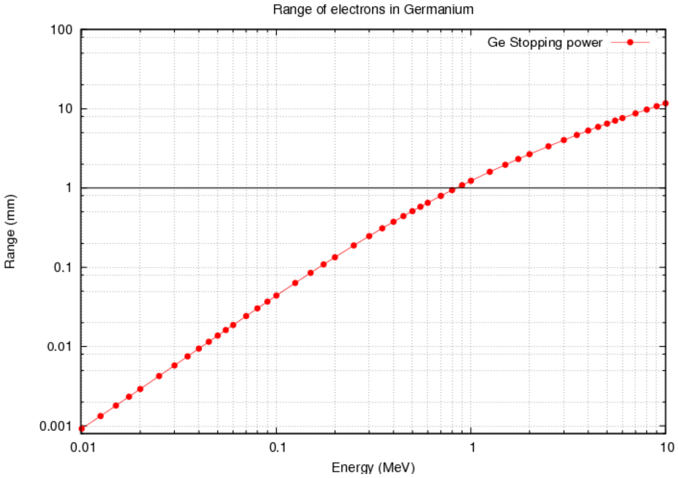

Figure 4.1: The electron range in HPGe versus initial energy. The solid horizontal line shows the 1 mm electron path length close to 0.9 MeV.

4.2 Statistical Moments

In this section we discuss the use of a pulse shape discrimination method derived from statistical moments but not normalized to a normal distribution. The properties of this parameter space provide an excellent basis for a complete framework to describe pulse properties.

> In order to arrive at a distinct formulation of statistical problems, it is necessary to define the task which the statistician set himself: briefly and in its most concrete form, the object of statistical methods is the reduction of data. A quantity of data, which usually by its mere bulk is incapable of entering the mind, is to be replaced by relatively few quantities which shall adequately represent the whole, or which, in other words, shall contain as much as possible, ideally the whole, of the relevant information contained in the original data. [63]

4.2.1 Statistical Moments properties

In the statistical description of any distribution of data point we use the statistical language of moments. When a set of values has a sufficiently strong central tendency, that is, a tendency to cluster around some particular value, then it may be useful to characterize the set by its moments. A moment in this sense derives its meaning from physics and is given mathematically by the nth moment of a real-valued function $f(x)$ of a real variable about a value c is

$$\mu_n = \int_{-\infty}^{\infty} (x-c)^n f(x) dx \tag{4.1}$$

The real value c is the mean of the function at the origin. Given the subtle assumption that all moments are about the origin leading to the subtlety $c \to \mu$.

The zeroth moment ($n = 0$) gives the **area** under the curve.

$$\mu_0 = \int_{-\infty}^{\infty} (x-c)^0 f(x) dx = \int_{-\infty}^{\infty} f(x) dx \tag{4.2}$$

In the context of signal filters, this moment is preserved for most filters including a moving window average. Few filters guarantee the preservation of higher moments. For discrete signals this takes the form:

$$\mu_0 = area = \sum_{j=0}^{N-1} x_j \tag{4.3}$$

The next moment for $n = 1$ is the **mean** of the function and is given by:

$$\mu_1 = \int_{-\infty}^{\infty} (x-\mu)^1 f(x)dx = \int_{-\infty}^{\infty} (x-\mu) f(x)dx \tag{4.4}$$

where μ is the mean. This may be confusing to have the mean defined in terms of itself, but this is because this gives us the translated mean about the origin. If we assume that the mean is already at the origin, then $c = 0$ in what follows. For discrete signals we have the form:

$$\mu_1 = mean = \frac{1}{N} \sum_{j=0}^{N-1} x_j \tag{4.5}$$

The second moment, $n = 2$, is the **variance** of the function given by:

$$\mu_2 = \int_{-\infty}^{\infty} (x-\mu)^2 f(x)dx \tag{4.6}$$

For discrete signals we have the form:

$$\mu_2 = variance = \frac{1}{N-1} \sum_{j=0}^{N-1} (x_j - \bar{x})^2 \tag{4.7}$$

We note that σ is defined as $\sigma = \sqrt{variance}$.

The third moment, $n = 3$, is the **skewness** of the distribution. The skewness of a function is a measure of its lopsidedness. A symmetric distribution will have a skewness of zero. The skewness is given in the usual way:

$$\mu_3 = \int_{-\infty}^{\infty} (x-\mu)^3 f(x)dx \tag{4.8}$$

Again, for discrete signals this has the form:

$$\mu_3 = skewness = \frac{1}{N}\sum_{j=0}^{N-1}\left\{\frac{x_j - \bar{x}}{\sigma}\right\}^3 \tag{4.9}$$

A distribution that is skewed to the left has a negative skewness and one to the right has a positive skewness.

The fourth moment, $n = 4$, is the **Kurtosis** of the distribution. The kurtosis measures if a given distribution has a peak or a flat shape to it.

$$\mu_4 = \int_{-\infty}^{\infty}(x-\mu)^4 f(x)dx \tag{4.10}$$

Again, for discrete signals this has the form:

$$\mu_4 = kurtosis = \left\{\frac{1}{N}\sum_{j=0}^{N-1}\left\{\frac{x_j - \bar{x}}{\sigma}\right\}^4\right\} - 3 \tag{4.11}$$

We will note that the value 3 subtracted from the end make the value zero for a normal distribution.

These moments are important to the application of filters to noisy data. Few filters preserve moments higher than $n = 0$. One exception is the Savitsky-Golay filter **(SG)** [51]. This is a filter in the time-domain as opposed to the frequency domain. SG preserves up to a designated n^{th} moment. Each physical characteristic of a pulse is related to one of these moments, and if we want to be able to discern signal from noise we must preserve the necessary moment. SG can remove noise in a very simple way in the time domain while retaining a designated nth moment of the information. Thus SG is very important to pulse shape analysis applications.

Another important statistical quantity to the field of radiation detection is the Fano factor. The Fano factor relies on moments one and two, $n = 1$ & $n = 2$. The Fano factor is defined as the ratio of the variance to the mean:

$$F = \frac{\sigma^2}{\mu} \tag{4.12}$$

This is a measure of the dispersion of a probability distribution. It was formulated to explain integrated charge of a specific energy in radiation detectors had a spread due not only to the electronic noise but also due to the detector material properties [40].

4.3 Pulse Shape Discrimination

4.3.1 Introduction

Pulse Shape Discrimination **(PSD)** is the process of extracting information from each pulse produced by radiation interaction with a detector. Pulses often go through several stages of amplification. As the signals travel through the detector and associated electronics noise accumulates in the signal. This noise must be minimized in order to extract the maximum amount of information from a pulse [50, 64].

Assuming reasonable minimal noise, there exists a great deal of information that can be extracted from pulse shapes. Current off-the-shelf systems use the pulse to determine the energy deposited from an interaction. However, particle identification, geometric information, and even particle paths can be extracted from these pulses [9, 57].

The PSD technique used to distinguish multi-site events from single-site events in the IGEX experiment is based on 3 moments of the current pulse. Unlike the statistical moments of the previous sections, these moments were designed to maximize the ability to discriminate specific information from current pulses of characteristic shape [9]. The first parameter is the pulse rise time, the second is the full width from the half width, the third is a normalized moment about the center of mass.

4.3.2 Aalseth PSD Method

The discrimination technique explored here is the method developed by Aalseth et.al.[9, 65], using three energy independent parameters to discriminate multiple site events from single site events. This method takes a raw current pulse from a digitizer, and applies any of several Digital Signal Processing **(DSP)** techniques. The only necessary DSP

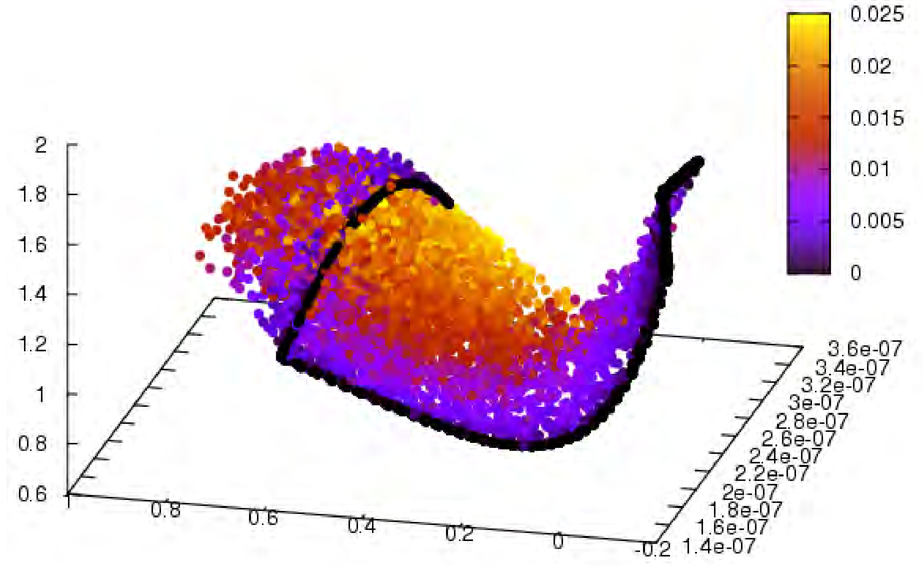

Figure 4.2: Theoretical PSD parameter space with color indicating the distance between multiple interactions.

techniques is smoothing, which is done with the Savitsky-Golay filter [51]. This filter was discussed previously.

The first parameter is the timing information. Given a voltage signal, the most obvious timing is the rise time (τ) of the voltage pulse, often taken as the time it takes to go between 10% and 90% of the maximum height of the voltage pulse. The 10% to 90% is often called the constant fraction discriminator **(CFD)** and it used to truncate noise from the measurement. Techniques to measure the rise time of a voltage pulse are given by the IEEE [66].

The rise time can come from the CFD of the voltage pulse, however in this method all of the parameters come form the current pulse. The current pulse, $I(t)$, comes from discrete differentiation of the voltage pulse. The rise from from the CFD applied to the

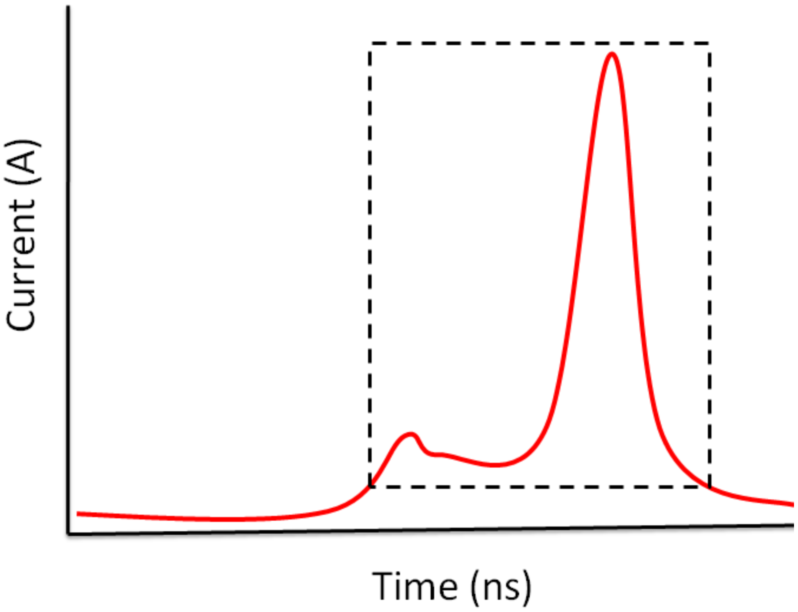

Figure 4.3: A current pulse with the 10% to 10% of the maximum enclosed in a box. The timming points needed are the start time, the end time and the time directly in the middle of these two, called the mid time.

current pulse begins at the 10% level to the left of the maximum and goes until it reaches the 10% level to the right of the maximum. Fig. 4.3 shows a typical current pulse with a box encompassing the timing information.

The second parameter used is the front back half back area **(FHBH)**. If we start at the center of the current rise time, and integrate the area before this we have the front area. If the we integrate the area after this, we have the half back area. This is illustrated in Fig. 4.4.

$$FrontHalf = B = \int_{\tau_i}^{\tau_{1/2}} I(t)dt \tag{4.13}$$

$$BackHalf = C = \int_{\tau_{1/2}}^{\tau_f} I(t)dt \tag{4.14}$$

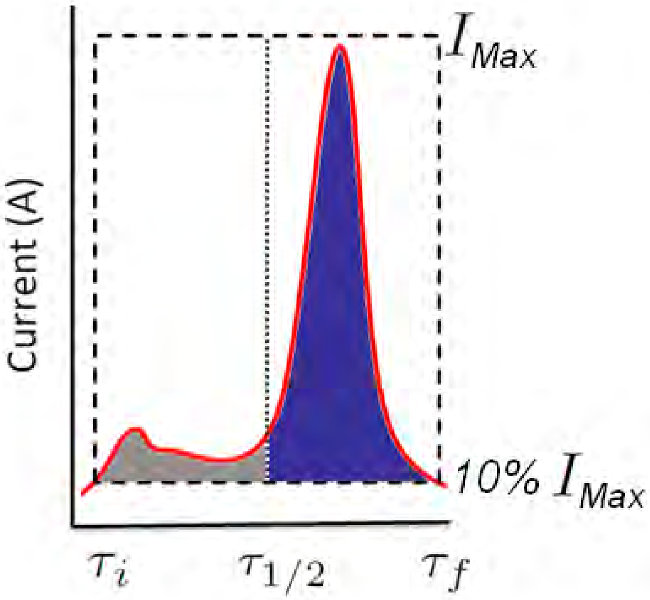

Figure 4.4: The front back area and the half back area as measured from a current pulse.

Then we define this parameter as:

$$\frac{B-C}{B+C} \tag{4.15}$$

The third parameter is the normalized moment **(I)**, similar to the moment of inertia in mechanics. If we take the moment of inertia for a plane in x and y, with the axis at $x = 0$ and rise time τ, parallel to the y-axis we have a moment given by:

$$I = \frac{m\tau^2}{2} = \int_{-\tau/2}^{\tau/2} mx^2 dx \tag{4.16}$$

Then we can find the moment of the front half via:

$$I_B = \int_{\tau_i}^{\tau_{1/2}} I(t)(t-\tau_{1/2})^2 dt \tag{4.17}$$

and the back half is given by:

$$I_C = \int_{\tau_{1/2}}^{\tau_f} I(t)(\tau_{1/2} - t)^2 dt \tag{4.18}$$

Then the normalized moment is given by:

$$I_N = \frac{I_B - I_C}{I} \tag{4.19}$$

The first note about these parameters is that the interaction location is lost. This is to say that these parameters are degenerate to the azimuthal angle and height of a cylindrically symmetric detector, so we cannot extract from a current pulse. This, however, is not a weakness because for experiments such as Majorana there is a much more important piece of information that can be extracted. We can extract whether an event was single site or multi site.

A single site event is exactly that, a photon interacts with an electron in a restricted, contiguous region of space. If a photon is completely absorbed by an electron, or in a detector a photon Compton scatters only once and then escapes the crystal, single site events are produced. Ultimately, we are limited by the spatial resolution of our PSD techniques, and cannot resolve events as single or multiple site if they occur too together. Hence, a photon which Compton scatters several time in a very small volume of the detector may be classified as single site by our PSD technique, even though, from a physics perspective events occur at several distinct regions. From a functional perspective any event which can be identified as multiple site cannot be double beta decay [23], so ultimately, our spatial resolution limits our ability to cut background events from a double beta decay experiment.

The Aalseth PSD method is excellent at discriminating if a current pulse was in fact due to one ionization event or several within the time of the pulse duration. This technique is often called a radial discriminator because it is assumed that two events, happening at the same time at the same radius, will look like a single event because it will take them the same mount of time to get to the collecting electrode. Thus, the current pulse will look like a single event.

4.3.3 Analytical Model for PSD

We can write a simple model for a current pulse given an interaction radius if we deal only with a coaxial detector. Second, if we assume that all charge carriers travel at saturation velocity at all times. These assumptions are not very restrictive and produce a surprisingly good model of the current pulse coming from the detector. We can write this model as

$$I(r_0, v_c, t) = Q \frac{1}{ln(R_i/R_o)} v_c \frac{1}{r_0 + v_c t} \tag{4.20}$$

where r_0 is the energy deposition radius, v_c is the saturation velocity for a given charge carrier, since the distinction of electron or hole can make a significant difference. Given the constant velocity, we can easily solve for the time it takes to reach the corresponding electrode with

$$\tau_e = \frac{R_o - r_0}{v_e} \tag{4.21}$$

$$\tau_h = \frac{r_0 - R_i}{v_h} \tag{4.22}$$

A function can be used with a Heaviside step function to account for the finite path while integrating over all time. However with careful consideration of individual integration limits, the Heaviside step functions are not necessary.

The first parameter is simply the maximum of the two charge carrier collection times, which is the rise time as it would be measured. If the electron transport time is longer than that of the hole, we use it, or vice versa. For multiple site events, we simply use the longest transport time. The longest transport time, for any event whether single or multiple site, is τ.

The second parameter space is the front half back half **(FHBH)** area, given by the integral of the front half and the back half of the current:

$$B = \int_0^{\tau/2} I(r_0, t)dt = \int_0^{\tau/2} (I_e(r_0, t) + I_h(r_0, t))dt \tag{4.23}$$

So,

$$B = \int_0^{\tau/2} (\frac{QDv_e}{-r_0 + v_e t} + \frac{QDv_h}{r_0 + v_h t})dt \tag{4.24}$$

with $D = 1/ln(R_i/R_o)$. It must be pointed out that the integration to $\tau/2$ could be greater than the transport time for that charge carrier $\tau_c/2$. So care must be taken with this integration limit.

We need the other side of this integral which is given as C:

$$C = \int_{\tau/2}^{\tau} (\frac{QDv_e}{-r_0 + v_e t} + \frac{QDv_h}{r_0 + v_h t})dt \tag{4.25}$$

We have the FHBH parameter $B - C$ given by the integral equation:

$$B - C = \int_0^{\tau/2} (\frac{QDv_e}{-r_0 + v_e t} + \frac{QDv_h}{r_0 + v_h t})dt - \int_{\tau/2}^{\tau} (\frac{QDv_e}{-r_0 + v_e t} + \frac{QDv_h}{r_0 + v_h t})dt \tag{4.26}$$

Thus, given τ we can easily integrate to find the FHBH parameter in this model.

4.3.4 Velocity and the PSD parameter space

The focus of this analytical parameter space model is to show that by including anisotropic drift velocities in our models, we can improve our ability to get at the relevant information in these experiments. If the Aalseth PSD method is to be improved on, then

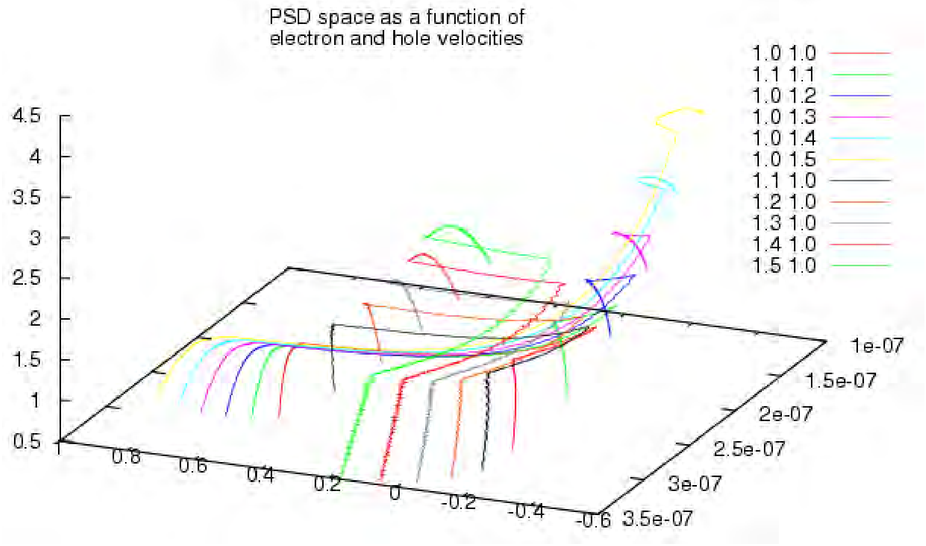

Figure 4.5: The PSD line for single site events as the interaction point moves along the radius. The different lines indicate the effect of different combinations of drift velocities for electrons and hole respectively.

there must be an affect on the PSD parameter that can be discerned. One parameter to explore is the effects of different electron(v_e) and hole (v_h) drift velocities. Such an effect is illustrated in Fig.4.5.

From Fig.4.5, we can see that velocity of the charge carrier not only affects the signal site curve through PSD space, but the velocity of each charge carrier affects this curve differently. This can be translated into the statement that the single site curve through PSD space contains information about the velocity of the charge carriers. The question that remains is the nature of noise in the PSD space and if the differences due to velocity are significant enough to be extracted from this noise.

4.3.5 Notes on PSD

We had to discern if an anisotropic drift velocity will affect the PSD results. We have established that it will. Next we must show significance in that some of this information can be extrapolated out of the noise inherent in the signal. So we asked how the noise in the current pulse affected the PSD data.

For the pulse time information, the current pulse is a set of discrete data points in time. If there is jitter (error in the timing of the data point) it cannot be distinguished from an error in the current pulse. This is due to the fact that the current is in fact a continuous signal and displacement from noise in the time direction is the same as a displacement current value. Error in the timing is the same as error in the current, so we will refer to a single error and assume it is simply of the current.

For the discrete current data points any error will effect the pulse width parameter space by inducing an expansion or contraction in the space. This effect is linear with the error and to be expected. This is not magnified in any way, neither is different in part of the space as it is from another. In fact this error is greatly reduced by using a Savitsky-Golay filter [51].

The error introduced to the FHBH area parameter space is different from that of the rise time. If we assume the error is additive to the current (as opposed to multiplicative) we can use the toy model above to ascertain its effect in this parameter space.

$$B'-C' = \int_0^{\tau/2}(I(t)+e(t))dt - \int_{\tau/2}^{\tau}(I(t)+e(t))dt = B+E_B-(C+E_C) = (B-C)+(E_B-E_C) \tag{4.27}$$

The denominator gives us:

$$B'+C' = \int_0^{\tau/2}(I(t)+e(t))dt+\int_{\tau/2}^{\tau}(I(t)+e(t))dt = B+E_B+(C+E_C) = (B+C)+(E_B+E_C) \tag{4.28}$$

The resulting equation with error is:

$$\frac{B'-C'}{B'+C'} = \frac{(B-C)+(E_B-E_C)}{B+C+E_B+E_C} \tag{4.29}$$

Given that the error E_C is approximately the same size as E_B the contribution to the numerator is very small, but the contribution to the denominator will push this parameter toward the origin. Given that the error at any given point can be greater than or less than the current at that point, but it cannot be negative due to the choice of baseline, given that it is part of the pulse and well removed from negative values. The sum of the error cannot be negative given the CFD level is much greater than the error as a requirement of a good CFD [66], any error will push this parameter toward the origin. The range of this parameter is both positive and negative due entirely to the numerator. Thus adding error to the denominator will contract this parameter range toward the center.

The error contribution to the normalized moment is very different from the other two parameters. If the error is once again additive, then it can be separated from the current in the integral like so:

$$M' = \int_0^{\tau}(t-\frac{\tau}{2})^2(I(t)+e(t))dt = \int_0^{\tau}(t-\frac{\tau}{2})^2 I(t)dt + \int_0^{\tau}(t-\frac{\tau}{2})^2 e(t)dt = M+E \tag{4.30}$$

while the denominator gives:

$$\left(\int_0^{\tau}(I(t)+e(t))dt\right)\frac{\tau^2}{12} = \frac{\tau^2}{12}(B+C+E) \tag{4.31}$$

Thus the error in the denominator will contribute in a linear fashion, meaning here uniform everywhere in the PSD space. The numerator, however, multiplies the error by its distance from the mid-point squared. This is a very non-linear contribution not only in time but also in the parameter space. One conclusion is that error will have the greatest affect for the longest pulses. Given the error term in the denominator is linear while that in the numerator is multiplied by a square term, the error will push the normalized moment away from the origin, and in a non-linear fashion. The error in the normalized moment maybe by far the most significant in the PSD parameter space.

The ultimate result of errors introduced into this PSD method are a contraction of data in each dimension. Error in the timing information is referred to as timing jitter whose effects are nominal compared to the other two dimensions. The FHBH and Moment dimensions contract with the introduction of error, or noise, to the signal. The effect is linear, but given the discrete nature of the PSD algorithm a contraction of the space will make discrimination more difficult. The acceptable levels of error for any signal of interest can be evaluated with this simple analytical model. In order to asses the impact of this method, however, we must introducea figure or merit capable of directly comparing alternate methods.

4.4 Figure of Merit

A figure of merit,**(FOM)**, is in general some quantity used to characterize the efficacy of a method relative to alternative methods. The FOM commonly used in neutrinoless double beta decay experiments, and used through out this work, is defined by Aalseth *et. al.* [67] with the form

$$FOM = \frac{\epsilon_{\beta\beta}}{\sqrt{\epsilon_{background}}} \tag{4.32}$$

where $\epsilon_{\beta\beta}$ and $\epsilon_{background}$ are the acceptance fractions of the discrimination for $0\nu\beta\beta$ decay events and background events, respectively. The usefulness of this FOM definition is that it is a multiplier to the standard half-life limit. This gives the direct improvement that one might gain in half-life sensitivity of the experiment due to the method of discrimination. Thus any analysis method can be compared by the FOM that it produces to any other analysis method.

Chapter 5

A P-type Modified Electrode Detector: Overview of Detector Properties

5.1 Introduction

An n-type germanium crystal with a small with a small point contact was reported by Luke [68] in 1989. Barbeau *et al.* [8] recently presented, for the first time, the implementation of this geometry as a p-type point contact (PPC) detector. Having a 330 eV energy threshold and energy resolution of 1.8 keV at 1332 keV, the performance of this detector has generated interest in the nuclear science community working on ultra-low background radiation measurements. At the time of the Barbeau *et al.* [8] paper , only one such PPC detector had been extensively studied, thus the question arises regarding the future availability and potential production rate of this detector design. This chapter presents an overview of the influence of the impurity concentration[1] and the impurity profile of the germanium crystal on the performance of an operational PPC detector. We present the results

---

[1] Throughout this paper the term “impurity concentration” is used as short hand for “net electrically-active impurity concentration”. Similarly, the term “impurity profile” is short hand for “net electrically-active impurity concentration spatial profile”.

of field modeling and charge transport simulations of PPC detectors. We use consistency with the depletion voltage, the charge transport time and the depletion capacitance curve of the existing PPC detector to establish the reliability of our models. The results of our simulations and comparison to known germanium ingot characteristics suggests that the PPC design is a feasible detector for regular manufacture, not unlike typical p-type coaxial detectors.

5.2 Motivation for the P-type Detector Geometry

There are two consequences to the electrode configuration of a PPC detector, as shown on the right in Fig. 5.1[8]. The first consequence is a reduction of the detector capacitance to $\sim$ 1 pF in comparison to $\sim$ 40 pF for a typical semi-coaxial detector [6]. The reduced capacitance permits a lower energy threshold [50], and an improved ability to resolve spatially separated charge depositions through pulse shape analysis (PSA). Barbeau *et al.* [8] have already reported one potential application of this detector design – the measurement of neutrino-nucleus coherent scattering. Another important application, the use of HPGe detectors in searches for neutrino-less double beta decay [23], provides a stringent set of performance requirements. Those requirements include excellent energy resolution (better than 0.2% FHWM at 2MeV), high mass detector elements($\geq\sim$ 0.5 kg), amenable to implementation in an ultra-low radioactive background environment and the ability to distinguish events of interest from background events.

The predominant event identification method is based on neutrino-less double beta decay producing a single-site energy deposition while gamma-ray backgrounds often produce multiple site energy depositions [9]. Although several commercially available germanium

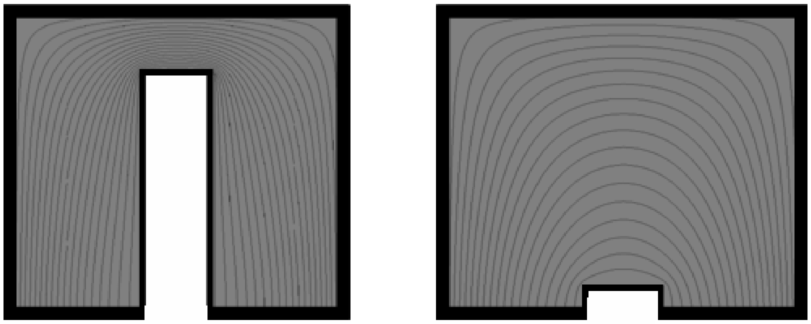

Figure 5.1: This notional diagram shows the comparison of an ordinary p-type detector (left) and a p-type point contact detector (right) showing a dead layer (dark), bulk p-type material (light), and an implanted contact on the central hole (thinned).

detector designs satisfy the energy resolution and mass requirements, there is typically a trade off between event identification capability and the requirement to minimize the introduction of radioactive contaminants in the electrical instrumentation and cabling components needed for readout. Typical p-type coaxial HPGe detectors allow the greatest control over radioactive backgrounds in detector construction materials; having only two contact electrodes, there are a minimal number of readout components. However, the event identification in typical p-type coaxial detectors is limited to PSA sensitive only to energy depositions spatially separated in radial position [69]. An alternative is to use highly segmented detectors which provide segment position, PSA-based radial position, and vertical and phi-cylindrical coordinate through PSA of adjacent segments **citation**. The price paid for this 3-dimensional event localization is the number and complexity of the read-out electronics (and their potential contaminants) required for the segmentation. In the absence of a clearly superior choice of detector design, investigation into alternative designs, such as the PPC detector, is warranted.

The central point-contact PSA for a PPC detector is substantially more powerful in differentiating single vs. multiple site energy depositions than obtainable from standard coaxial p-type detectors. This results from the stretching out of the charge collection signal in time due to decreased weight fields and increased charge transport path lengths relative to a standard p-type design. In contrast to segmented detectors, this improved event discrimination ability does not increase the number or mass of cabling and local electronics components, relative to the coaxial p-type. Likewise the PPC design does not increase the complexity of the read-out instrumentation and subsequent analysis as will a fully instrumented segmented detector [70, 71]. In the specific case of neutrino-less double beta decay experiments, the PPC design profits from the thick (≈ 0.5 mm) dead layer covering most of the crystal surface, which acts as a shield against external betas, x-rays, and surface alpha particles. Hence the PPC detector design is compatible with good ultra-low background design while improving upon the event discrimination capabilities of coaxial p-type detectors.

For a successful future neutrino-less double beta decay or dark matter program, the benefits of the PPC detector design may be desirable, but cost, difficulty in manufacturing, and the rate of production are important considerations, especially in light of the number of detector elements required for a future large-scale experiment. For these reasons it is important this new detector design be straightforward and cost effective to manufacture. For comparison, the cost of a generic p-type detector of 1 kg mass is approximately 1/3 the cost per kg of a highly segmented n-type detector. If the cost and difficulty of manufacturing a PPC detector is only incrementally higher than a common, p-type coaxial detector of similar mass, broader applications are possible and essentially every detector manufacturer will be able to produce them. The goal of this chapter is to investigate the likelihood of

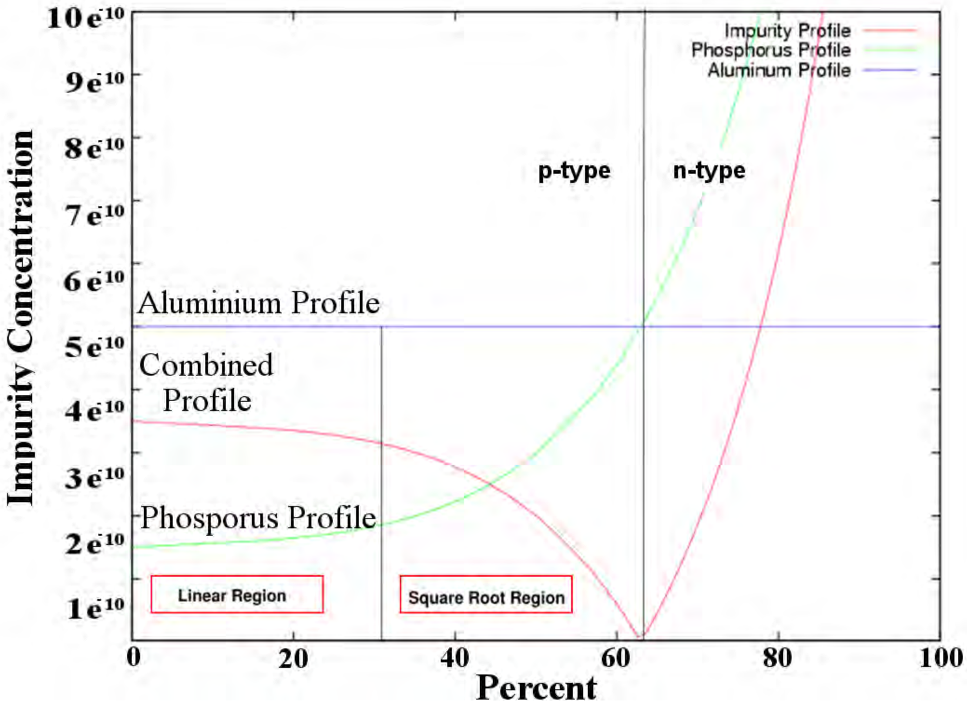

Figure 5.2: Impurity profile of a germanium ingot [7]. The crystal growth seed is located at the 0 percent end of the crystal.

this outcome.

The driving factor for determining the type (p- or n-type) and the quality of the detector is the distribution (amount and profile) of impurities throughout the ingot. Fig. 2.5, reproduced here as Fig. 5.2, shows the typical impurity concentration and profile of a germanium ingot. The impurity profile arises in the production of germanium crystals due to the different segregation coefficients of the electrically-active trace impurities in the Czochralski crystal pull method [7]. The analysis presented in this paper suggests that a reasonably wide range of impurity profiles will lead to an acceptable p-type point contact detector. To facilitate comparison, the same dimensions given in [8] for the first PPC detector were used for this study (2.5 cm radius and 4.4 cm length).

5.3 Method

A study of the impact of the impurity profile on the acceptability of a PPC detector requires defining “acceptable performance”. The limits due to practical considerations are: reasonable maximum applied depletion voltage and a maximum charge collection time. These requirements together bound the usable parameter space of the model used for these calculations. We use a model to pair impurity profile and the charge transport properties of the detector to identify acceptable impurity profiles. Our impurity profiles can be somewhat arbitrary, therefore we use consistency with the measured depletion voltage, charge transport time and the depletion capacitance curve of the existing PPC detector to establish the reliability of our models. The calculation method uses a simulation of charge transport through a germanium crystal in the presence of the appropriate electric field. Two such codes have been developed at PNNL, an earlier 2-D model [57] and more recently a 3-D version [72]. The earlier code was validated in the IGEX experiment [73] while the new 3-D code has been shown to reproduce the 2-D solutions. The dynamics are handled with the application of the Shockley-Ramo theorem[2] [47, 46, 48, **?**] and a parametric description of charge carrier mobility [4].

In this study, the equation describing the impurity concentration of a crystal cut from the p-type region of the ingot is given as a function of the crystal height alone [7]. The impurity density is given as:

$$\rho(z) = A + B\sqrt{\frac{z}{H}} \tag{5.1}$$

where A is the crystal’s minimum impurity concentration and B is the coefficient describing the shape of the impurity profile. Both A and B have units of net electrically-active impurity

---

[2] See Appendix A. for a derivation of the Shockely-Ramo theorem

concentration (i.e., $atoms/cm^3$) with the radial dimension accounted for. The constant H is the detector's height. The independent parameter, z, is the distance between [0,H]. Using a two parameter equation simplifies the description of the net charge impurity concentration distribution, such that only the boundary values at either end ($\rho(z = 0) = A$ and $\rho(z = H) = A+B$) are necessary. This is equivalent to the parameterization used for the detectors of the GRETINA experiment [71] and is implicit in the discussions of Haller *et al.* [7]. As the difference between the impurity concentrations at either end of the crystal decreases, the profile becomes more linear. As the difference increases, the profile has more curvature due to the square root dependence on z, as in Fig. 5.2.

Using the simulation, the voltage necessary for depletion is determined for the (A,B) parameter space, this calculation is described in section 6.3. This parameter space is bounded by a maximum allowable depletion voltage at 5 keV, consistent with typical instrumentation, preamplifier high voltage filters, and achievable crystal surface dielectric strength. The acceptable parameter space is compared with that for an equivalent p-type coaxial detector in Fig. 5.4. In this context, an equivalent p-type coaxial detector has the same external dimensions as the PPC detector, but with a central contact hole of depth 3.0 cm and radius 0.5 cm. Rather than comparing equal masses, this definition allows comparison of the potential detectors that could be prepared from equally-sized crystal blanks.

The time needed for full charge collection due to radiation interaction is determined using the dynamics of charge carrier propagation in a semiconductor following Ramo and Shockley [47, 46, 48]. Full charge collection time for the idealized PPC detector is generally longer than an equivalent idealized p-type coaxial detector. As already stated, the charge

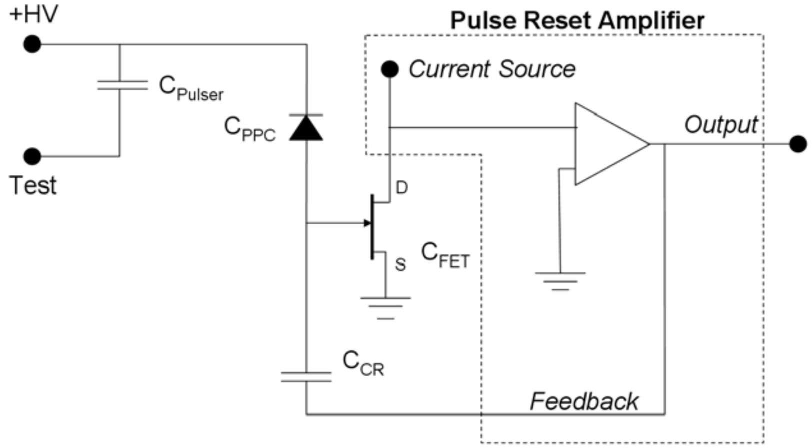

Figure 5.3: Simplified schematic of a typical HPGe preamplifier circuit focusing on the contributions to the front end capacitance. The PPC preamp may or may not have a Feedback loop in the circuit.

collection time is a constraint on the acceptability of the detector. Low electric fields, charge trapping, and ballistic deficit are important additional considerations with respect to the PPC design. Relative to a typical coaxial p-type, the PPC detector design will have larger regions of volume where the charge carrier velocity is below the saturation velocity due to low electric field strength along the axis [74, 75, 68]. Furthermore, on average the PPC design has longer path lengths for the charge carriers to reach collection electrodes. These two features conspire to increase the probability of charge trapping resulting in poor detector performance. However this possibility can be assessed using an IEEE measurement standard [66].

At full operating bias voltage, a high purity germanium detector is in essence a very large reverse biased pn-junction where the p (or n) region extends over the entire volume of the crystal. As the voltage on one contact is increased the width of the depleted region extends further into the crystal volume until it extends all the way to other electrode.

At this bias voltage ($V_{\text{bias}}^{\text{Depleted}}$) the crystal is fully depleted and the detector capacitance ($C_{\text{PPC}}^{\text{Depleted}}$) is determined by the physical geometry of the electrodes combined with the permittivity of the material. The detector capacitance is determined from $FWHM = (41eV)V_n(C_F + C_D)/\sqrt{\Delta t}$ from Ref. [8]. The FWHM value is known from Fig. 8 of Ref. [8] by inspection of the series noise at short shaping times ($\Delta t = 0.5$ ms). Information on the EuriFET ($C_{\text{FET}} = 0.9$ pF and $V_n = 1.6$ nV/$\sqrt{\text{Hz}}$) provide the remaining values to determine the detector's capacitance: $C_{\text{PPC}}^{\text{Depleted}} = 1.8$ pF. This value was used to determine the diameter (0.62 cm) of the point contact. This dimension was not supplied by the manufacturer but is needed for modeling the detector's electric field at bias voltages less than depletion.

Detector capacitance measured as a function of bias voltage is sensitive to the impurity profile of the crystal. It is possible to make a depletion capacitance measurement of a germanium detector using a standard pulser. The relevant consideration is the total capacitance of the detector and front end circuit shown in Fig. 5.3 and mathematically represented by

$$C_{\text{Total}} = \frac{1}{\frac{1}{C_{\text{PPC}}} + \frac{1}{C_{\text{Pulser}}}} + C_{\text{FET}} + C_{\text{CR}}. \tag{5.2}$$

The capacitance of the FET and test pulser input ($C_{\text{Pulser}} = 10$ nF) are known. Gamma-rays of known energy are used to establish an energy scale for the acquisition system at full depletion bias. The test pulser is connected and the output voltage is adjusted to place the pulser peak at a chosen energy in the gamma-ray spectrum. The centroid energy of the pulser peak, $E_{\text{Pulse}}^{\text{Depleted}}$, corresponds to a fixed amount of charge injected by the pulser, $Q_{\text{Pulse}}^{\text{Depleted}}$, as determined by the 2.96 eV of energy needed to liberate a single charge carrier pair on average in germanium. Setting C_{Total} equal to $Q_{\text{Pulse}}^{\text{Depleted}}/V_{\text{Pulse}}^{\text{Depleted}}$ determines

$V_{\mathrm{Pulse}}^{\mathrm{Depleted}}$, the voltage seen at the FET gate induced by the pulser. When the bias voltage is less than the depletion voltage the test pulser voltage remains fixed. However, the capacitance of the detector has changed and becomes a function of the bias voltage, $C_{\mathrm{PPC}}(V_{\mathrm{Bias}})$. The changed detector capacitance results in a changed amount of charge injected at the FET gate. This effect is measured as a displacement of the location of the pulse peak in the gamma-ray spectrum. From the gamma-ray spectrum's energy scale, the amount of charge represented by the location of the pulser peak is determined as a function of bias voltage, $Q_{\mathrm{Pulse}}(V_{\mathrm{Bias}})$. Setting $Q_{\mathrm{Pulse}}(V_{\mathrm{Bias}})/V_{\mathrm{Pulse}}^{\mathrm{Depleted}}$ equal to C_{Total} gives the detector capacitance as a function of bias voltage, $C_{\mathrm{PPC}}(V_{\mathrm{Bias}})$. A measurement of the prototype PPC detector was conducted in the manner described above.

5.4 Results

A successful impurity profile for a common p-type coaxial detector has the greatest impurity concentration at the closed end of the detector, decreasing toward the open end. If a point contact is simply substituted for a common p-type coaxial detector, the simulation predicts a local minimum in the potential above the central contact. This local minimum is difficult if not impossible to to remove except with the most extreme voltages applied. The solution is to reverse the direction of the impurity gradient. This is essentially a flipped orientation relative to the common p-type coaxial design.

The depletion voltage for the PPC detector as a function of the parameter space is given in Fig. 5.4. The figure shows the depletion voltage as a shaded surface in the 2-D parameter space The lightest part, the lower edge, represents the maximum reasonable depletion voltage of 5000 V. The darkest part, the upper left corner, represents the lowest

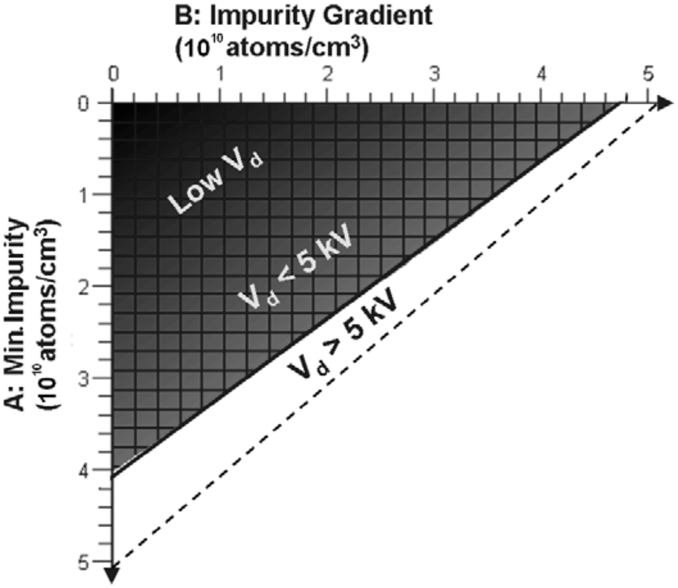

Figure 5.4: Calculated depletion voltage for given values of minimum charge impurity and charge impurity profile. Dark to light shading represents low to high depletion voltage respectively. The computation was cutoff at 5000 V. The darkest shading represents 0 V. Imposing a lower bound of 1000 V would only remove a small region very close to the origin.

depletion voltage. A cutoff for a lowest depletion voltage is not included in this graph. Note that low depletion voltages imply long collection times, which is undesirable and discussed further below. There are other practical limitations imposed by the crystal growth; intrinsic germanium radiation detectors are rarely reported to have impurity concentrations less than 0.1×10^{10} cm^{-3} or greater than 5×10^{10} cm^{-3}. These rough bounds set the reasonable range of the impurity. The wide range of impurity profiles producing acceptable detectors in terms of attainable depletion voltage as shown in Fig. 5.4. The typical coaxial p-type detector design has a larger acceptable range of A and B values (shown by the dashed line), yet given equivalent external crystal dimensions the two are not significantly different.

The charge collection time as a function of the A and B parameter space is given in Fig. 5.5. The figure shows the maximum charge collection time as a function of the parameter space. The charge collection time has a range from 250 to 2000 ns. Very long collection times such as 2000 ns would lead to poor detector performance. PPC detectors will generally have longer charge collection times in comparison to common p-type coaxial detectors of the same external crystal dimensions.

Investigating the capacitance of these detectors, the prototype PPC detector [8] capacitance (C_{PPC}) was measured as a function of bias voltage. Fig. 5.6 compares this measurement to simulation using the same dimensions and the two parameter model in equation 5.1. A suggested relation of $B = A$ [76], which is consistent with those impurity concentration values reported in [68], is needed for a solution of the depleted detector capacitance using the measured detector depletion voltage, 2500 V. The simulation reproduces the charge collection time of 700 ns as seen in the bottom of Fig. 11 in Ref. [8].

Note that the two capacitance curves do not match up at voltages below the

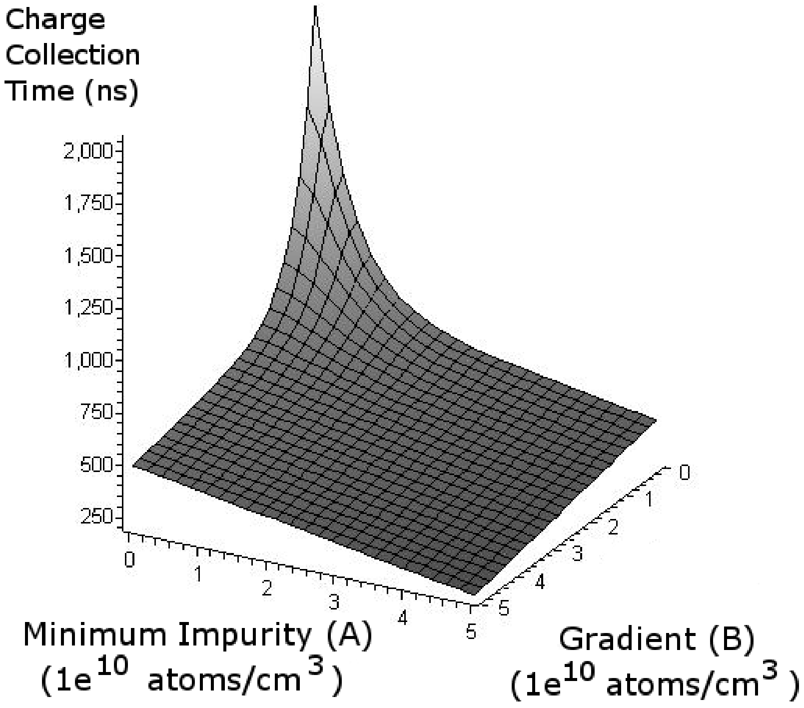

Figure 5.5: Calculated charge collection time surface parameterized by A and B. The prototype PPC showed a charge collection of up to 700 ns.

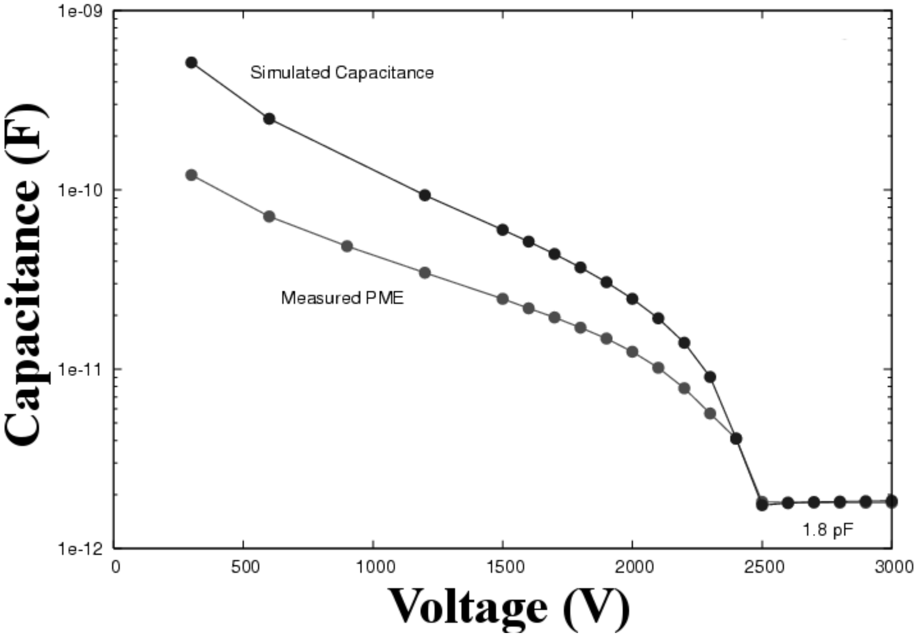

Figure 5.6: Capacitance versus bias voltage for the prototype PPC [8] compared with simulation.

full depletion voltage. This likely demonstrates demonstrates the need to add a radial component to the model of the impurity concentration, equation 5.1. This hypothesis is based on the results from an impurity concentration model having an *ad hoc* exponential dependence on the radius. The degree of freedom provided by the radial dependence allows different capacitance values at voltages less than full depletion. We explore the details of the depletion capacitance and it measurement in chapter 6.

5.5 Conclusion

This work explores the relationship between germanium crystal impurity concentrations and the performance of detectors having the PPC design. Using a field simulation for high purity germanium crystals, the range of charge impurity concentrations and profiles that will produce acceptable detectors is predicted. Detector acceptability is defined by explicit calculation of depletion voltages and charge collection times. These measures are used to compare with the first operational PPC detector [8].

This work shows that with current manufacturing methods, production of the PPC detector design is confined to a range of impurity concentrations and profiles only slightly smaller than a typical p-type coaxial germanium detector. Thus it is concluded PPC detectors have the potential to become a moderately priced and universally available resource for future applications.

Finally, this work suggests greater attention must be given to the *radial* impurity concentration profile for complete understanding of the charge collection properties of the PPC detector design. This subject is explored in chapter 6.

Chapter 6

Determination of the Impurity Profile for a PPC Detector

6.1 Introduction

In the previous chapter we have shown that a PPC type detector may be made from a wide range of impurity profiles. In this chapter we seek to demonstrate how to measure the profile of a PPC detector. A method for using the measured capacitance versus the applied voltage combined with appropriate simulations to model the impurity profile is developed. A similar method for using an efficiency versus applied voltage, as well as the commonly used four point resistance method is explained and contrasted to the capacitance method developed.

Experimental characterization of an impurity profile for a detector can be resource intensive and time consuming. Advanced PSA often uses a library of pulse shapes. To statistically characterize the pulse shapes based on interaction position can take months. However, the only alternative is simulation of the pulses as a function of position. If simulations are to be used to build a library of pulse shapes, then a very good model for the charge impurity density must be obtained. We demonstrate a method of solving for the charge impurity density as a function of height and radius with a simple capacitance measurement. This measurement gives the solution for a three parameter 2 dimensional charge impurity density model. This can be used to simulate the electrical properties and response of a solid state radiation detector.

There are only three ways to find the charge impurity model, one is an efficiency scan and subsequent fit, another is a resistance measurement done at the manufacturer, the third is a capacitance measurement and a subsequent fit. A scan to statistically characterize the pulse shapes based on interaction position can only be used to build a pulse shape library, and without a good model for the charged impurity profile. However, no modeling work can be done to optimize any of the parameters for a particular experiment or physical process signature without a charged impurity profile.

Pulse shape analysis (PSA) can be distinguished into two categories: parametric and library. Parametric PSA uses specific parameters of the pulses to establish whether a given pulse satisfies a given set of criteria. Common parameters include energy and charge collection time. Library PSA builds a library of basis pulse shapes from which any pulse can be reconstructed. Each experimental pulse is then compared to the library of pulses to find a best match or a set of best possible matches. This corresponds to the position of the interaction [77, 6, 78].

There are two approaches to making a library of pulse shapes. One can experimentally scan a detector with highly collimated sources to produce a statistical pulse shape for a set of interaction positions [31]. This can take months to complete for a single crystal. The alternative is a parametric approach that uses computational modeling techniques to build the pulse shape library. The computational method is very fast, yet its effectiveness depends on the level of validation with experimental observables that can be achieved.

We present a method of doing a simple capacitance versus voltage measurement to solve for the 2 dimensional charge impurity density equation with the third dimension being symmetric. Given boundary conditions on the radius and height a 2 dimensional solution guarantees a unique solution for this set of 2 dimensional boundary conditions. Given this insight, the question becomes one of how sensitive are these measurements to computational solutions and local deviations.

6.2 Physics of HPGe Detector Capacitance

For a depleted detector, the capacitance is completely determined by the geometry of the conductors and the dielectric constant of the materials. Therefore the capacitance of a true coaxial detector is given by the capacitance of two cylinders [6, 36]. If the crystal is not depleted, then the capacitance takes a very different form.

In many modern text books on materials and their electrical properties we will find the capacitance that relates the charge on a conducting surface to the voltage applied for a p-n junction is termed the depletion capacitance [45]. The capacitance for reverse biased p-n junctions is defined this way and using the energy stored in the electric field can give very different and incorrect results.

A p-n junction has two basic types of capacitance. The first type is the differential storage capacitance or diffusion capacitance which arises from a rearrangement of the minority carrier distribution due to diffusion into the bulk semiconductor as the voltage is changed [79]. Differential storage capacitance is dominant under forward bias conditions. The second type of junction capacitance is the transition capacitance or depletion-layer capacitance. It is due to the variation of space charge with voltage in the depletion region and is dominant under reverse bias conditions [45].

A transition capacitance is the result of the flow of majority carriers that changes the widths of the total n and p space charge regions in response to a change in the applied reverse bias potential V. A capacitance calculated from the total energy of the electric field will give an incorrect result because it cannot account for energy lost to the lattice due to scattering of the charge carriers as the boundary changes.

The variation of the space charge with an applied bias is due to the movement of majority carriers in and out of the depletion zones. This is a very fast process that takes on the order of picoseconds. Time constants associated with these charge variations can therefore be neglected, and the associated capacitances can be considered frequency independent [45].

Using the definition of the transition capacitance

$$C_t = \left| \frac{dQ}{dV} \right| \tag{6.1}$$

as we increase the voltage, the depletion region of the junction changes. The dopant or acceptor is neutral until this voltage sweeps away the neutralizing charge creating a space charge. HPGe detectors are neutral except for the very thin natural p-n junction. As the reverse bias inducing applied voltage to an electrode increases this p-n junction grows toward the opposing electrode. This wide p-n junction region forms an active detector region. As this active detector region grows charges from the dopant's are swept away leaving a net charge in the region as in Fig. 6.1. This net charge induces its own electric field which adds by the principle of linear super position to the electric field due to the applied voltage as illustrated in Fig. 2.4. In a p-type material the resulting space charge in the active

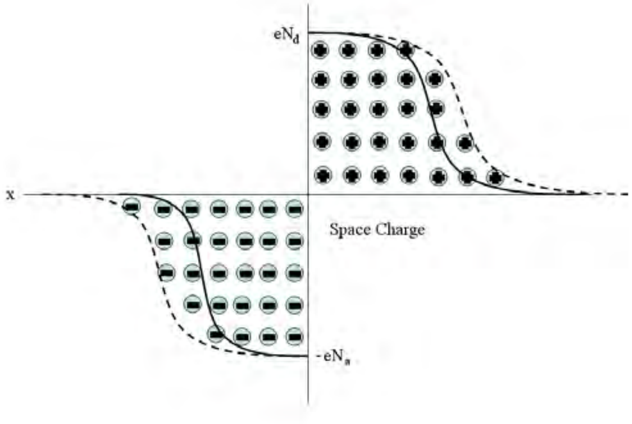

Figure 6.1: Effects of a reverse bias on a p-n junction. As the voltage increases, the amount of the charge in both the acceptor and donor regions increase by the regions increasing in volume.

region is thus negative, conversely for an n-type material the active region is positive. The charge is not completely displaced as a current to ground, but instead redistributed onto the boundary between the active and inactive regions. The contacts and the undepleted region are thus treated as conductors.

Given this definition of the depletion capacitance, we can integrate the depletion capacitance to get the total impurity charge in a crystal.

$$\int_{Voltage} C_t dV = Q = \int_{Volume} \rho(r')d\tau' \tag{6.2}$$

Integrating over the space charge in the active region and dividing by the voltage applied is the calculation that gives you the true capacitance of the undepleted detector. Using the energy stored in the fields will often produce the wrong result [79, 39].

If we assume a simple function for the charge impurity profile of

$$\rho(r, z) = A + Br + Cz \tag{6.3}$$

We can then use the definition of the capacitance to pin down one of the parameters. The most obvious parameter being the constant term A. The integration limits are therefore the radius R and the height H of the detector. Integrating over the experimentally obtained capacitance as a function of voltage, up to the depletion voltage, we have a value for the charge Q. Then

$$\int C(V)dV = Q = \int \rho(r,z)d\tau = 2\pi \int_0^H \int_0^R (A + Br + Cz) r dr dz \tag{6.4}$$

giving a parameterized limit to the three parameters $\{A, B, C\}$. Using this integrated charge as a limit will greatly decrease the size of the parameter space that must be modelled.

6.2.1 Electronic noise and capacitance

The capacitance of an HPGe detector is not of secondary consideration. The capacitance of the system including the HPGe detector influences strongly the electronic noise of the system. The noise level of an HPGe detector is conveniently given as the equivalent noise charge Q_n. The equivalent noise charge is amount of deposited charge that gives a signal to noise ratio of one [66]. For and HPGe detector the equivalent noise charge is:

$$Q_n^2 = i_n^2 F_i T_S + e_n^2 F_v \frac{C^2}{T_S} + F_{vf} A_f C^2 \tag{6.5}$$

where C is the sum of all of the capacitances shunting the input. The constants F_i,F_v and F_{vf} come from the shape of the pulse, T_S is a characteristic time of the circuit [58]. We can see that the electronics noise contributions are related to the capacitance.

In Pulse Shape Analysis (PSA) methods the slope of the pulse to the noise must be optimized in addition to the signal to noise ration alone. The jitter of the timing distribution is:

$$\sigma_t \approx \frac{t_r}{S/N} \tag{6.6}$$

where t_r is the rise time of the amplifier. To increase dS/dt without excessive noise the amplifier bandwidth should match the rise time of the voltage pulse. Often the rise time of the voltage pulse is given as the 10% to 90% CFD rise time of the pulse [66]. The rise time of the amplifier is given as:

$$t_r = \frac{0.35}{f_u} \tag{6.7}$$

with f_u being the amplifier bandwidth in Hertz. When amplifiers are chained together the individual rise times add in quadrature as:

$$t_r \approx \sqrt{t_{r1}^2 + t_{r2}^2 + \ldots} \tag{6.8}$$

Thus for good PSA, improving the signal to noise ratio will improve the time resolution so minimizing the total capacitance at the input is very important.

6.3 Capacitance Measurement

The capacitance of an undepleted crystal can be measured at any applied voltage by injecting a small voltage pulse into the crystal. Most HPGe detectors are made such that the test pulse input bypasses the detector. In some detectors, like the PPC, the test pulse input connects to the high voltage line allowing the pulse to travel through the crystal. A simplified circuit diagram is given in Fig. 5.3. If the test pulse input bypasses the detector, a line can be placed is such proximity to capacitively couple to the high voltage line and inject test pulses through the crystal.

The voltages pulses were 20 mV square waves with a 20 ms duration. The 20 mV test pulse, ΔV is on top of the constant applied voltage V. At each applied voltage, the detector system was run in multi-channel analyzer, **(MCA)**, mode recording the ADC values of the test pulses as if they were radiation events. The test pulses will produce a Gaussian peak in the histogram whose peak position and FWHM is recorded for that applied voltage. This procedure is repeated for each applied voltage of interest. The test pulse peak will stop changing once the applied voltage is above the depletion voltage. The results of this procedure on the PNNL PPC detector are recorded in Fig. 6.2.

A radiation source of know energy is used to calibrate the energy histogram. The calibration will give the gain of the system

$$G = \frac{E_{peak}(eV)}{ADC_{peak}} \tag{6.9}$$

Using this gain on the test pulse peaks P_i, for each voltage i, we have the number of electrons produced

$$N_e = \frac{P_i \cdot G}{2.96(eV/e^-)} \tag{6.10}$$

, where 2.96 eV per electron is the energy per electron hole pair in germanium [6]. The number of electrons can then be easily converted into Coulombs of charge produced in the detector for use in the capacitance at each applied voltage.

$$C(V_i) = \frac{\frac{(1.602\times10^{-19}C)P_i \cdot G}{2.96(eV/e^-)}}{20(mV)} \tag{6.11}$$

The capacitance as a function of applied voltage is now correctly in units of farads as show in Fig. 6.3.

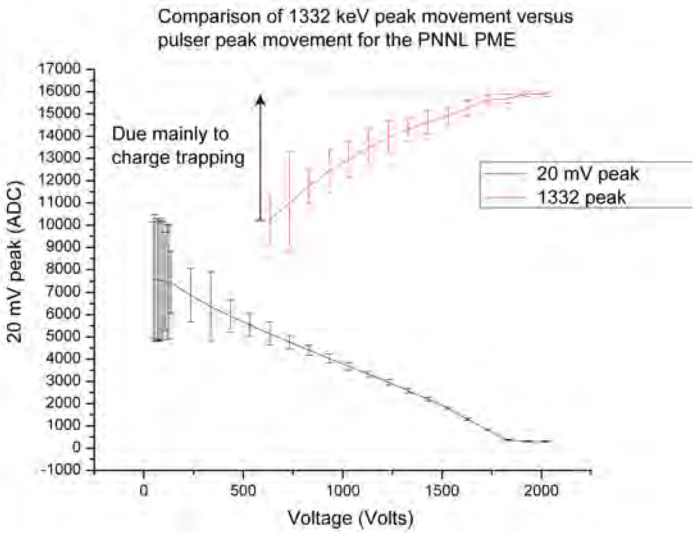

Figure 6.2: Capacitance measurement of a HPGe detector using injected voltage pulse, compared to ^{60}Co 1332 keV peak.

6.4 Impurity profile from Capacitance

The model for the charged impurity profile is a three parameter 2 dimensional equation given by:

$$\rho(r, z) = A + Br + Cz \tag{6.12}$$

where A,B and C are simply the parameter space with the appropriate units. The parameter set is exceedingly large and until we calculate the capacitances we do not know how close we are to a good model. Calculating the capacitances is a very CPU intensive process, thus we must use a small subset of the $\{A, B, C\}$ parameter set. The necessary limit is given by integrating the capacitance as a function of voltage, giving the total charge Q of the detector.

$$Q = \int C(V)dV = \int_{Volume} \rho(r, z)d\tau \tag{6.13}$$

The model for $\rho(r, z)$ given above is easily integrated given the radius and height. The measured capacitance as a function of voltage does have an associated error as well as lower limit of 300 Volts. To account for this unknown region of the capacitance we set a 10% upper and lower bound on the integrated charge. Thus we generate a parameter space file for all $\{A, B, C\}$ sets whose integrated value is in the range $Q \pm 10\%$. The range needs to wide enough to account for the unknown region of the capacitance measurement while being small enough to allow the problem to be tractable. The parameter space should allow for negative values of parameters B and C.

A model of the charged impurity density will allows simulation of the capacitance at any voltage below depletion. The capacitance is simulated using the CRT code. CRT calculates the capacitance very simply, by first calculating the potentials at the applied voltage V. The total charge in the active region is integrated as Q_1. Then a ΔV of 20 mV is added to the applied voltage and the potential is calculated. The total charge is again calculated in the new active region as Q_2. Thus the capacitance is simply:

$$C(V) = \frac{Q_2 - Q_1}{\Delta V} \tag{6.14}$$

CRT reads in each parameter set $\{A, B, C\}$ giving the charged impurity density $\rho(r, z)$. CRT then calculates the capacitance at each voltage given in the measured capacitance curve. The χ^2 is then calculated using the resulting capacitance curve and the measured capacitance curve. This process is repeated for each parameter set until χ^2 is less than 1. Associating the χ^2 with each parameter set in the parameter space shows a very non-linear solutions set. The fitted parameter coordinates are surprisingly sensitive to the parameter space. Thus minimization methods do not become effective until they are sufficiently close to the solution coordinates. Several minimization routines were used, but

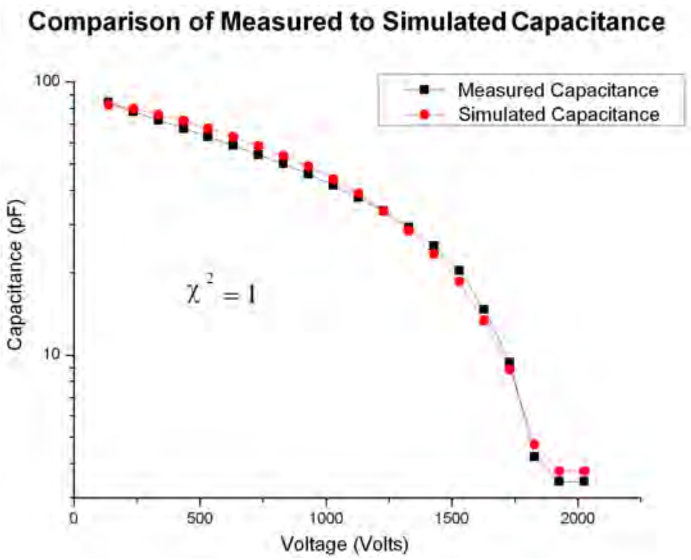

Figure 6.3: Iterating over a parameter space of the charge impurity profile, a fit to the capacitance was found.

none proved more efficient than straight forward iteration until a solution was found. This calculation will remain CPU intensive until an effective minimization routine is found.

6.5 Efficiency Method for Impurity Profile

In this method a count of the events in a given peak at each voltage with a collimated γ source at several positions along the height of the crystal. The number of counts in the peak, for each height for each voltage is proportional to the amount of volume exposed to the γ rays. Taking many such measurements with a good knowledge of the total volume should allow one to solve for the area of each height at a given voltage. This in turn could produce a charge impurity profile as well as active volume versus voltage.

A ^{60}Co source was placed between two lead slabs and aligned such that the collimated source irradiated a thin slice if the detector perpendicular to its axis. At a given voltage, below depletion, only the active area will respond. The energy histograms were recorded for 30 seconds with the collimated source at each of four heights from the base for each voltage. The number of counts in a peak for some height at some voltage should relate to the relative active area of the detector at that voltage. The measurement was made at the University of Chicago and the results are given in Fig. 6.4.

The computational approach is much the same as with the capacitance approach. CRT reads in the parameter set for the charged impurity model, and solves for the potential at the given voltage. CRT then records the active region due to the calculated potential. CRT then reads in a Monte Carlo of the detector with the appropriate collimated source, recording the energies in a histogram of all events depositing energy in the active region. The energy peaks are then compared to the measured energy peaks. The errors were to significant to differentiate between a wide range of parameter sets.

There are many other drawbacks to this method. A fairly hot source needs to be used to achieve a high signal to background as well as to be able to perform the measurements in reasonable time. The γ rays scatter such that the radiation field volumes overlap leading to spatial errors. As the voltage decreases below the depletion voltage the error, due to very poor charge collection, increases well beyond any usable form. Thus the changing nature of the charge collection as a function of voltage adds a great deal of uncertainty to this method. Ultimately this method was determined to be inadequate due to the statistical errors inherent to the measurement and the insensitivity of the computational solution set.

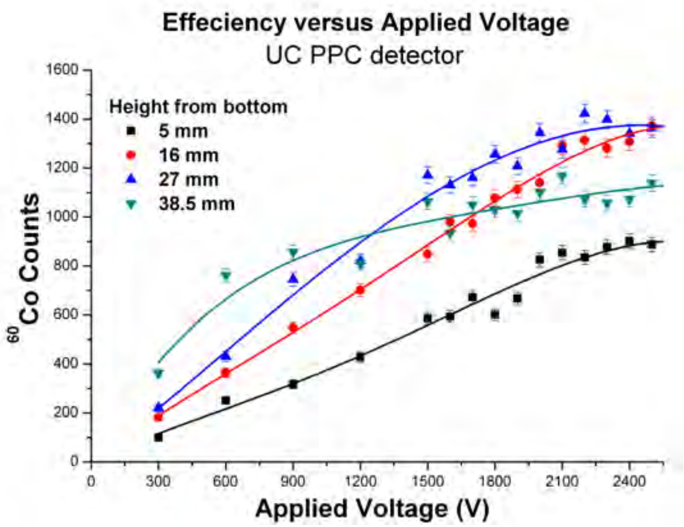

Figure 6.4: The Number of counts for a collimated ^{60}Co source placed at four different heights versus the applied bias voltage of the University of Chicago PPC detector. As the applied voltage increases, the active volume increases thus the number of counts should increase proportionately.

6.6 Four point Resistance Measurement

This method is common for manufactures to use on an HPGe crystal. The benefit to manufactures is that it must be performed on an HPGe crystal before any surface treatments, thus it can act as a quality control where the crystal can be rejected before expensive treatments if the resistance is not in a specific range for a functioning HPGe detector.

This method measures the resistance which is related to the charged impurities. The drawbacks of this method are that it measures the resistance very close to the surface, it is only performed when necessary, it supplies only a couple of points, it can be off by as much as 30%. The method can only be performed by the manufacture and gives insufficient information with which to base simulations.

The resistivity of a semiconductor is defined as:

$$R = \frac{1}{nq(\mu_e + \mu_h)} \tag{6.15}$$

where n is the free electron and hole concentrations, and μ_e and μ_e are the electron and hole mobilities[80]. This resistivity can be measured in many ways, but sharing some very common traits. The most common from semi-conductor manufactures is the four point probe[80]. The four probes are generally arranges in-line with equal spacing between them. Two probes carry the current while the other two probes measure the voltage derived from the simple relationship:

$$V = \frac{RI}{2\pi r} \tag{6.16}$$

Assuming equal spacing (s) between the probes, the total resistant can be given as

$$R = 2\pi sF(\frac{V}{I}) \tag{6.17}$$

where the most common spacings are 0.635 mm and 1.588 mm [80]. F is the correction factors necessary to account for the edge effects, thickness effects, probe placement effects and several other independent correction factors. The correction factors needed are much more complex than the simple equation for the resistance. Common sources of error include sample size, minority carrier injection, probe spacing, current effects and temperature effects.

According to Schroder:

> Conventional four-point probe measurements give an average resistivity. This is suitable for uniformly doped substrates but is not sufficient for non-uniformly doped samples in which the resistivity profiles need to be determined. [80].

The charge carrier dopant concentration (majority carrier) is related to the resistivity, but it is not usually derived from it. Resistivity measurements are often preformed by HPGe detector manufactures. given that the current flows at only very shallow depths it will not give detailed information about a detector. Assuming a well behaved impurity concentration, measurements typically measure the resistance at four points, two at either end of crystal center and two at either end of the outer radius. Giving a linear profile. These measurements differ from the absolute impurity concentration by as much as 30 percent [9, 81], however maintain good relative information.

The path of the current typically will have a small diffusion width and direct path between the source and drain of the current. Only with extensive and complex sets of measurements could the bulk of the material be sampled. Even if this were feasible for HPGe detectors, the effort required would dissuade any manufacture from attempting it. Manufactures apply a passivation and metalized surface to HPGe crystals, resistance measurements must be made on bare crystal, thus a resistance measurement can only be done by the manufacture.

6.7 Pulse Shape Library from a Scan

A library of pulse shapes can be made for an HPGe detector. The general method involves two setup in a Compton scattering technique. A collimated source is incident on the detector of interest, while a second detector is placed relative to the detector of interest to maximize a Compton scatter. This second detector will also be collimated to the fist detector and shielded from the source. A data set is collected with these two detectors in coincidence and analyzed for a specific combined energy. With large statistics, this method will produce a dataset of dominated by energy depositions from the intersection of the source and second detector collimation paths in the detector of interest. A scan is very resource intensive, as well it takes a very long time to complete, on the order of months per detector.

6.8 Conclusion

We have reviewed the physics of capacitance in an HPGe detector. We have written code that can correctly give the capacitance for an undepleted HPGe detector, given a charged impurity density. The dependence of the capacitance on the charged impurity profile for an undepleted HPGe detector allows an iterative search for the best charged impurity model. A three parameter 2D model of the charged impurity density was used to fit the measured capacitance curve for the PNNL PME detector.

Chapter 7

Position Resolution

7.1 Overview

The position resolution for ionizing events in HPGe detectors fundamentally limits the efficacy of multiple site cuts The position resolution is difficult to analyze in general, however, as it it depends on a host of factors which we divide broadly into intrinsic factors characterizing the spatial ionization distribution and technical factors associated with detector and readout design. In what follows we explore these factors and how they influence the position resolution of P-type Point Contact detectors.

7.2 Factors affecting position resolution

7.2.1 Intrinsic Factors

A number of physical aspects closely related to the detection process impose a fundamental limit in the attainable position resolution. The finite length of the photoelectron's ionization path, and the spatial distribution of the charge carrier clouds formed following photoelectron-induced excitations place a lower bound on the precision with which we can identify the formation of charge carriers that take place in an extended volume. The detector technology we consider does have the capability to reconstruct the three dimensional path of the ionization. We must model the effect of the ionization distribution on the time profile of the current signal.

The energetic electrons produced following a γ- interaction in the Ge detector loose their energy in the detector material through ionizations and excitations according to the formula derived by Bethe formula for the linear stopping power S_c [6] of free electrons in a material.

$$S_c = \frac{4\pi e^4 z^2}{m_0 \nu^2} NZ \left[ln\left(\frac{2m_0\nu^2}{I}\right) - ln\left(1 - \frac{\nu^2}{c^2}\right) - \frac{\nu^2}{c^2} \right] \tag{7.1}$$

The velocity and charge of the primary particle are ν and ze, while N and Z are the number density and atomic number of the absorber atoms, m_0 is the electron rest mass. The parameter I represents the average excitation and ionization potential of the absorber atoms. Besides the energy loss through excitations and ionizations, the electrons lose energy by radiating bremsstrahlung due to deflections of their trajectories, but the proportion of energy loss through this process is small for the energies of interest here. Eq. 7.2 represents the radiative stopping power S_r for energetic electrons[6].

$$S_r = \frac{NEZ(Z+1)e^4}{137 m_0^2 c^4} \left[4ln\left(\frac{2E}{m_0 c^2}\right) - \frac{4}{3} \right] \tag{7.2}$$

where E is the energy of the primary particle. An approximation for the ratio between the two specific energy losses is given by the formula:

$$\frac{S_r}{S_c} \approx \frac{EZ}{700} \tag{7.3}$$

with the photoelectron energy E expressed in MeV, and $Z = 32$ for Ge. Fortunately, the produced bremsstrahlung is predominately low energy and is absorbed in close proximity the the site of the initial bremsstrahlung interaction.

Besides the spatial range of the charge carrier formation during the event ionization, the charge carriers diffuse as they drift through the detector and its electric field leading to a spatial distribution often referred to as a charge cloud. As a consequence, the electrons and holes will have individual paths through the weighting fields for each electrode, thus forming different induced signals on each detector electrode. Hence the resulting signal on a given electrode will be an integral over a distribution of signal shapes.

7.2.2 Technical Factors

In the category of technical factors which influence the position sensitivity are those which result from the design of the detector and of the read-out electronics. Theoretically, these factors can be adjusted for better performance, through better knowledge of the involved physical processes and a better technical design.

Good control of the signal shapes corresponding to a particular interaction site, and to be able to accurately simulate these signals, the charge collection process must be well known within the entire active volume, and the weighting fields of each electrode must be be carefully calculated. There are a few factors which hinder precise characterization of charge collection processes and the weighting fields. The normal design of any HPGe detector involves the existence of at least one active surface between the electrodes of opposite polarity. This surface is treated to minimize surface leakage currents by etching and passivation. Unfortunately, the influence of the passivation material on the electrostatic fields is not very well understood. Ideally, such surfaces should behave as electrostatic mirrors, corresponding to Neumann boarder conditions [39]. Since for the moment, the technology is not fully developed and the knowledge of the influence of surfaces on the electrical field is approximate, one should account for the existence of electric field inhomogeneities especially at the edges of the detector. This limits the knowledge of the charge collection process, as well as the accuracy of the calculated weighting fields of the segments which are adjacent to the open surfaces.

As presented in chapter 4, the electrostatic field in the detector varies with the concentration of the spatial charges which exist in the depleted detector volume. These charges are formed at the places where impurities exist, and therefore, the distribution of the impurity concentration will determine the charge distribution, and consequently, will affect locally the electrostatic field. In the detector production, variations of the impurity concentration are unavoidable. An accurate determination of this distribution will improve our estimate of the local electrostatic field.

The empirical model of the charge carrier drift velocity, Eq. 3.1, and its variation with the electric field is also an model. Moreover, variations of the bias voltage or temperature lead to variations in the drift velocity of the charge carriers, inducing different signals.

The influence of the limited preamplifier bandwidth on the shapes of the detector segment signals is often referred to as ballistic deficit. Ballistic deficit comes from the read out electronics and directly affects the energy resolution [66]. This is an important limitation, since valuable information which exists in the detector signal is typically lost in the preamplifier output signal. Moreover, the unavoidable detector and electronics noise will further distort the signal shapes.

7.2.3 Consequences

Due to uncertainties in the charge collection process, the assumptions taken for pulse shape simulations used in creating the database of signal shapes for each discernible interaction site must be checked and directly compared with experimental values. By measuring experimental signals produced by single interactions in several well defined regions using a Compton spectrometer, the parameters used in the simulation can be adjusted to reproduce the experimental shapes. In this way, variations in the distribution of the impurity concentration and the charge carrier drift velocity can be estimated.

Another possible method to circumvent the missing knowledge in the signal shape formation is to preform a scan with highly collimated γ-ray sources over the entire volume of the detector, and to directly use the experimental shapes in the data base of patterns. The resultant grid of signal types can be refined by interpolation between the experimentally determined pulse shapes. Obviously, such a procedure is time-consuming, and impractical, more so when applied to a very large number of detectors, as would be required for a large neutrinoless double beta decay experiment. In any case, one of the two methods must be applied to avoid systematical errors in position determination.

For single interactions, the position resolution will be finite, the ultimate limitation being the dimension of the charge carrier clouds. Besides this, depending on the local variations of the signal features, which can have different levels of discrimination applicability for different positions, the position reconstruction precision will vary at different interaction locations. Finally, the signal-to-noise ratio of the detected signal, which is a function of the deposited energy, will influence also the precision of the position resolution. Ultimately, the signal-to-noise ratio can be improved simply by reducing the noise, by an improved design of the analog section of the electronics, and by using sampling ADC's with a larger number of bits.

For multiple interactions, due to the distribution of the charge carrier clouds, electronic noise and preamplifier shaping, the decomposition of the signals will be a mathematically ill-posed problem. Especially for interactions lying close together, for other particular combinations of interactions, it will not be possible to decompose them uniquely. In principle, this limitation has to be considered in the design of an optimized tracking algorithm. Moreover, to optimally extract the available information by pulse shape analysis, a Bayesian approach for the decomposition of multiple interactions can be followed by taking into account the statistics of the γ-ray scattering process. Thus, the distribution of the multiple interactions can be estimated by calculating an a-priori probability using the known released energies. This information can then be included in the pulse shape analysis methods to estimate the relative positions and energies of the interactions.

7.3 Effect of Anisotropic Drift Velocity

HPGe detectors are semiconductors as well as crystals, subject to crystal lattice effects. One such affect is called anisotropic drift velocity [37]. This refers to each charge carrier having a velocity dependence on the crystal orientation relative to the direction of travel. This was discussed in chapter 2 and expanded on in chapter 3. To review, we see from Fig. 2.4 that the band structure is different for different crystal axes. Charge carrier traveling through this lattice scatter to some certain degree off of the charges held tight in the lattice. Different orientations offer different scattering properties and therefore limit the maximum velocity differently.

This effect is known in the field but no current publications address this effect in regards to pulse shape analysis. We built a rotating source holder such that we can place a collimated low energy source at different angles relative to the detector. We used a ^{57}Co source with a 122 keV γ incident on a p-type semi-coaxial 120% relative efficiency HPGe detector, such that all full energy depositions occurred close to the surface, maximizing the path that holes must travel to reach the inner contact. This allowed us to measure the drift velocity at different angles.

The spectra collected are shown in Fig. 7.1. The source was in place for 9 hours in each orientation, the time was monitored closely. We can see the dead layer results in a significant difference in the relative efficiency of each orientation. To account for this the dead layer thickness must be accounted for. Only the relative dead layer needs to be accounted for since the ultimate measures is a difference for the spectra.

To account for the non-uniformity of the dead layer, we begin with the attenuation formula for photons through matter:

$$N = N_0 e^{-\mu t \rho} \tag{7.4}$$

where N_0 is the number of incident photons, t is the thickness normal to the beam, ρ is the density of the material, and μ is the mass attenuation coefficient of the incident material given a specific energy E. The mass attenuation coefficients came from NIST standards, and are given in the Table. 7.1. We find the following simple correction for the number of incident photons in the active region of the detector:

$$N = N_0 e^{[-\mu t \rho]_{Al} + [-\mu t \rho]_{Ge}} \tag{7.5}$$

where t_{Al} is the Al thickness and t_{Ge} is the HPGe detector dead layer thickness. Given all of the parameters being known we can solve for the thickness of the Germanium dead layer t_{Ge}

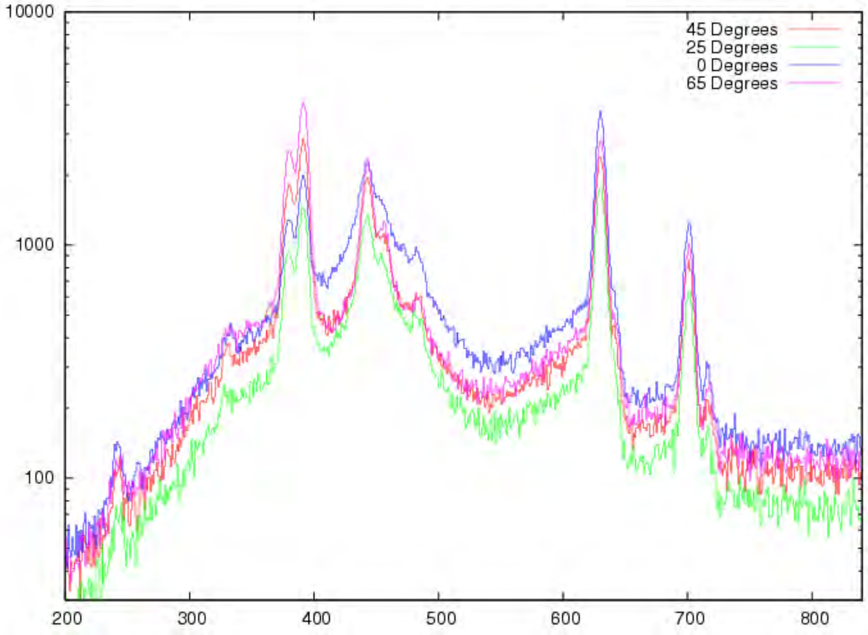

Figure 7.1: Spectra for a 120% HPGe detector for a colimated ^{57}Co source at different angles to the front of the detector.

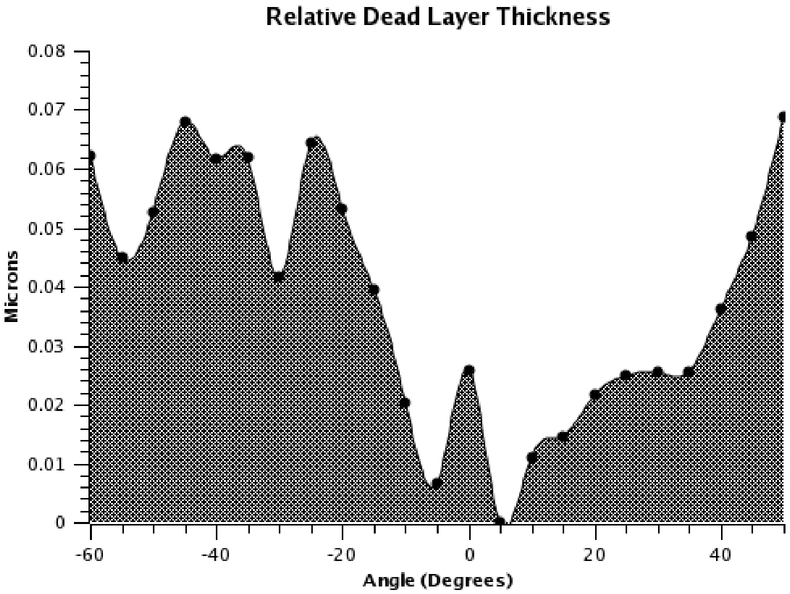

Figure 7.2: The relative dead layer thickness as parsed from the low energy efficiency.

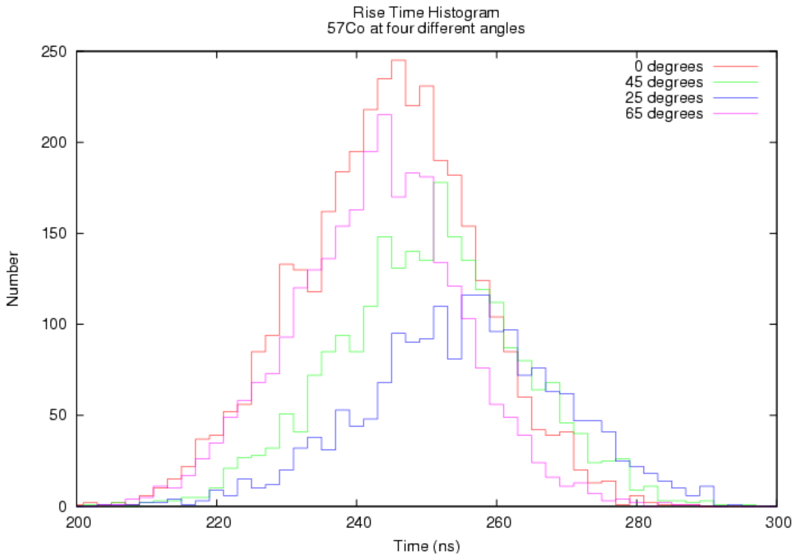

Figure 7.3: Rise time data extracted from the 122 keV peak of the ^{57}Co spectra.

for each angle relative to some well chosen reference position. For this measurement we chose 5° as the relative angle since it gave the thinest dead layer, all other angle measurements are the thickness in addition the thickness at 5°. The results of the dead layer uniformity are given in Fig. 7.2.

Table 7.1: Mass attenuation Coefficients, density, and thicknesses for the materials used in the measurement [5]. Dead layer thicknesses are typically "several hundered micrometers"[6].

Mass attenuation Coefficients of the materials involved			
Material	Attenuation Coefficient $[cm^2/g]$	Density $[g/cm^3]$	Thickness $[cm]$
Aluminum	0.155	2.702	0.050
Germanium	0.405	5.3234	≈ 0.02

Correcting for the dead layer of the detector we can fit a Gaussian peak to the charge collection time of the given energy peak, as in Fig. 7.4, to extract the charge

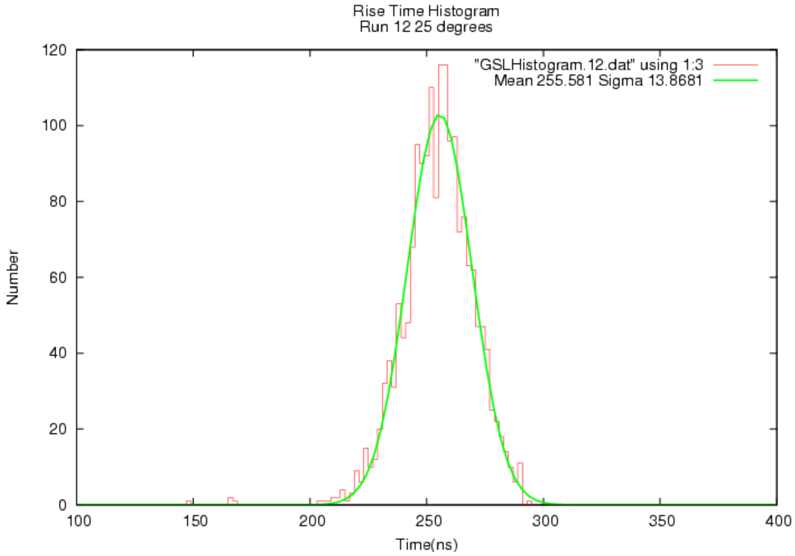

Figure 7.4: A fit to the rise time extracted from the 122 keV peak of the ^{57}Co spectra at 25°.

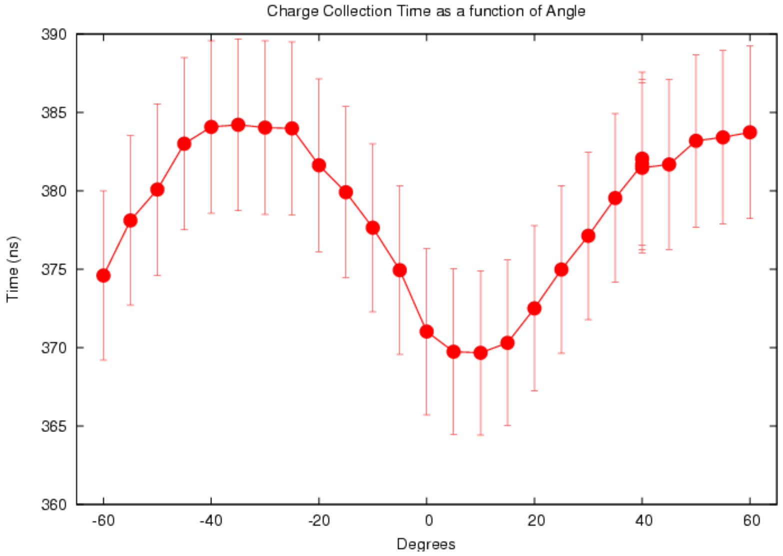

Figure 7.5: The timing for full charge collection of electrons in a p-type HPGe versus angle. The error bars indicate the FWHM of the peak.

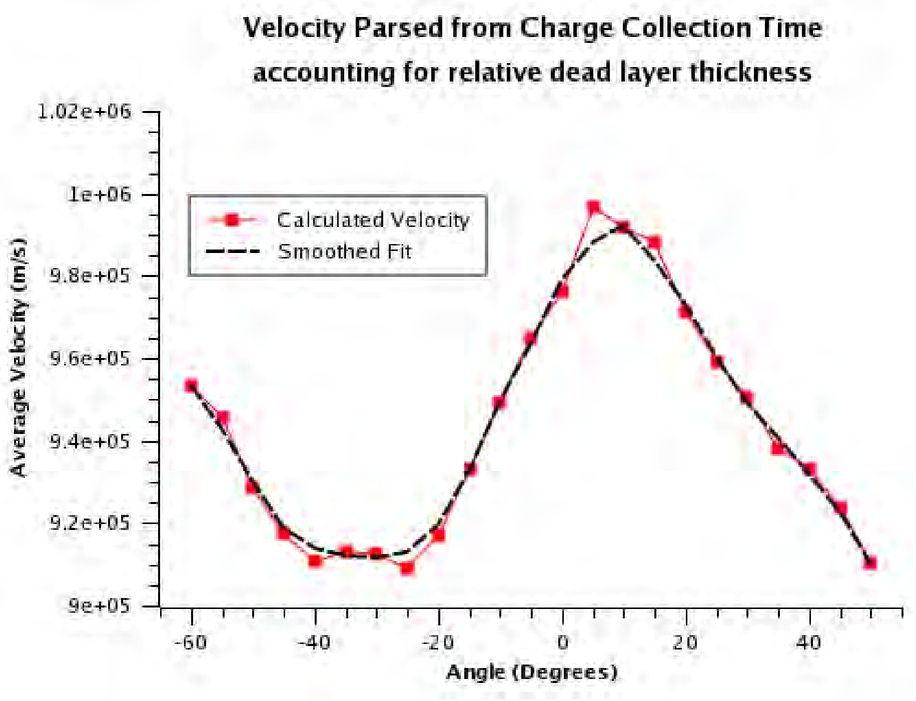

Figure 7.6: The velocity of holes in a p-type HPGe versus angle. Including corrections for dead layer thickness.

collection time. Comparing these charge collection peaks we see the difference in the total charge collection time as illustrated in Fig. 7.3. We can see the difference in the time it takes for the different angles for a p-type semi-coaxial HPGe detector is maximally about 15 ns from Fig. 7.5. Using the results of these fits the dead layer thickness, relative to 5°, and timing information for each angle we can reconstruct the anisotropic drift velocity of the charge carriers versus the angle in Fig. 7.6.

The effect of the anisotropic drift velocity of the charge carriers for an 80 mm p-type semi-coaxial HPGe detector was measured. The maximal difference in the timing for different angles was approximately 15 ns. When the Aalseth PSD method was applied to multiple angular data sets, the difference in the PSD spaces were below the noise threshold. Thus, for this detector it is determined that no angular information can be extracted with this PSD method. Given the design of this detector it is unlikely that angular information can be extracted, using this PSD method, from any semi-coaxial HPGe detector.

7.4 Effect of Finite Carrier Lifetimes

The charge carrier path lengths for a PPC can be significantly longer than those in a semi-coaxial detector. The maximum length a charge carrier will move in a semi-coaxial detector is from the outer radius to the inner radius. In a PPC where the height is roughly equal to the radius then $\frac{1}{3}$ of the volume of the crystal has a path length further then the maximum path length in a semi-coaxial detector. If the height of the PPC is roughly equal to the diameter, then the approximately $\frac{4}{3}$ of the volume of the crystal extends beyond the maximum path length of an equivalent semi-coaxial detector. Given that PPC detectors come in various lengths, the volume that extends beyond the maximum path length of an equivalent semi-coaxial detector can be approximated by:

$$\delta V \approx (\beta - \frac{2}{3})V_{PPC} \tag{7.6}$$

where β relates the PPC height to the PPC Radius as $H_{PPC} = \beta R_{PPC}$.

This increase is path length increases the time it takes to collect charges from energy depositions. This increase in time stretches out the signal enabling greater PSD analysis. This increase in the charge collection time is not without drawbacks which must be balanced for optimal detector design. The most significant drawback comes from the charge carrier lifetime in germanium.

$$Q(t) = Q_0 e^{-\frac{x}{\mu\tau E}} = Q_0 e^{-\frac{x}{v\tau}} \tag{7.7}$$

where Q_0 is the initial charge, x is the distance traveled, μ is the charge carrier mobility, E is the electric field and τ is the charge carrier mobility coefficient. In simulations this $Q(t)$ would be inserted into the Shockely-Ramo equation for the current in Appendix A.

A separate consideration is the greater likelihood of low field regions in a PPC detectors as opposed to a semi-coaxial detector. Low fields regions allow the charge carriers to slip below the maximum drift velocity and allow for increased trapping and lattice effects. From Eq. 7.7 we can easily see the dependence of the charge carrier lifetime on the electric field. This model uses the simplified velocity from the Drude model of $v = \mu E$. In HPGe detectors the velocity term should be replaced with the much more accurate velocity from Eq. 3.1. Using Eq. 7.7 with the more accurate form of the velocity, we can plot the energy loss of an event versus its distance traveled versus the strength of the electric field in HPGe detectors using the upper limit of the charge carrier lifetime in Fig. 7.7. A good HPGe detector systems will have a FHWM of approximately 2 keV for a 1 MeV peak as compared to the energy loss in Fig. 7.7.

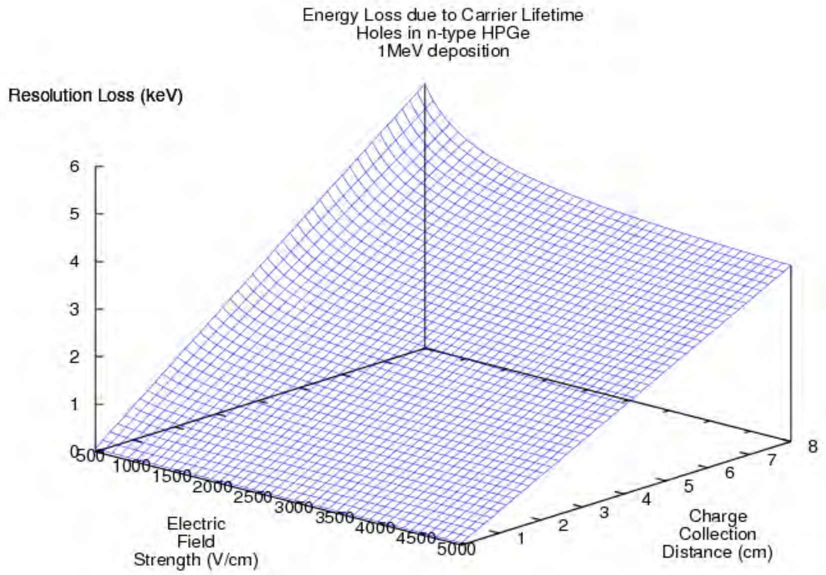

Figure 7.7: A plot of the charge carrier lifetime limit in high purity germanium at 77 k versus path length and electric field strength. This is for holes and is the loss of energy given a 1 MeV energy deposition with $\tau < 1E - 4$ seconds [6].

Based on this simple model, we can measure the charge carrier loss of a given energy if we can establish the distance the charge traveled. For semi-coaxial HPGe detectors, this correction would be insignificant except for crystals with significant lattice damage and trapping regions. For a PPC detector, however, the path lengths of the charge carriers can give rise to significant energy losses due to even a reasonable charge carrier lifetime. The two requirements for this type of measurement are that, first, we can identify events belonging to a specific full energy deposition even with charge trapping losses. Using a coincidence γ-source we can easily identify the energy of the deposition. Second, we must be able to identify the distance which the charge carrier has traveled.

A PPC detector has a very different pulse shape from a semi-coaxial detector. One major difference is that for a PPC pulse, the start time is often unknown. However, if we place a NaI detector in coincidence with the PPC detector for a ^{60}Co γ-source we can measure the start time of the pulse independently of the PPC detector. We compare the total charge carrier lifetime measured by the NaI detector to the $10-90\%$ rise time of the PPC detector. Fig. 7.8 thus verifies the simple linear relationship between the total drift time to the $10-90\%$ rise time of the PPC detector. The first implication is that if a drift time correction is necessary, then it can be done for this and similar PPC detectors. The second implication is that the $10-90\%$ rise time of a PPC pulse carries spatial and drift time information for the entire volume.

A measure of the charge carrier lifetime for the UC PPC detector was made using the ^{60}Co coincident data set. By fitting an energy peak versus the $10-90\%$ rise time, as in Fig. 7.9, we can demonstrate the effect of the charge carrier lifetime on the energy peak through its losses. Fig. 7.9 graphs the energy peaks versus rise time at depletion

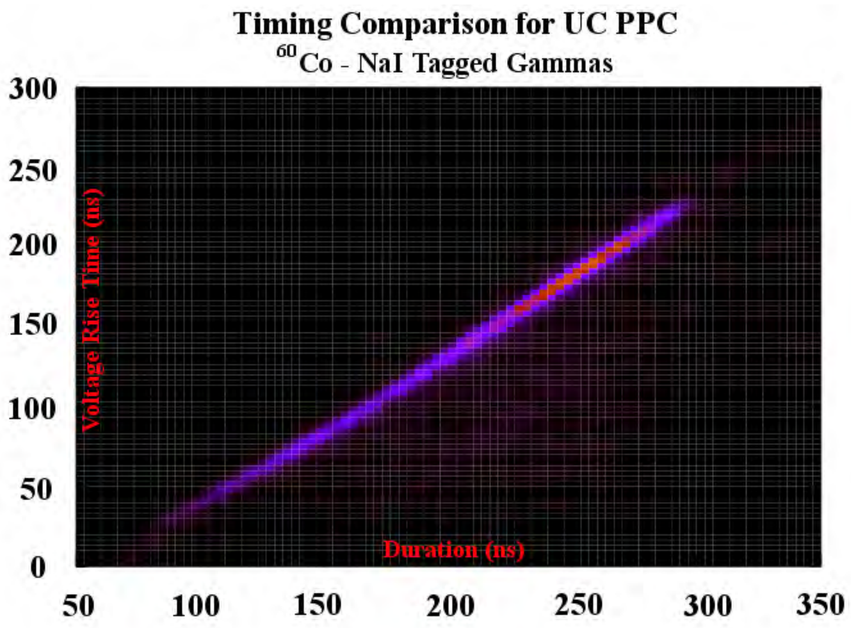

Figure 7.8: A plot of the total charge carrier drift time in the UC PPC versus the 10-90% rise time of the integrated current pulse. For the 1332.5 keV gamma of a ^{60}Co source tagged with a NaI detector. Data courtesy of Phil Barbeau and Juan Collar at the University of Chicago.

(2500 Volts) as well as at the operating voltage (3000 Volts). The charge carrier lifetime measured is $1.654E-4$ s at 2500 Volts and $0.878E-4$ s at 3000 Volts, demonstrating the need for significant electric field strengths in the PPC detector.

7.5 Optimizing a Geometry

Combining the models with a Monte Carlo we can evaluate the figure of merit for different HPGe radii and height given the same impurity density. The figure of merit to be used has previously been defined in in chapter 4 folowing from that developed by Aalseth [67]. We show the geometry space below and the results of the figure of merit calculations using a ^{228}Th source distributed uniformly around the detector.

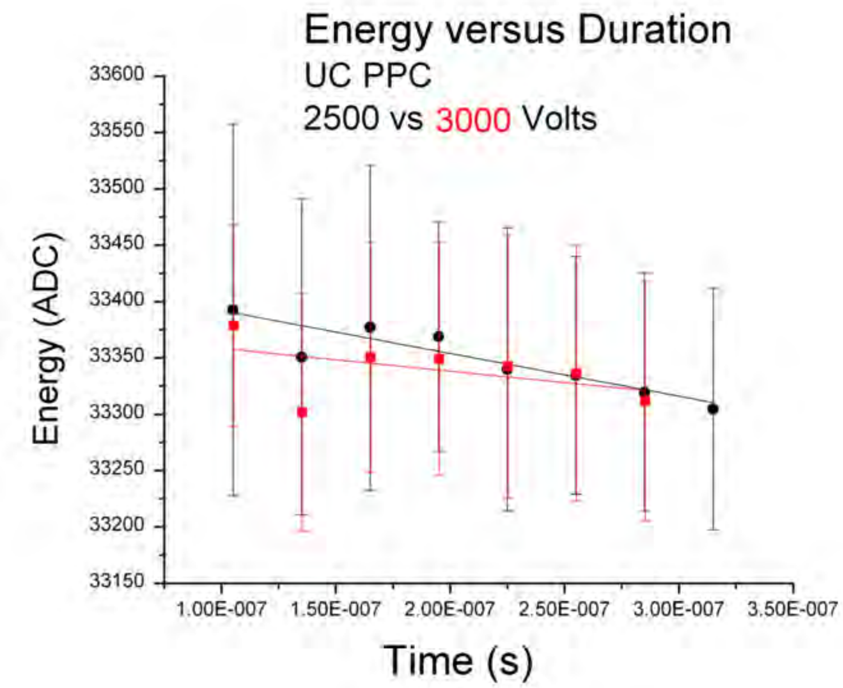

Figure 7.9: A plot of the Energy versus the duration for the UC PPC.

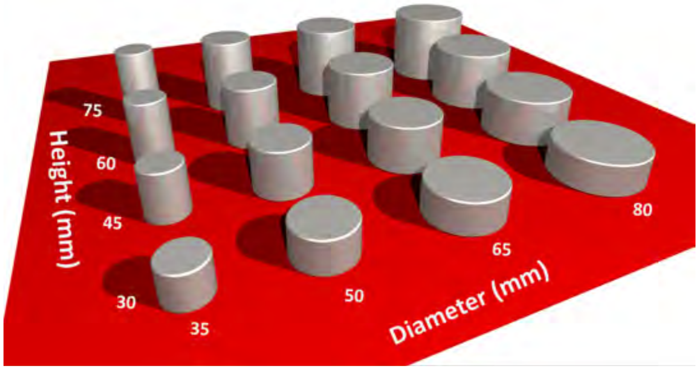

Figure 7.10: Representation of the geometric parameter space. We can see the change in diameter and height for the parameter space in question.

The parameter space consists only of the diameter and height of a P-type Point Contact detector. This parameter space is illustrated in Fig. 7.10. The point contact itself is 6mm in diameter. The impurity density equation is

$$\rho(r, z) = A + Br + Cz \tag{7.8}$$

Where A is $-100\text{E}{-5}\frac{C}{m^3}$, B is $200\text{E}{-5}\frac{C}{m^3}$ and C is $1000\text{E}{-5}\frac{C}{m^3}$. This choice allows the entire range of diameters and heights to easily be depleted under 4000 volts. Each detector had a dead layer thickness of 0.5 mm over the entire surface except the bottom passivated surface. The thorium source surrounds the detector on all sides without any absorbing material. The source include the entire thorium decay chain.

The depletion voltage for each detector was solved given the the impurity density. Each detector was simulated at 500 Volts above depletion. This gives a fairly uniform electric field throughout the detector except very close to the point contact. The potential and electric field for each detector is then stored from later use.

Once the detector geometries were defined a Monte Carlo of the radiation interactions for each detector geometry was performed. The data listed each energy deposition as part of the parent event. Each event corresponds to a single iteration through the entire decay chain. Thus no two independent decays can interfere as background or summing.

Each energy deposition has an interaction time relative to the parent event. In the charge transport simulation all energy depositions are simulated with the given location and relative timing. The signals are recorded and passed through the electronics transfer function into the appropriate file format for analysis. Thus very realistic signals are generated for analysis by the same code used to analyze experimental data.

The analysis is a pulse by pulse based parametric method developed in the IGEX experiment [73, 9, 65]. The code uses a training set of predominately single site events. Thus a single site event library can be fed directly into the analysis code, or one can use the events from a given energy whose interactions are predominately single site. In this case events from the 1592 keV peak have been shown to be > 90 percent single site through Monte Carlo simulations [65]. Using these events from the energy peak to train the analysis code, we can evaluate our ability to discriminate background, in this case the 1620 keV peak is dominated by multiple site events, also show by Monte Carlo simulations, as seen in Fig. 7.11. This method is used to evaluate the efficacy of the pulse shape discrimination method for an experiment with similar event interaction characteristics. The resulting figure of merit for the geometric parameter space (Fig. 7.10) is presented in Fig. 7.12.

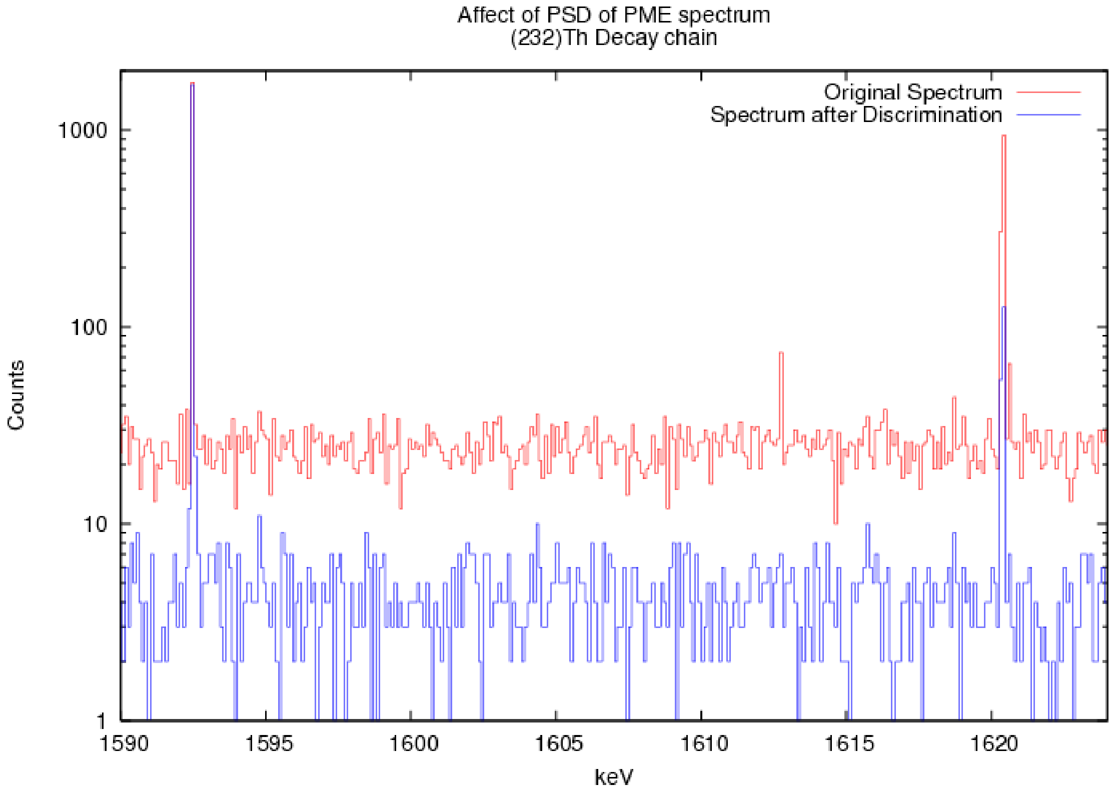

Figure 7.11: A ^{232}Th spectrum illustrating the PSD method used to remove most of the multiple site events while retaining most of the single site events. Using these peaks from this type of spectrum follows the method outlined in [9].

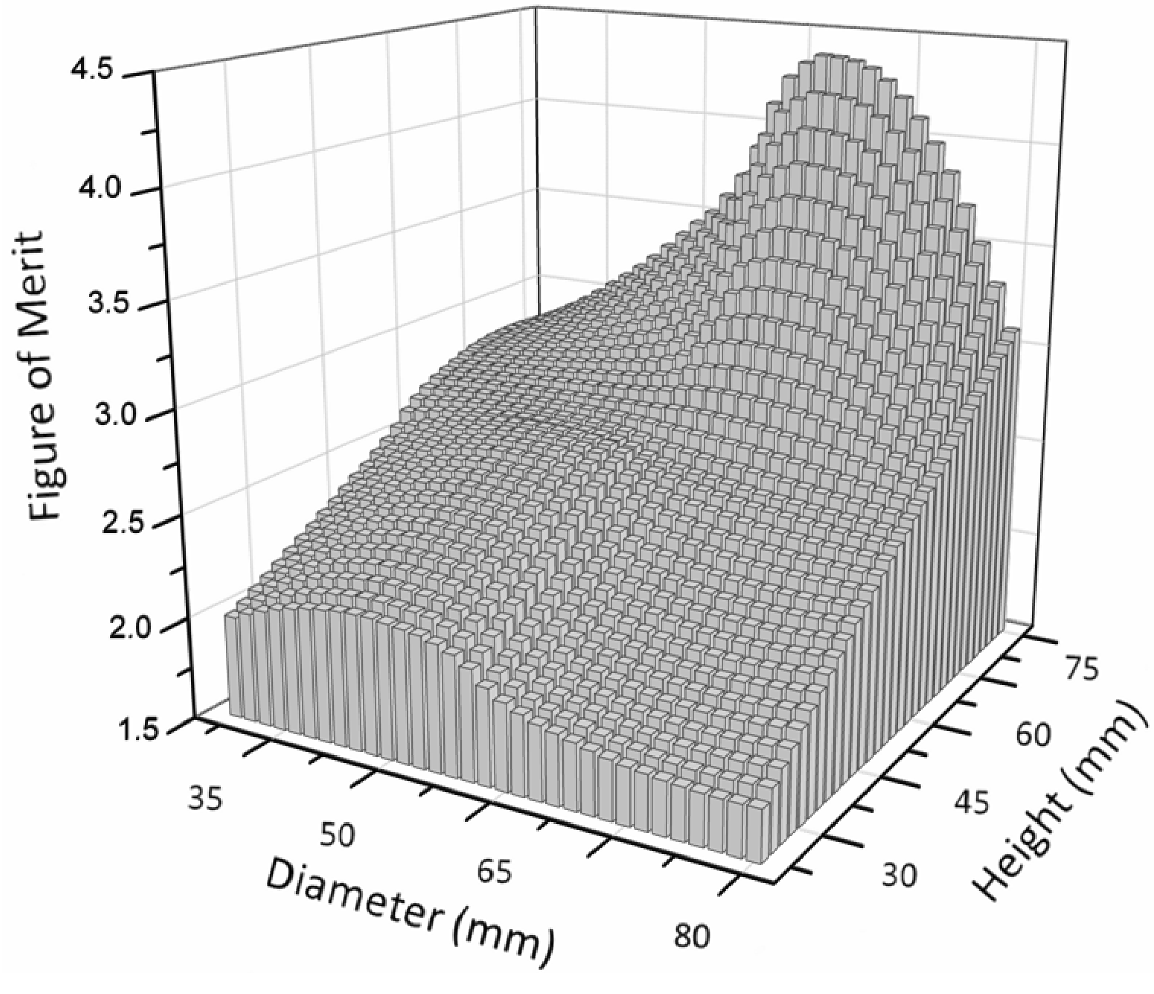

Figure 7.12: The resulting figure of merit interpolated for the geometric parameter space shown in Fig. 7.10 of different radii and heights for a simple Point Contact Detector design.

Chapter 8

Conclusion

8.1 Overview

Physicists have and will continue to explore the nature of the neutrino through a variety of experimental techniques [15, 13, 82, 32]. Neutrino-less double beta decay is a process specific to certain fundamental properties of the neutrino [12, 83, 20]. Experiments must continue to improve beyond present detector sensitivity in order to explore these properties. Advancement is required in many areas to achieve this lofty goal, detector design optimization is one such necessary advancement [84, 14, 20]. This work does not address the requirements of any specific experiment, instead it addresses the key components and develops the necessary models to optimize HPGe detector design parameters to meet experiment specific goals.

Many neutrino-less double beta decay experiments employ isotropically enriched high purity germanium detectors as both source and detector [20, 73, 23, 22]. For greatest sensitivity these experiments must build a detector that maximizes the $0\nu\beta\beta$-signal while simultaneously minimizing backgrounds and noise. If a background free condition can be obtained in the signal region within a width determined by the energy resolution, the sensitivity scales as the square root of the exposure [14]. Great efforts have gone into eliminating sources of radioactive contamination [41, 42, 43, 44, 24, 85, 86] via extreme shielding [12], evaluation and screening of all material [87], minimalistic suspension and contact design [22], the use of ultra-pure materials [27] and pulse shape analysis [65, 62, 88, 89].

A factor of 1.56 in the half life sensitivity by pulse shape analysis has been demonstrated [90], further an increase from electrical contact segmentation has also been demonstrated [62, 91]. Novel electrical contact design has also shown increase in half-life sensitivity [8]. Clearly that the sensitivity to the neutrino-less double beta decay signal in these experiments is greatly affected by many factors of the detector design and subsequent signal analysis. To truly maximize experiment efficacy, each experiment must seek an optimal detector design and operational parameters based on both initial experimental conditions and ultimate scientific goals.

In this work, models for electric field, charge transport, and signal formation are developed given an electrode geometry description, charged impurity density equation, and electrical response function as input parameters. A novel detector characterization is presented to address the difficulty of characterizing the charge impurity equation, with experimental validation. A pulse shape analysis method is also developed from previous work. The combination of these elements provides a robust evaluation of detector design and operational parameters impact on the specific goals of an experiment.

Highlights of the computer code are explained, including the geometrical representations, electrostatic solutions and signal generation dynamics. The code includes functionality for including the electrical response, nevertheless this work uses a general HPGe preamplifier response function from the appropriate literature. Results are shown to pass a series of systematic and experimental validations. The importance of the charged impurity profile to this model requires its characterization beyond current standards or even capabilities. A method is presented to iteratively solve for the charged impurity profile within the error of a χ^2 fit [51] using the measured capacitance as a function of voltage. Chapter 6 shows an example of this technique.

We provide a simple example of one possible use of this model for the optimization of input parameters for some defined experimental result. We use a simple equation for the charged impurity equation, combined with the contact geometry of a p-type point contact detector. Reasonable limits were set on the allowed depletion voltages and detector size were used. The a figure of merit for a well defined physics goal was used to find the optimal diameter and height combination given the simulation limits.

8.2 Extension of this work to future $0\nu\beta\beta$ decay experiments

Great efforts have gone into eliminating sources of radioactive contamination [41, 42, 43, 44, 24, 85, 86] via extreme shielding[12], evaluation and screening of all material [87], minimalistic suspension and contact design [22], the use of ultra-pure materials [27] and pulse shape analysis [65, 62, 88, 89]. Radiation transport and Monte Carlo simulations may be used to study the effects of material radio-purity and spatial distribution of radioactive sources within an experimental geometry. The data from these Monte Carlo simulations can then be used to couple in detector design and property limits such as impurity density

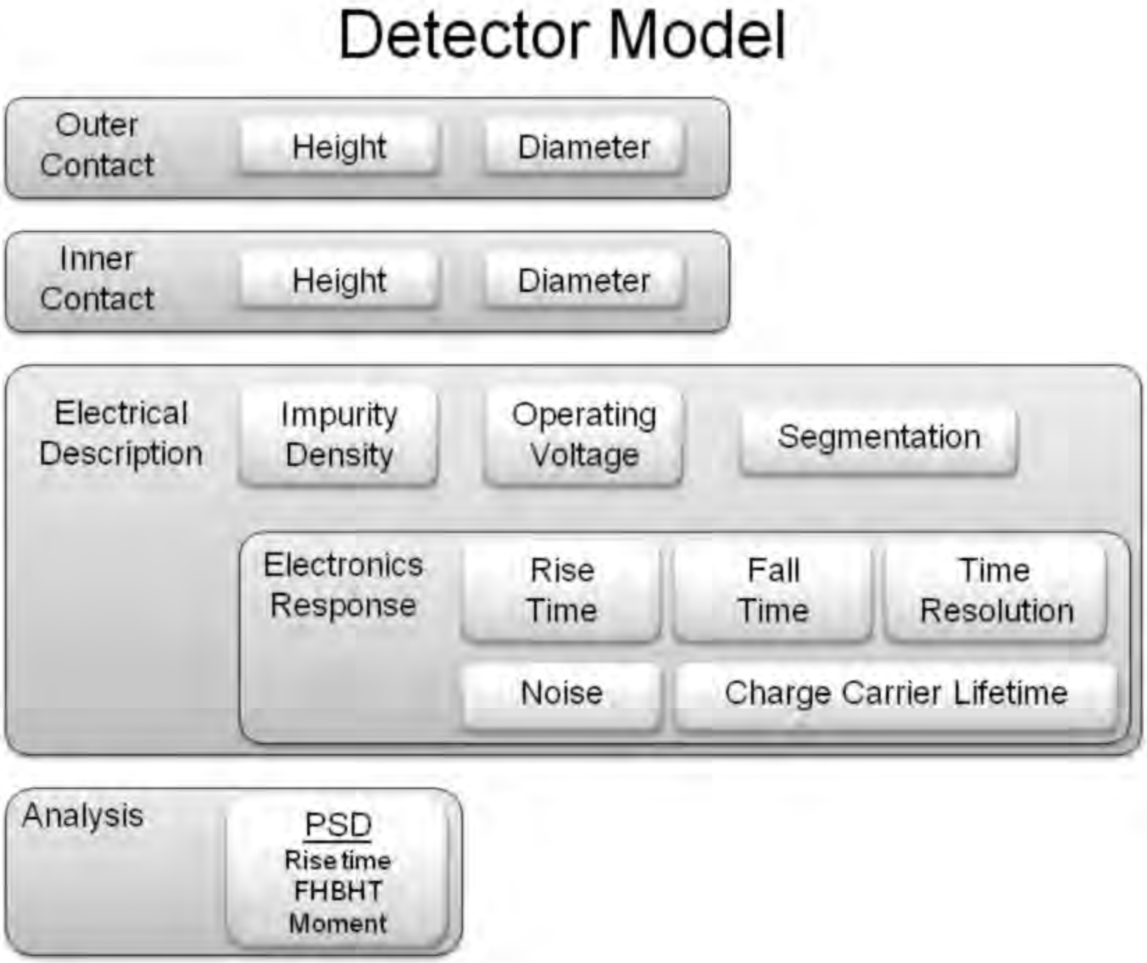

Figure 8.1: Parameterized model for for simulation of the detector response.

and charge carrier lifetime. The final step of applying the actual analysis methods directly to the simulation data will allow a realistic evaluation of the total detector design toward the science specific goals.

Our model simulates the response of high purity germanium detectors to radiation based on a large set of physical parameters. This parameter set includes the geometry, the electrode layout, the charged impurity density and even the electronics response. The model will evaluate any parameter set from simulated radiation event data completely through to the specific analysis performed on the data. Given quantifiable experiment specific goals, this entire model can be used to evaluate many possible parameter sets. This model even allows the optimization of the input parameters to achieve maximum efficiency in some appropriate experiment specific goals.

Neutrino-less double beta decay experiments will have a certain set of well defined goals for experiential success embodied in an appropriately defined figure of merit. The model can be used to optimize increasingly complex parameter spaces, within the limits set, for a maximal probability of positive outcome for this defined set of physics goals. In the case of Germanium detector experiments, at least two major experiments explore a number of alternate designs in an attempt to identify the optimal strategy for experiments scalable to one ton or more of active germanium mass. This huge undertaking will be substantially aided by the analysis tools we have developed.

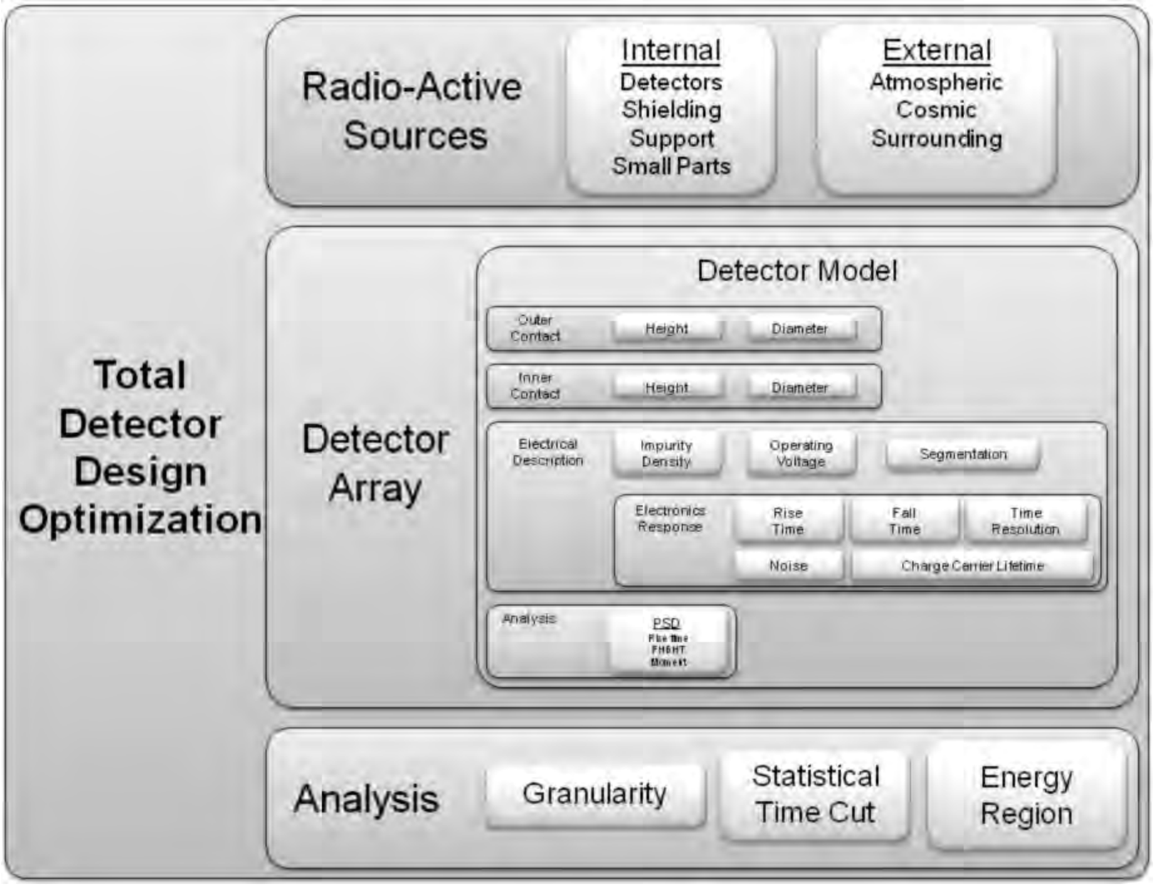

Figure 8.2: Total parameterized model for general consideration of physics experiments.

Bibliography

[1] M. Günther, J. Hellmig, G. Heusser, M. Hirsch, H. V. Klapdor-Kleingrothaus, B. Maier, H. Päs, F. Petry, Y. Ramachers, H. Strecker, M. Völlinger, A. Balysh, S. T. Belyaev, A. Demehin, A. Gurov, I. Kondratenko, D. Kotel'nikov, V. I. Lebedev, and A. Müller. Heidelberg-Moscow $\beta\beta$ experiment withˆ{76} Ge: Full setup with five detectors. *Physical Review D*, 55(1):54–67, Jan 1997.

[2] Vadim Siklitsky. Band structure and carrier concentration. http://www.ioffe.ru/SVA/NSM/Semicond/Ge/index.html.

[3] FA Trumbore. The Bell system technical journal, 1960.

[4] C. Canali, G. Majni, R. Minder, and G. Ottaviani. Electron and hole drift velocity measurements in silicon and their empirical relation to electric field and temperature. *IEEE Transactions on Electron Devices*, 22(11):1045–1047, 1975.

[5] J.H. Hubbell and S. M. Seltzer. X-ray mass attenuation coefficients. http://physics.nist.gov/PhysRefData/XrayMassCoef/tab3.html, April 1996.

[6] Glenn F. Knoll. *Radiation Detection and Measurment.* Wiley, 2000.

[7] E.E. Haller, W.L. Hansen, and F.S. Goulding. Physics of ultra-pure germanium. *Advances in Physics*, 30(1):93–138, 1981.

[8] J. I. Collar P. S. Barbeau and O. Tench. Large-mass ultra-low noise germanium detectors: Performance and applications in neutrino and astroparticle physics. *arXiv:nucl-ex/0701012v1*, 2007.

[9] H.S. Miley C.E. Aalseth. A novel method of pulse shape discrimination for germanium spectrometers. *Nuclear Physics B - Proceedings Supplements*, 2000.

[10] S. M. Bilenky, S. Pascoli, and S. T. Petcov. Majorana neutrinos, neutrino mass spectrum, *cp* violation, and neutrinoless double β decay: The three-neutrino mixing case. *Phys. Rev. D*, 64(5):053010, Aug 2001.

[11] H.S. Miley. Majorana whitepaper. Technical report, PNNL, 2005.

[12] F.T. Avignone III, S.R. Elliott, and J. Engel. Double Beta Decay, Majorana Neutrinos, and Neutrino Mass. *eprint arXiv: 0708.1033*, 2007.

[13] S.R. Elliott and J. Engel. Double-beta decay. *J. Phys*, 30:183–215, 2004.

[14] S.R. Elliott. Introduction to the Double-Beta Decay Experimental Program. *Arxiv preprint nucl-ex/0609024*, 2006.

[15] A. Barabash. Double beta decay experiments: past and present achievements. *Arxiv preprint hep-ex/0608054*, 2006.

[16] F. Boehm and P. Vogel. Physics of Massive Neutrinos. *New York: Cambridge*, 1992.

[17] B. Kayser. On the quantum mechanics of neutrino oscillation. *Physical Review D*, 24(1):110–116, 1981.

[18] Z. Xing, FR Klinkhamer, A. Kostelecky, J. Tasson, M. Pospelov, A. Ritz, S. Winitzki, R. Whisker, S.D.O. Shin'ichi Nojiri, M. Kawasaki, et al. Theoretical Overview of Neutrino Properties. *International Journal of Modern Physics A*, 23(26):4255–4272, 2008.

[19] RN Mohapatra, S. Antusch, KS Babu, G. Barenboim, MC Chen, S. Davidson, A. de Gouvea, P. de Holanda, B. Dutta, Y. Grossman, et al. Theory of Neutrinos: A White Paper. *Reports on Progress in Physics*, 70(11):1757–1867, 2007.

[20] A. Morales and J. Morales. The neutrinoless double beta decay: The case for germanium detectors. *Nuclear Physics B (Proceedings Supplements)*, 114:141–157, 2003.

[21] C. E. Aalseth, F. T. Avignone, R. L. Brodzinski, J. I. Collar, E. Garcia, D. González, F. Hasenbalg, W. K. Hensley, I. V. Kirpichnikov, A. A. Klimenko, H. S. Miley, A. Morales, J. Morales, A. Ortiz de Solórzano, S. B. Osetrov, V. S. Pogosov, J. Puimedón, J. H. Reeves, A. Salinas, M. L. Sarsa, A. A. Smolnikov, A. S. Starostin, A. G. Tamanyan, A. A. Vasenko, S. I. Vasiliev, and J. A. Villar. Neutrinoless double-beta decay of 76Ge: First results from the International Germanium Experiment (IGEX) with six isotopically enriched detectors. *Phys. Rev. C*, 59(4):2108–2113, Apr 1999.

[22] A. Bettini. GERDA. Germanium Detector Array. Search for Neutrino-less $\beta\beta$ Decay of 76Ge. *Nuclear Physics B (Proceedings Supplements)*, 168:67–69, 2007.

[23] R. Arthur F.T. Avignone III C. Baktash T. Ball A. S. Barabash F. Bertrand R. L. Brodzinski V. Brudanin W. Bugg A. E. Champagne Y-D. Chan T. V. Cianciolo J. I. Collar R. W. Creswick M. Descovich M. Di Marco P. J. Doe G. Dunham Yu. Efremenko

V. Egerov H. Ejiri S. R. Elliott A. Emanue P. Fallon H. A. Farach R. J. Gaitskell1 V. Gehman R. Grzywacz A. Hallin R. Hazma R. Henning A. Hime T. Hossbach D. Jordan K. Kazkaz J. Kephart G. S. King III O. Kochetov S. Konovalov R. T. Kouzes K. T. Lesko P. Luke M. Luzum A. O. Macchiavelli A. McDonald D. Mei H. S. Miley G. B. Mills A. Mokhtarani M. Nomachi J. L. Orrell J. M. Palms A. W. P. Poon D. C. Radford J. H. Reeves R. G. H. Robertson R. Runkle K. Rykaczewski K. Saburov Y. Sandukovsky Sonnenschein A. Tornow W. Tull C. van de Water R.G. Vanushin I. Vetter K. Warner R.A C. E. Aalseth, D. Anderson, J.M. Young A.R Wilkerson, J.F. Wouters, and V. Yumatov. The majorana experiment. *Something*, 2004.

[24] RL Brodzinski, HS Miley, JH Reeves, and FT Avignone. Low-background Germanium spectrometry the bottom line three years later. *Journal of Radioanalytical and Nuclear Chemistry*, 193(1):61–70, 1995.

[25] I. Abt, M. Altmann, A. Bakalyarov, I. Barabanov, C. Bauer, E. Bellotti, ST Belyaev, L. Bezrukov, V. Brudanin, C. Buettner, et al. A New 76Ge Double Beta Decay Experiment at LNGS. *Arxiv preprint hep-ex/0404039*, 2004.

[26] S. Schönert, I. Abt, M. Altmann, AM Bakalyarov, I. Barabanov, C. Bauer, M. Bauer, E. Bellotti, S. Belogurov, ST Belyaev, et al. The GERmanium Detector Array (Gerda) for the search of neutrinoless $\beta\beta$ decays of 76Ge at LNGS. *Nuclear Physics B (Proceedings Supplements)*, 145:242–245, 2005.

[27] E.W. Hoppe, A. Seifert, C.E. Aalseth, A.R. Day, O.T. Farmer, T.W. Hossbach, J.I. McIntyre, H.S. Miley, J.E. Smart, and G.A. Warren. A method for removing surface

contamination on ultra-pure copper spectrometer components. *Journal of Radioanalytical and Nuclear Chemistry*, 276(3):645–650, 2008.

[28] C. Amsler, M. Doser, M. Antonelli, DM Asner, KS Babu, H. Baer, HR Band, RM Barnett, E. Bergren, J. Beringer, et al. Particle Data Group. *Phys. Lett. B*, 667(1), 2008.

[29] M. Lauer. *Digital Signal Processing for Segmented HPGe Detectors Preprocessing Algorithms and Pulse Shape Analysis.* PhD thesis, s. n, 2004.

[30] L.P. Gamir. *A new method for the determination of the entry position of γ rays in HPGe detectors by current pulse analysis.* PhD thesis, Max-Planck-Institut fur Kernphysik, Heidelberg, 1997.

[31] K. Vetter. Gamma-ray tracking: Utilizing new concepts in the detection of gamma-radiation. *The European Physical Journal A-Hadrons and Nuclei*, 15(1):265–269, 2002.

[32] K. Zuber. Neutrinoless double beta decay experiments. *ACTA PHYS.POLON.B*, 37:1905, 2006.

[33] G. Heusser. Low-Radioactivity Background Techniques. *Annual Reviews in Nuclear and Particle Science*, 45(1):543–590, 1995.

[34] K.S. Krane. *Introductory Nuclear Physics.* John Wiley & Sons, 1987.

[35] K. Debertin and R.G. Helmer. *Gamma-and x-ray spectrometry with semiconductor detectors.* North-Holland, 1988.

[36] S.N. Ahmed. *Physics & Engineering of Radation Detection.* Academic Press, 2007.

[37] Karl Hess. *Advanced Theory Of Semiconductor Devices.* PublisherWiley-Interscience, 1999.

[38] C. Kittel et al. *Introduction to solid state physics*. Wiley New York, 1986.

[39] J.D. Jackson. *Classical Electrodynamics*. Wiley, 1998.

[40] U. Fano. Ionization Yield of Radiations. II. The Fluctuations of the Number of Ions. *Physical Review*, 72(1):26–29, 1947.

[41] R.L. Brodzinski, D.P. Brown, J.C. Evans, W.K. Hensley, J.H. Reeves, N.A. Wogman, F.T. Avignone, and H.S. Miley. An ultralow background germanium gamma-ray spectrometer. *Nuclear Instruments and Methods in Physics Research Section A*, 239(2):207–213, 1985.

[42] RL Brodzinski, JH Reeves, FT Avignone, and HS Miley. Achieving ultralow background in a germanium spectrometer. *Journal of Radioanalytical and Nuclear Chemistry*, 124(2):513–521, 1988.

[43] RL Brodzinski, HS Miley, JH Reeves, and FT Avignone. Further reduction of radioactive backgrounds in ultrasensitive germanium spectrometers. *Nuclear Instruments and Methods in Physics Research Section A*, 292(2):337–342, 1990.

[44] RL Brodzinski, HS Miley, JH Reeves, and FT Avignone. Ultra-low background germanium spectrometry: Techniques and results. *Nuclear Physics B Proceedings Supplements*, 28(1):415–419, 1992.

[45] S.O. Kasap. *Principles of Electrical Engineering Materials and Devices*. McGraw-Hill, 2000.

[46] S. Ramo. Currents induced by electron motion. *Proc. IRE*, 27(9):584, 1939.

[47] W. Shockley. Currents to conductors induced by a moving point charge. *Journal of Applied Physics*, 9:635, 1938.

[48] G. Cavalleri, E. Gatti, G. Fabri, and V. Svelto. Extension of ramos theorem as applied to induced charge in semiconductor detectors. *Nucl. Instr. and Meth*, 92:137–140, 1971.

[49] S. Prata. *C++ Primer Plus*. Sams Publishing, 2001.

[50] Radika. Noise in radiation detection. *Reviews of Physics*, 1982.

[51] W.H. Press, S.A. Teukolsky, W.T. Vetterling, and B.P. Flannery. *Numerical recipes in C++*. Cambridge University Press New York, 2002.

[52] L. Reggiani, C. Canali, F. Nava, and G. Ottaviani. Hole drift velocity in germanium. *Physical Review B*, 16(6):2781–2791, 1977.

[53] W. Shockley. Currents in conductors induced by moving point charge. *Journal of Applied Physics*, 1938.

[54] CE Aalseth and HS Miley. A simulation method for germanium pulse shapes. *Nuclear Science Symposium, 1999. Conference Record. 1999 IEEE*, 2, 1999.

[55] Z. He. Review of the shockley–ramo theorem and its application in semiconductor gamma-ray detectors. *Nuclear Inst. and Methods in Physics Research, A*, 463(1-2):250–267, 2001.

[56] A. Vladimirescu. *The SPICE book*. J. Wiley New York, 1994.

[57] H.S. Miley C.E. Aalseth. A simulation method for germanium pulse shapes. *IEEE Nuclear Science Symposium Conference Record*, 1999.

[58] H. Spieler. *Semiconductor Detector Systems.* Oxford University Press, 2005.

[59] G. Douysset, T. Fritioff, C. Carlberg, I. Bergström, and M. Björkhage. Determination of theˆ{76} Ge Double Beta Decay Q Value. *Physical Review Letters*, 86(19):4259–4262, 2001.

[60] R.B. Firestone, V.S. Shirley, C.M. Baglin, S.Y.F. Chu, and J. Zipkin. *Table of isotopes.* Wiley, 1996.

[61] L. Pandola, M. Bauer, K. Kröninger, X. Liu, C. Tomei, S. Belogurov, D. Franco, A. Klimenko, and M. Knapp. Monte Carlo evaluation of the muon-induced background in the GERDA double beta decay experiment. *Nuclear Inst. and Methods in Physics Research, A*, 570(1):149–158, 2007.

[62] I. Abt, M. Altmann, A. Caldwell, K. Kröninger, X. Liu, B. Majorovits, L. Pandola, and C. Tomei. Background reduction in neutrinoless double beta decay experiments using segmented detectorsA Monte Carlo study for the GERDA setup. *Nuclear Inst. and Methods in Physics Research, A*, 570(3):479–486, 2007.

[63] R.A. Fisher. On the Mathematical Foundations of Theoretical Statistics. *1992). Breakthroughs in Statistics*, 1, 1922.

[64] G. Vasilescu. *Electronic Noise And Interfering Signals: Principles And Applications.* Springer, 2005.

[65] C.E. Aalseth. *Germanium Spectrometer Pulse-shape Discrimination for 76Ge Double-beta Decay.* PhD thesis, University of South Carolina, 2000.

[66] TOC View. IEEE standard test procedures for high-purity germanium crystalsfor radiation detectors. *IEEE Std 1160-1993*, 1993.

[67] C.E. Aalseth. *Germanium spectrometer pulse-shape discrimination for germanium-76 double-beta decay.* PhD thesis, UNIVERSITY OF SOUTH CAROLINA, 2001.

[68] PN Luke, FS Goulding, NW Madden, and RH Pehl. Low capacitance large volume shaped-field germanium detector. *Nuclear Science, IEEE Transactions on*, 36(1):926–930, 1989.

[69] J. L. Orrell, C. E. Aalseth, M. W. Cooper, J. D. Kephart, and C. E. Seifert. Radial position of single-site gamma-ray interactions from a parametric pulse shape analysis of germanium detector signals. Presented at the SORMA XI Conference, Ann Arbor, MI, May 2006.

[70] MA Deleplanque, IY Lee, K. Vetter, GJ Schmid, FS Stephens, RM Clark, RM Diamond, P. Fallon, and AO Macchiavelli. Greta: Utilizing new concepts in-ray detection. *Nuclear Instruments and Methods in Physics Research A*, 430:292–310, 1999.

[71] IY Lee, RM Clark, M. Cromaz, MA Deleplanque, M. Descovich, RM Diamond, P. Fallon, AO Macchiavelli, FS Stephens, and D. Ward. GRETINA: A gamma ray energy tracking array. *Nuclear Physics, Section A*, 746:255–259, 2004.

[72] Jeremy Kephart. *Method of evaluating the effect of HPGe design on the sensitivity of physics experiments.* PhD thesis, North Carolina State University, 2009.

[73] CE Aalseth, FT Avignone III, RL Brodzinski, S. Cebrian, E. Garcia, D. Gonzalez, WK Hensley, IG Irastorza, IV Kirpichnikov, AA Klimenko, et al. IGEXˆ{76} Ge

neutrinoless double-beta decay experiment: Prospects for next generation experiments. *Physical Review D*, 65(9):92007, 2002.

[74] P.N. Luke. Low noise germanium radial drift detector. *Nuclear Instruments and Methods in Physics Research Section A*, 271(3):567–570, 1988.

[75] PN Luke. Germanium Detectors with a Built-In Transverse Drift Field. *IEEE Trans. Nucl. Sci*, 32(1), 1985.

[76] Juan Collar. Private communication. email.

[77] IY Lee. Gamma-ray tracking detectors. *Nuclear Instruments and Methods in Physics Research Section A: Accelerators, Spectrometers, Detectors and Associated Equipment*, 422(1):195–200, 1999.

[78] K. Vetter, A. Kuhn, MA Deleplanque, IY Lee, FS Stephens, GJ Schmid, D. Beckedahl, JJ Blair, RM Clark, M. Cromaz, et al. Three-dimensional position sensitivity in two-dimensionally segmented HP-Ge detectors. *Nuclear Inst. and Methods in Physics Research, A*, 452(1-2):223–238, 2000.

[79] C. Jacoboni and P. Lugli. *The Monte Carlo method for semiconductor device simulation*. Springer, 1989.

[80] D.K. Schroeder. *Semiconductor material and device characterization*. Wiley, 1990.

[81] Craig Aalseth. Private communication. email.

[82] RN Mohapatra, S. Antusch, KS Babu, G. Barenboim, M.C. Chen, S. Davidson, A. de Gouvea, P. de Holanda, B. Dutta, Y. Grossman, et al. Theory of Neutrinos: A White Paper. *Arxiv preprint hep-ph/0510213*, 2005.

[83] P. Vogel. Double Beta Decay: Theory, Experiment, and Implications. *Arxiv preprint nucl-th/0005020*, 2000.

[84] I. Abt, A. Caldwell, K. Kröninger, J. Liu, X. Liu, and B. Majorovits. Identification of photons in double beta-decay experiments using segmented germanium detectorsStudies with a GERDA phase II prototype detector. *Nuclear Inst. and Methods in Physics Research, A*, 583(2-3):332–340, 2007.

[85] H. Gomez, S. Cebrian, J. Morales, and J. A. Villar. Background reduction and sensitivity for germanium double beta decay experiments, 2007.

[86] HS Miley, RL Brodzinski, WK Hensley, JH Reeves, and FT Avignone. New techniques and results in {sup 76} Ge double-beta decay. *Conference: 2. international workshop on theoretical and phenomenological aspects of underground physics, Toledo (Spain), 9-13 Sep 1991*, 1991.

[87] FT Avignone, RL Brodzinski, JI Collar, HS Miley, E. Garcia, A. Morales, J. Morales, R. Nuñez-Lagos, JH Reeves, C. Saenz, et al. Theoretical and experimental investigation of cosmogenic radioisotope production in germanium. *Nuclear Physics B Proceedings Supplements*, 28(1):280–285, 1992.

[88] D. González, J. Morales, S. Cebrián, E. Garcıa, IG Irastorza, A. Morales, A. Ortiz de Solórzano, J. Puimedón, ML Sarsa, JA Villar, et al. Pulse-shape discrimination in the IGEX experiment. *Nuclear Inst. and Methods in Physics Research, A*, 515(3):634–643, 2003.

[89] HV Klapdor-Kleingrothaus, IV Krivosheina, and IV Titkova. Theoretical investigation of the dependence of double beta decay tracks in a Ge detector on particle and nu-

clear physics parameters and separation from gamma ray events. *Physical Review D*, 73(1):13010, 2006.

[90] CE Aalseth and HS Miley. The Majorana Project: Ge-76 $0\nu\beta\beta$-decay neutrino mass measurement. *Nuclear Physics B-Proceedings Supplements*, 110:392–394, JUL 2002.

[91] SR Elliott, VM Gehman, K. Kazkaz, D.M. Mei, and AR Young. Pulse shape analysis in segmented detectors as a technique for background reduction in Ge double-beta decay experiments. *Nuclear Inst. and Methods in Physics Research, A*, 558(2):504–510, 2006.

Appendices

Appendix A. Shockely Ramo theorem for calculation

Consider the equation for the total rate of work done by the fields given a continuous distribution of charge and current in a finite volume: (Eq. 6.103 [39])

$$\int_\tau \mathbf{E} \cdot \mathbf{J}_t d\tau \tag{A-1}$$

where $J_t = J + \frac{\partial D}{\partial t}$ such that $\nabla \cdot J_t = \nabla(J + \frac{\partial \mathbf{D}}{\partial t}) = 0$. Let us assume a quasi-static case:

$$\mathbf{E} = -\nabla\phi \tag{A-2}$$

We can write the current equation:

$$\int_\tau \mathbf{E} \cdot \mathbf{J}_t d\tau = \int_\tau -\nabla\phi \cdot \mathbf{J}_t = -\int_\tau \nabla \cdot (\phi \mathbf{J}_t) d\tau + \int_\tau \phi \nabla \cdot \mathbf{J}_t d\tau \tag{A-3}$$

The last term is equal to zero. We can apply the divergence theorem to the next to the remaining term to get:

$$\int_\tau \mathbf{E} \cdot (\mathbf{J} + \frac{\partial \mathbf{D}}{\partial t}) d\tau = -\int_S \phi \mathbf{J} \cdot d\mathbf{S} = \sum_{k=1}^{n} V_k I_k(t) \tag{A-4}$$

with V_k as the voltage applied to the k^{th} electrode and $I_k(t)$ is the current on the k^{th} electrode. We can separate out the relevant parts by the principle of linear super position such that $\mathbf{E} = \mathbf{E_1} + \mathbf{E_2} + \mathbf{E_3}$ with E_1 being the electric field due to the electrodes with no space charge, E_2 is due to static space charge ρ_2 and E_3 is due to the moving charge ρ_3 with a velocity $\mathbf{u}_3$. Note that $\rho = \rho_2 + \rho_3$, such that the boundaries are at zero potential due to the presence of charge. $\phi_1(\mathbf{r} \rightarrow \mathbf{S}) = V_k$ and $\phi_2(\mathbf{r} \rightarrow \mathbf{S}) = \phi_3(\mathbf{r} \rightarrow \mathbf{S}) = 0$ at all electrodes.

Let $V_k \rightarrow 0$ for all k, while retaining ρ_2 and ρ_3.

$$\int_\tau \mathbf{E} \cdot (\mathbf{J} + \frac{\partial \mathbf{D}}{\partial t}) d\tau = \int (\mathbf{E}_2 + \mathbf{E}_3) \cdot (\rho_3 \mathbf{u} + \frac{\partial}{\partial t}(\mathbf{D}_2 + \mathbf{D}_3)) d\tau = 0 \tag{A-5}$$

where $\mathbf{D}_2 = \epsilon \mathbf{E}_2$ and $\mathbf{D}_3 = \epsilon \mathbf{E}_3$. Then:

$$\frac{\partial \mathbf{D}_1}{\partial t} = 0 = \frac{\partial \mathbf{D}_2}{\partial t} \tag{A-6}$$

We write $\mathbf{E}_2 + \mathbf{E}_3 = \mathbf{E} - \mathbf{E}_1$ to get

$$\int (\mathbf{E} - \mathbf{E}_1 \cdot (\rho_3 \mathbf{u} + \frac{\partial \mathbf{D}_3}{\partial t})) = 0 \tag{A-7}$$

$$\Rightarrow \int \mathbf{E} \cdot (\rho_3 \mathbf{u} + \frac{\partial \mathbf{D}_3}{\partial t}) d\tau = \sum_{k=1}^{n} V_k I_k(t) = \int \mathbf{E}_1 \cdot (\rho_3 \mathbf{u} + \frac{\partial \mathbf{D}_3}{\partial t}) d\tau \tag{A-8}$$

Such that:

$$\sum_{k=1}^{n} V_k I_k(t) = \int \mathbf{E}_1 \cdot (\rho_3 \mathbf{u} + \frac{\partial \mathbf{D}_3}{\partial t}) d\tau \tag{A-9}$$

Taking the second term in the integral

$$\int \mathbf{E}_1 \cdot \frac{\partial \mathbf{D}_3}{\partial t} d\tau \tag{A-10}$$

Using

$$\frac{\partial}{\partial t} \int \mathbf{E}_1 \cdot \mathbf{D}_3 d\tau = \int \frac{\partial \mathbf{E}_1}{\partial t} \cdot \mathbf{D}_3 d\tau + \int \mathbf{E}_1 \cdot \frac{\partial \mathbf{D}_3}{\partial t} d\tau \tag{A-11}$$

We can see that

$$\int \frac{\partial \mathbf{E}_1}{\partial t} \cdot \mathbf{D}_3 d\tau = 0 \tag{A-12}$$

Since $\mathbf{E}_1$ is constant in time, we can pull the partial differential outside of the integral to get:

$$\int \mathbf{E}_1 \cdot \frac{\partial \mathbf{D}_3}{\partial t} d\tau = \frac{\partial}{\partial t} \int \mathbf{E}_1 \cdot \mathbf{D}_3 d\tau \tag{A-13}$$

We can use the definition of $\mathbf{D}_3 = \epsilon \mathbf{E}_3$ to write:

$$\int \mathbf{E}_1 \cdot \frac{\partial \mathbf{D}_3}{\partial t} d\tau = \frac{\partial}{\partial t} \epsilon \int \mathbf{E}_1 \cdot \mathbf{E}_3 d\tau \tag{A-14}$$

We can then use the relationship of the electric field to the potential $\mathbf{E} = -\nabla\phi$ to write:

$$\int \mathbf{E}_1 \cdot \frac{\partial \mathbf{D}_3}{\partial t} d\tau = \frac{\partial}{\partial t}\epsilon \int \nabla\phi_1 \cdot \nabla\phi_3 d\tau \qquad \text{(A-15)}$$

Using Green's first identify [39]

$$\int_\tau (\phi_3 \nabla^2 \phi_1 + \nabla\phi_1 \cdot \nabla\phi_3) d\tau = \oint_S \phi_3 \cdot \frac{\partial \phi_1}{\partial t} dS \qquad \text{(A-16)}$$

From this equation we know that $\nabla^2\phi_1 = \rho_1 = 0$, as well we have $\phi_3 = 0$ at the surface. So this part of the integral is zero. We are left with:

$$\sum_{k=1}^{n} V_k I_k(t) = \int (\mathbf{E}_1 \cdot \rho_3 \mathbf{u}) d\tau) \qquad \text{(A-17)}$$

With the applied voltage on electrode k being V_k we can divide through to get the current $I_k(t)$:

$$I_k(t) = \int (\mathbf{W}_{k1} \cdot \rho_3 \mathbf{u}) d\tau) \qquad \text{(A-18)}$$

where $\mathbf{W}_{k1} = \frac{\mathbf{E}_1}{V_k}$ is the weight potential. Thus we are left with the current on electrode k as a function of time due to the movement of the charge ρ_3, the applied voltage on electrode k and the electric field due to the electrodes with no space charge.